Interactive Patient-Specific Simulation of Cardiac Electrophysiology

Hugo Talbot

Université Lille1
Sciences et Technologies

Document soumis pour obtenir
le titre de Docteur de l'Université
des Sciences et Technologies de Lille

EDSPI: Section Informatique

Interactive Patient-Specific Simulation of Cardiac Electrophysiology

Hugo Talbot
Equipe INRIA SHACRA
Equipe INRIA ASCLEPIOS

Defended on the 10^{th} of July 2014

Jury:

Advisor:	Stéphane Cotin	-	INRIA Equipe Projet SHACRA
Co-advisor:	Hervé Delingette	-	INRIA Equipe Projet ASCLEPIOS
Reviewers:	Olaf Dössel	-	KIT-Institute of Biomedical Engineering
	Emmanuel Promayon	-	Université de Grenoble
Examiners:	Olivier Bernus	-	Université de Bordeaux
	Darren Hooks	-	Hopital Haut Leveque Bordeaux
Invited Examiners:	Christian Duriez	-	INRIA Equipe Projet SHACRA
	Maxime Sermesant	-	INRIA Equipe Projet ASCLEPIOS

Acknowledgments

Je tiens tout d'abord à remercier chaleureusement Stéphane Cotin et Hervé Delingette pour m'avoir encadré tout au long de ma thèse. Stéphane pour avoir su me transmettre la passion de la recherche et la motivation de tous les jours, et Hervé pour ses idées et la structure qu'il a su apporter à cette thèse. Pour leur disponibilité, leur bonne humeur et leur soutien quotidien, je tiens également à remercier Christian Duriez et Maxime Sermesant.

Comment ne pas remercier toute l'équipe SHACRA sans laquelle l'ambiance de travail n'aurait pas été la même ! Tout d'abord, mon coubureau Alexandre Bilger avec qui nous avons beaucoup partagé et qui a du enduré ma présence durant toutes ces années. Merci à Nazim. Bien sûr, Nazim Haouchine sur qui il est toujours possible de compter et qui est toujours prêt à nous offrir un point de vue différent des autres. Merci à Mario Sanz Lopez, le plus ancien ingénieur de l'équipe, pour sa gentillesse, son dynamisme et ses explications minutieuses. Et merci à Jéremie Dequidt pour son aide quotidienne, nos discussions et les bons moments partagés. Un merci spécial aux différents stagiaires avec qui j'ai eu la chance de travailler: Samra tout d'abord toujours la bonne humeur avec elle et une profonde générosité, Amir grâce à qui j'ai pu découvrir le monde de l'optimisation et enfin Aina avec qui nous avons démarrer un projet innovant sur la cryoablation. Pour leur aide très précieuse au début de ma thèse, merci à Jéremie Allard et Igor Peterlik. Merci également Hadrien Courtecuisse, Juan Pablo De La Plata, Pierre-Jean Bensoussan, Francois Jourdes, Guillaume Kazmitcheff, Ahmed Yureidini, Frederic Roy, Rémi Bessard, Damien Marchal, Bruno Carrez, Marc Legendre, Eulalie Coevet, Julien Bosman, Vincent Majorczyk, Zhifan Jiang, Fred Largillière, Valérian Verona, Valentin Vergez pour tous les moments que l'on a partagé. Last but not least, merci à Anne Rejl assistante de l'équipe SHACRA qui se démène soir et week-end pour rendre toutes nos missions et tâches administratives plus faciles !

Qui dit co-direction, dit deux équipes: merci à toute l'équipe ASCLEPIOS pour un accueil chaleureux à chacune de mes venues ! Merci à Nicholas pour m'avoir invité à participer aux événements de l'équipe. Au début de ma thèse, l'accueil de Stephanie Marchesseau, Francois Chung, Jan Margeta, Marine Breuilly et Krissy McLeod m'avait été précieux. Plus recemment arrivés dans l'équipe, je tiens aussi à remercier Chloé Audigier, Vikash Gupta, Mehdi Hadj-Hamou, Hakim Fadil, Rocio Cabrera Lozoya, Loic Le Folgoc, Thomas Benseghir et Florian Vichot. Pour tous les moments professionels ou

non passés ensemble, je souhaite remercier très spécialement Federico Spadoni avec qui nous avons développé le simulateur présenté dans cette thèse. Et merci à Isabelle Strobant pour avoir toujours faciliter mes séjours nicois.

Je remercie de plus mes collaborateurs de l'équipe du Pr. Marc O'Neill au St Thomas Hospital à Londres pour la précieuse évaluation de notre simulateur. Merci à l'IHU Bordeaux et l'IHU Strasbourg. Merci au service de radiologie du Pr. Gangi pour les expériences de cryoablation que nous avons pu faire.

Je remercie également tous les membres de mon jury de thèse. Tout d'abord, Olaf Dössel et Emmanuel Promayon qui ont la gentillesse de prendre le temps de lire et corriger minutieusement mon manuscrit. Merci à Olivier Bernus d'avoir si bien animé les discussions. Et merci à Darren Hooks pour ses idées, ses retours et sa présence dans ce jury.

Enfin je remercie tous ceux qui ont toujours été là pour moi, mes amis, ma famille, Anne-Laure.

MERCI à tous et à toutes !

Abstract

As in most of the medical departments, interns in cardiac electrophysiology follow a curriculum combining an intense theoritical learning with a long clinical practice. After years of theory (mainly book learning), junior electrophysiologists start practicing on patients under the supervision of a senior cardiologist. In the last decades, the improvement of computational technologies led to the development of numerical tools dedicated to training, planning or guiding of surgical procedures. The objective of this thesis is to construct a training framework, allowing junior electrophysiologists to practice radio-frequency (RF) ablation for the treatment of ventricular arrhythmias on virtual patients. Training on *in silico* models can not only shorten the electrophysiology curriculum, but it can also standardize it. Yet the development of such training systems raises several challenges.

The first challenge consists in simulating the cardiac electrophysiology in real-time. Through the improvement of cardiac imaging, characterization of the normal and arrhythmic electrical activity of the heart using mathematical models has been an important research topic. We focus here on a model representing the electrophysiology at the organ scale: the Mitchell-Schaeffer model. A powerful GPU implementation is proposed to reach real-time performances. Our efficient electrophysiology model is coupled with a mechanical model of the heart. A realistic left bundle branch block can be simulated, thus inducing the associated late contraction of the left ventricle.

For clinical application of electrophysiological mathematics, our virtual scenario of cardiac arrhythmias needs to be personalized. This crucial step aims at adapting all model parameters in order to fit patient data, acquired intra-operatively. After a detailed state of the art of optimization methods, the unscented Kalman filter deriving from a Bayesian approach is chosen and applied on a dataset of three patients suffering from ventricular tachycardia. Relying on our GPU electrophysiology model, the optimization process is achieved in about 20 minutes, while faithfully reproducing the pathology recorded in the operation room.

Lastly, the construction of the first training framework dedicated to cardiac ablation is presented. The scenario reproduces the catheter navigation inside the vascular system using a physics-based approach, and the beating heart is modeled from patient data. In addition to the cardiovascular navigation, a case of an ectopic focus in the right ventricle is modeled using our GPU implementation. An innovative multithreading approach couples both

simulations, thus offering performances close to real-time. The computational efficiency allows the trainee to interact with the simulation and perform all the clinical gestures, namely electrical catheter measurements, electro-anatomical mapping, electrical stimulation and eventually RF ablation. A clinical evaluation by electrophysiologists highlights the good performances and the realism of the training framework.

Keywords: Cardiac Electrophysiology Modeling, Real-Time Simulation, Arrhythmia Modeling, Cardiac Electromechanics, Nonlinear Optimisation, Model Personalization, Endovascular Navigation, Training Simulation, Radio-Frequency Ablation Planning, SOFA Framework.

Résumé

Comme dans la plupart des spécialités médicales, les internes en électrophysiologie cardiaque suivent un cursus qui repose sur un lourd apprentissage théorique d'une part, et une longue période de pratique clinique d'autre part. Après des années d'études théoriques, les internes en électrophysiologie cardiaque commence leur apprentissage clinique sur patients encadrés par des praticiens expérimentés. Durant les dernières décennies, les progrès technologiques ont mené au développement de nouveaux outils dediés à l'entrainement, au planning ou au guidage pendant l'opération. L'objectif de cette thèse est de contruire un framework permettant aux étudiants de s'entrainer virtuellement à l'ablation radio-fréquence d'arythmie ventriculaire. L'entrainement dit *in silico* permettrait non seulement de réduire le temps de formation, mais également de standardiser l'ensemble de cursus. Le développment d'un tel simulateur soulève plusieurs challenges.

Le premier challenge consiste à simuler l'électrophysiologie cardiaque en temps-réel. Par l'amélioration des techniques d'imageries, la caractérisation de l'électrophysiologie cardiaque par des modèles mathématiques est devenue un important sujet de recherche. Nous nous concentrons ici sur un modèle représentant l'électrophysiologie cardiaque à l'échelle de l'organe: the modèle de Mitchell-Schaeffer. Une implémentation GPU est proposée afin d'obtenir des performances temps-réelles. Notre modèle est ensuite couplé avec un modèle mécanique du coeur. Utilisant des données patient-spécifiques, notre simulation est capable de reproduire fidèlement un bloc de branche gauche, caractérisé par une activation et une contraction tardive du ventricule gauche.

En vue d'applications cliniques telles que le planning pré-opératoire ou le guidage intra-opératoire, notre modèle doit être personnalisable. Cette étape clé vise à adapter les paramètres de notre modèle afin de reproduire les données patients. Après un état de l'art détaillé sur les différentes méthodes d'optimisation, le filtre "Unscented Kalman" derivant d'une approche bayesienne est choisi et appliqué sur un 3 cas patients de tachycardie ventriculaire. Basé sur notre modèle d'électrophysiologie GPU, le processus d'optimisation s'exécute en moins de 20 minutes et permet de reproduire les phénomènes électriques observés en clinique,

Enfin, la construction du premier framework d'entrainement dédié à l'ablation d'arythmie ventriculaire est présentée. Le scénario reproduit tout d'abord l'étape de navigation endovasculaire en se basant sur un modèle physique. Les mouvements de contraction du coeur sont extraits de don-

nées patients. De plus, un foyer ectopique ventriculaire est simulé à l'aide de notre modèle d'électrophysiologie GPU. Une architecture multithreading permet le calcul de l'électrophysiologie et de la navigation endovasculaire en parallèle, tout en conservant des performances proches du temps-réel. La puissance de notre calcul permet aux internes d'intéragir avec la simulation et de réaliser différents gestes tels que: la mesure de potentiels extra-cellulaires, le mapping électro-anatomique, des stimulations électriques et enfin l'ablation radio-fréquence. Une évaluation clinique menée auprès d'électrophysiologistes experts et débutants démontre les bonnes performances et le réalisme de notre simulateur d'entrainement.

Mots-clés: Modélisation de l'Électrophysiologie Cardiaque, Simulation Temps-Réel, Modélisation d'Arythmie, Électromécanique Cardiaque, Optimisation Non-linéaire, Personnalisation de Modèle, Navigation Endovasculaire, Simulation d'Entrainement, Ablation Radio-Fréquence, Planning d'Ablation, Framework de Simulation SOFA.

Contents

Abbreviations

Acronym	Description
3D-Var	Three dimensional variational method
4D-Var	Four dimensional variational method
SSFP	Steady-state free precession MR imaging
AHA	American Heart Association
AV	Atrioventricular
BCS	Bestel-Clément-Sorine
BDF	Backward differentiation
BFGS	Broyden-Fletcher-Goldfarb-Shanno
Cath Lab	Catheterization laboratory
CPU	Central processing unit
CRT	Cardiac resynchronization therapy
CV	Conduction velocity
CVD	Cardiovascular disease
DI	Diastolic interval
ECG	Electrocardiograms
ECGI	Electrographic imaging
EKF	Extended Kalman filter
EU	European Union
FEM	Finite element method
GPU	Graphics processing Unit
ICD	Implantable cardioverter-defibrillator
ICI	Ionic current integration
KF	Kalman filter
LA	Left atria
LBBB	Left bundle branch block
LBM	Lattice-Boltzmann method
LV	Left ventricle
MCNAB	Modified Crank-Nicolson/Adams-Bashforth
MDT	Maximum Depolarization Time
MJED	Multiplicative jacobian energy decomposition
MRI	Magnetic resonance imaging
NICE	National Institute for Health and Care Excellence
PF	Particle filter
RA	Right atrium
RBBB	Right bundle branch block
RF	Radio-frequency
RV	Right ventricle
SA	Sinoatrial
SCD	Sudden cardiac death
UKF	Unscented Kalman filter
VF	Ventricular fibrillation
VT	Ventricular tachycardia

CHAPTER 1

Introduction

Contents

1.1 Clinical Context

Cardiovascular diseases are epidemiologically known as the main cause of death in western countries. The survey conducted by Nichols et al. (2012) and updated in Nichols et al. (2013) establishes that cardiovascular diseases (or CVD) represents nearly half (40% i.e., 1.9 million deaths) of all non-accidental deaths in 2012 in the European Union (EU), as shown in Fig. 1.1. The most common cause of CVD is the atherosclerosis, which consists in the thickening of an artery wall and can result itself in many other diseases such as cardiac arrhythmia, coronary artery disease, and heart failure. As a significant contributor to mortality, CVD represents a major economical burden for the EU economy with an overall estimated cost of €196 billion a year. Within this total cost of CVD in EU, only 54% is due to direct health care costs. This pathology also implies an important loss of quality of life, resulting in productivity losses (24%). Finally, informal care of people with CVD accounts for 22% of the total cost. The study of Nichols et al. (2012) reports a decrease in CVD mortality experienced in European countries since the mid-2000. However, the cost to the EU economies of CVD remains constant. Regarding the developing countries, predictions suggest a spreading of the epidemic, the CVD thus becoming the most common cause of death worldwide. Improvements in the medical treatment as well as in detection and prediction of CVD are necessary to reduce mortality and the associated economical burden borne by the EU.

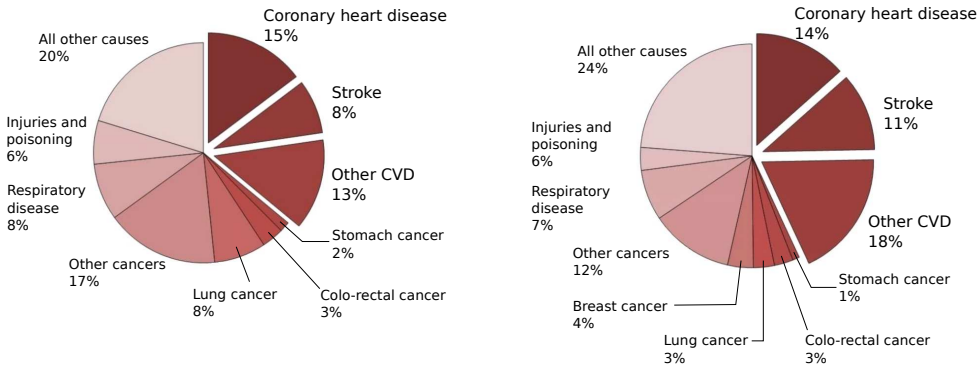

(a) For men (b) For women

Figure 1.1: Cause of death in the EU (latest year available). Courtesy of Nichols et al. (2012)

As most of the cardiac diseases, heart rhythm disorder or cardiac arrhythmia is a life-threatening pathology. Due to the intrinsic relationship between the electrical and mechanical properties of the heart, malfunctions in the electrical activity can have dramatic consequences within minutes leading to sudden cardiac death (or SCD). Cardiac arrhythmia can result in either a slower (bradycardia), faster (tachycardia) or irregular heart rhythm than the regular sinus rhythm. Ventricular tachycardia (VT) is a major concern for cardiologists since SCD is, in the majority of cases, triggered by the onset of a VT event.

Depending on the type of arrhythmia, two different interventions may be considered. First, cardioversion by shock therapy can be achieved by an external electrical defibrillation or using an implantable cardioverter-defibrillator (ICD) that continuously monitors and regulates the electrical activity. The effectiveness of the ICD therapy has been proven by Lee et al. (2003) to reduce mortality by up to 39% in patients who underwent severe ventricular fibrillation (VF) or have sustained VT. However, this therapy remains a non-curative method that does not prevent new arrhythmia events from re-occurring, and often requires pharmaceutical treatment.

The second procedure is the radio-frequency (RF) ablation that aims to occlude the re-entry circuit by performing RF thermal lesions on the isthmus. The success of this curative therapy lies in the identification of the location of the malfunctioning area and its total ablation. This minimally invasive surgery relies on endovascular navigation using specific catheters inserted from the femoral vein/artery to the targeted heart chamber. Catheter navigation under fluoroscopy, localization and ablation of the area causing the arrhythmia are challenging operations requiring highly skilled cardiologists.

This thesis was involved in the euHeart[1] project, a European research initiative targeting the personalized diagnosis and treatment of CVD. The project combined seventeen industrial, clinical and academic partners including Philips Research and Philips Healthcare. The project duration was 54 months with a budget of €19.05 million.

Within this scope, the objective of this work was to provide new computerized tools for training and therapy planning. Training simulations would allow junior cardiologists to better understand the intricacy of this procedure: endovascular navigation, signal interpretation and RF ablation in a virtual operating environment. Regarding VT, there exists no real consensus about optimum RF ablation patterns. A simulation tool modeling the patient-specific electrophysiology would tackle this issue of ablation planning and would even allow to rehearse on a virtual patient-specific electrophysiology. These challenges require many improvements regarding the state of the art. The main questions, that we aim to answer in this thesis, are:

- How to simulate the human cardiac electrophysiology in real-time ?
- Could we perform a patient-specific simulation of cardiac electrophysiology and RF ablation therapy ?
- Based on our first work on real-time electrophysiology, is it possible to develop a realistic and advanced training system by coupling electrophysiology with catheterization simulation ?

1.2 Manuscript Organisation

This thesis is organized along our published and submitted work, on which it is largely based. The resulting manuscript progresses from the implementation of an efficient electromechanical model of the heart to the development of an interactive training system using patient-specific data.

Chapter 2 introduces the background on cardiac anatomy and cardiac physiology, and then details on cardiac electrophysiology. It also presents the different types of arrhythmia and their causes, diagnoses, and treatments. This thesis focuses on ventricular arrhythmia and the associated RF ablation procedures. An introduction to cardiac electrophysiology modeling establishes the state of the art, further used in our choice of electrophysiology model.

In **Chapter 3**, based on Talbot et al. (2013a), we propose an efficient implementation of cardiac electrophysiology using latest GPU computing techniques. Second, a mechanical simulation is then coupled to the electrophysio-

[1]Read more about euHeart: www.euheart.eu

logical signals to produce realistic motion of the heart. We demonstrate that pathological mechanical and electrophysiological behaviour can be simulated.

In **Chapter 4**, based on Talbot et al. (2014a), a state of the art on model personalization is proposed. Our personalization method based on the unscented Kalman filtering is explained and the performance of the algorithm is evaluated.

In **Chapter 5**, based on Talbot et al. (2011, 2013b, 2014c), we present a training system dedicated to cardiac electrophysiology, including pacing and ablation procedures. Based on a multithreading approach, our framework involves a faithful catheter navigation and an efficient GPU-based electrophysiological model, both running asynchronously. With this method, we reached high computational performances that allowed to account for user interactions in real-time. With a scenario of cardiac arrhythmia, we demonstrate the ability of our simulator to reproduce a complete ablation procedure.

Chapter 6 concludes this thesis and, based on Talbot et al. (2014b), opens new fields of research such as cryoablation simulation for cardiac arrhythmia.

CHAPTER 2

State of the Art on Cardiac Electrophysiology

Contents

2.1 Cardiac Anatomy

The heart is a hollow muscular organ that pumps blood through the entire body by contracting repeatedly. It can be described as a double pump: one for the pulmonary circulation and the other for the systemic circuit, see Fig. 2.1(b). Each separated pump is made up of one superior atrium and one inferior ventricle, as illustrated in Fig. 2.1(a). The right chambers of the heart drive the de-oxygenated blood from the veins to the lungs for oxygenation. The superior and inferior vena cava carry the de-oxygenated blood to the right atrium (RA), the blood is then pumped to the right ventricle (RV) through the tricuspid valve before being pumped out through the pulmonary valve into the lungs. The oxygenated blood returns from the lungs into the left atrium (LA), where it is pumped through the mitral valve into the left ventricle (LV).

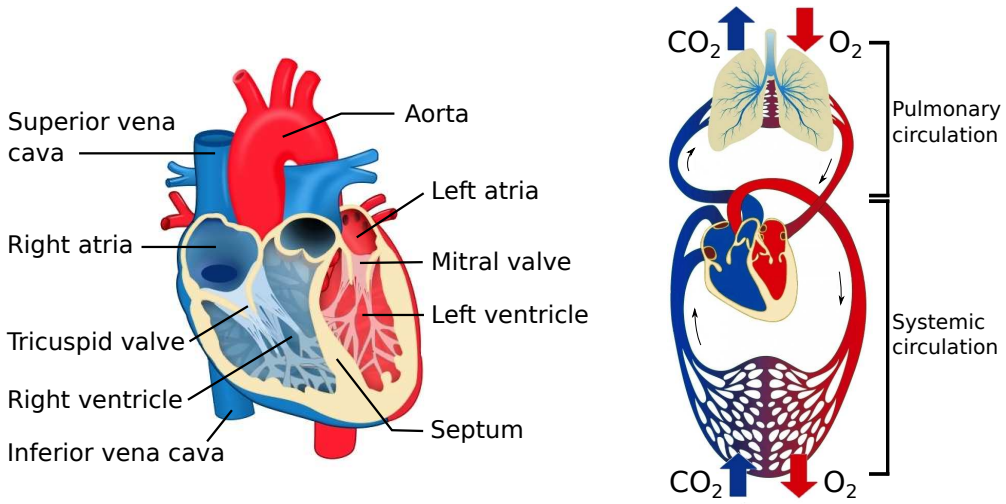

(a) Four cardiac chambers. From wikipedia.org

(b) Circulatory system

Figure 2.1: Anatomy of the human heart

The powerful contraction of the LV then ejects the blood through the aorta to provide oxygen to the body.

The heart is located anterior to the vertebral column and posterior to the sternum. The whole organ is covered by a tough double-layered membrane: the pericardium. The pericardial cavity is filled with a serous fluid preventing friction during contractions. This double-walled sac protects the heart, anchors its surrounding structures and avoids any overfilling of the heart with blood. The outer wall of the human heart is composed of three layers. The epicardium is the outermost layer of the heart wall and merges with the inner layer of the pericardium. Below the thin epicardium is the second, thicker layer of the heart wall: the myocardium. This middle layer is the active part of the heart responsible for pumping blood. Containing the cardiac muscle tissue, myocardium makes up the majority of the mass of the heart wall. Finally, endocardium is the simple squamous endothelium layer that covers the inside of the heart. Its smooth surface prevents blood from sticking to the inside of the heart, i.e. avoiding clot formation.

The cells making up the myocardium are called cardiac myocytes, structured in fibers. This specific cardiac cytology ensures the electrical continuity between cells. Fiber orientation is varying along the myocardium. This orientation is defined using an elevation angle corresponding to the obliquity of the fibre with respect to the plane of the section. The elevation angle amounts to $+70°$ on the endocardium, to $0°$ at the middle of the endocardium and to $-70°$ in the epicardium. Inducing a twisting during contraction, the fiber

structure of the heart (detailed in Fig. 2.2) optimizes the pump function while minimizing the muscular work.

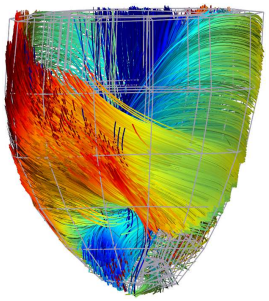

Figure 2.2: Ventricular fibers from *in vivo* Diffusion Tensor Imaging (DTI). With courtesy of team.inria.fr/asclepios

2.2 Cardiac Electrophysiology

2.2.1 Excitability

In the rest configuration, the myocardial fibers are polarized, i.e. there is an electrical potential difference between the inside and the outside of the cells. This potential difference is called the transmembrane potential (or transmembrane voltage). Its value evolves according to the gradient of ionic concentration between the intracellular and extracellular medium. In a rest state, the rest transmembrane potential of ventricular cells amounts to about -90 mV. Every unique electrical stimulus generates an action potential response that can be divided into three main phases, as shown in Fig. 2.3(c):

1. a fast depolarization,
2. a plateau phase,
3. and a repolarization back to the rest potential.

This electrical phenomenon corresponds to sharp variations of the ionic permeability (or conductance) of the cell membrane. Orientation of the ionic flow through cell membrane is detailed in Fig. 2.3(a) and the evolution of ionic concentrations is plotted in Fig. 2.3(b). During the different phases, many different ions flow through this permeable membrane, thus modifying the ionic composition inside and outside the cells. A simplified description amounts to consider the evolution of the three main ions: sodium, calcium and potassium. In phase 1, the fast sodium channel (Na^+) is activated: a dramatic increase of the transmembrane potential occurs due to the sodium concentration. The phase 2 (plateau phase) characterizes a slow de-activation

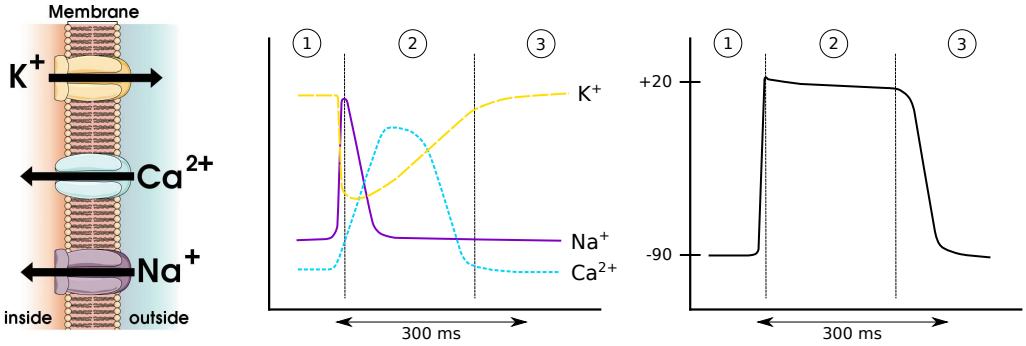

(a) Simplified ionic flow through cell membrane

(b) Relative ionic conductances

(c) Action potential response (mV)

Figure 2.3: Electrical activity of cardiac myocytes

of the potassium channel (K^+) and fast sodium channel, whereas the calcium channel (Ca^{2+}) opens. The calcium inflow triggers the shortening of cardiac fibers. Finally, calcium flow decreases while the potassium channel is gradually re-activated. This last step allows the re-establishment of the ionic rest state. The resulting transmembrane potential is given in Fig. 2.3(c).

To initiate this action potential response, the stimulus must exceed a threshold in terms of intensity and duration. In case of a short or low stimulus, the depolarization cannot be triggered.

Until the end of the plateau phase, cardiac cells are refractory to any stimulation. The generation of a new action potential is consequently impossible during this period, thus preventing from additive contractions or tetanic contractions. The absolute refractory period also determines the maximum contraction frequency, i.e. the heart rate. Following this absolute refractory state, cardiac cells recover a relative excitability. A premature action potential can be initiated provided that intensity of the stimulus is higher than the initial stimulus.

2.2.2 Automaticity and Conductivity

In his experimental work, Albrecht von Haller (1708-1777) demonstrated the automaticity of the heart in 1757. This Swiss biologist highlighted that a heart removed and placed in an adequate medium keeps beating regularly without any extrinsic stimulation. The reason of this mechanical automaticity lies in the fact that action potentials are spontaneously generated within the heart muscle. This natural pacemaker, called the sinoatrial (SA) node, is located in the upper wall of the RA close to the junction with the superior vena cava, as illustrated in Fig. 2.4(a). The regular electrical stimulation induced by these

specific cells (about 60-100 beats per minute) is called the sinus rhythm.

As other cardiac myocytes, the resting potential of the SA tissue results from a continuous outflow of potassium ions through the membrane. However, the potassium permeability of SA cells early decreases, thus partly causing a slow depolarization. As described in Fig. 2.4(b), the slow depolarization continues until a threshold potential is reached, triggering the propagation of a depolarization wave. The action potential stroke is smoother than for regular cardiac myocites due to a slow influx of calcium ions. The SA cell finally repolarizes with the re-activation of the potassium channel.

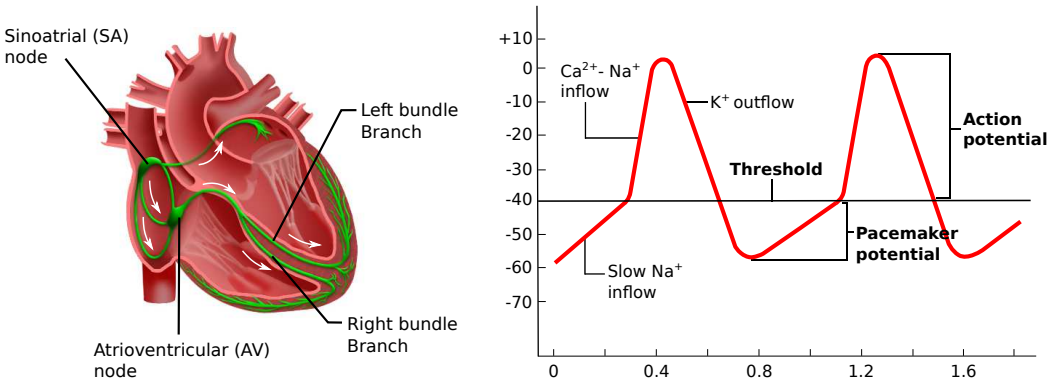

(a) Conduction pathways of the heart (green). From hopkinsmedicine.org

(b) Electrical potential (mV) of pacemaker cells against time (sec)

Figure 2.4: Pacemaker and condution pathways of the heart

Generated in the SA area, the depolarization wave propagates through atrial fibers. These branched cardiac cells enable an easy transmission of action potentials due to low resistance junctions between the cells. Conduction velocity (CV) in the atria ranges between 0.8 and 1 m/s. Once the atria are stimulated, the depolarization reaches the atrioventricular (AV) node, located in the postero-inferior region of the interatrial septum. This key tissue connects both atria and ventricles. It is characterized by a slow activation, i.e. a low CV about 3 to 5 cm/s. The AV node therefore delays the conduction, so that atria contract first and actively fill the ventricles. Leaving the two upper chambers of the heart, the depolarization wave subsequently follows a preferred conduction pathway, as detailed in Fig. 2.4(a). First, the His bundle, located inside the fibrous skeleton of the heart, extends the SA node. The His bundle is then divided into two branches (left and right) for each ventricle, that itself gives rise to two other branches (anterior and posterior). CV in these septal fibers amounts to 1 m/s. The endocardial ramifications of these branches constitutes the Purkinje network, where CV reaches 4 m/s. The Purkinje network activates all cardiac myocites inside the ventricles.

In the heart, myocardial fibers are responsible for the anisotropic propagation of action potentials, thus creating a syncytium-like structure for the conduction.

2.2.3 Cardiac Cycle

The cardiac cycle refers to the electrical and induced mechanical events occurring during a unique contraction-relaxation cycle. This cardiac cycles involves three significant pressure values: the ventricular, atrial and aortic pressures. Their evolution is plotted in Fig. 2.5 and is detailed below.

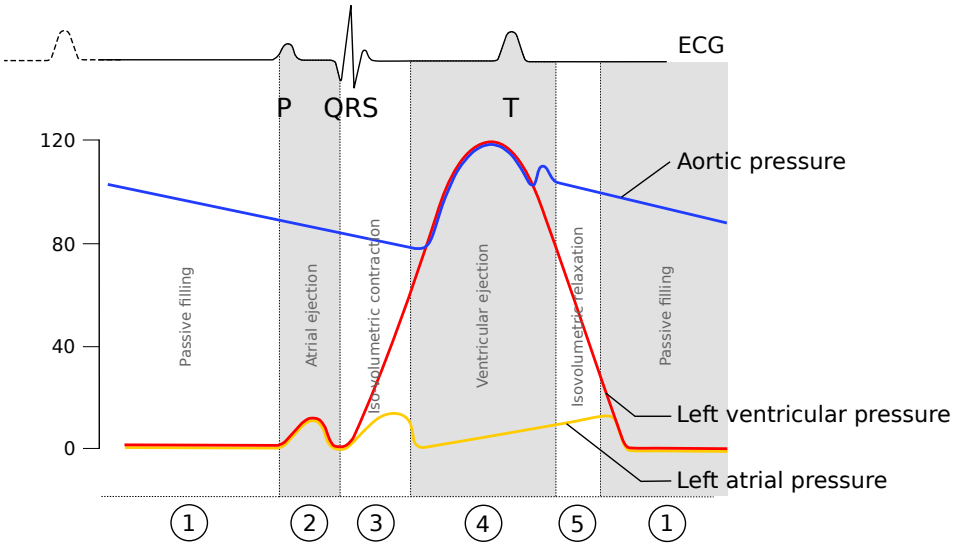

Figure 2.5: ECG and pressure (in mmHg) evolutions during a cardiac cycle

First, the ventricular pressure is very low during the ventricular diastole (phases 1-2 in Fig. 2.5). Below 1 mmHg during the atrial filling (1), the pressure increases up to 5 mmHg due to the atrial contraction (2). Blood flows from the atria to the ventricles. The AV valve then closes and the ventricular muscle starts contracting: the ventricular systole (3) begins. This isovolumetric contraction translates into a large increase of the ventricular pressure. The ventricular chambers open under the pressure and the blood flows out. During this ejection phase, the pressure in the left ventricle reaches its maximum around 120 mmHg before decreasing (4). Pulmonary and aortic valves close and the fibers relax after the repolarization, thus inducing a pressure fall back to the initial value (5).

The atrial pressure undergoes three main increases. The first leap occurs during the phase 2 due to the contraction-relaxation of the atrium. During the rapid ejection phase (4), ventricular contraction pushes the AV valve into the atrium and increases atrial pressure. At the beginning of diastole (5),

blood gradually fills the atrium while the AV valve is closed, causing atrial pressure to rise.

During the ventricular diastole, the aortic pressure slowly decreases. As soon as the ventricular pressure exceeds the aortic pressure, the valves opens inducing a brutal increase of pressure. Following the decrease of the ventricular pressure, the aortic valve closes and generates a slight overpressure in the aorta. The behavior of the aortic valve only depends on the pressure gradient between the inside of the LV and the aortic pressure.

2.2.4 Electrocardiogram

To guide their diagnosis, cardiologists rely on electrocardiograms (ECG) that measure the intra-cardiac electrical activity. Many leads can be chosen to observe electrical response along different axes. The electrodes are combined into pairs whose output signal is known as a lead. Leads (detailed in Fig. 2.6) can be sorted into two categories:

- the peripheral leads (noted D) placed on the four limbs in order to explore the frontal plane of the heart,
- the precordial leads (noted V) placed on the thorax in order to explore the transverse plane of the heart.

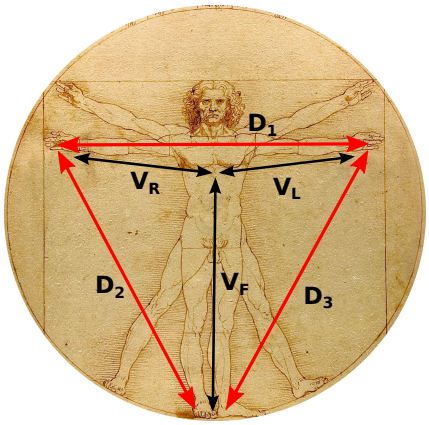

Figure 2.6: ECG leads

As shown in Fig. 2.5, the ECG is decomposed with PQRST waves. The first P wave is associated to the atrial depolarization, whereas the QRS wave reflects the rapid depolarization of ventricles and the T wave their repolarization. The QT interval represents the Action Potential Duration (APD). The time interval between two cardiac cycles (TP interval) is known as the diastolic interval (DI).

2.3 Cardiac Electrical Disorders: Arrhythmia

Cardiac arrhythmias are characterized by an abnormal propagation of the wave of cardiac excitation, or by an abnormal initiation of the wave, or even by a combination of both. Cardiac arrhythmia can manifest themselves in many different ways, and their mechanisms cannot always be precisely established.

2.3.1 Classification

Arrhythmias may be classified in several ways: by site of origin, by rate and by mechanism. First, cardiac arrhythmia can occur in the upper part of the heart (atria), in the lower part (ventricles) or at the AV junction. Second, an arrhythmic activity is associated with any perturbation of the regular heart rhythm: arrhythmia can thus produce irregular, faster or slower heart beats. Over 100 beats per minute in rest, the cardiac rhythm is considered as too fast: this is called tachycardia. Conversely, below 60 beats per minute, the heart is in a state named bradycardia.

However, supplying the above information regarding the region and the rate of the arrhythmia cannot be sufficient to define the pathophysiology. In this work, we focus on ventricular arrhythmia. The different mechanisms responsible for cardiac arrhythmia will therefore be detailed considering the ventricles as region of interest. The associated ECG signals are plotted in the Table 2.1.

- The **idioventricular rhythm**: results in a regular bradycardia with 20 up to 40 beats per minutes. With this pathology, the electrical stimulus is not generated by the SA node. In the absence of triggering signals, the ventricular myocardium itself becomes the pacemaker. Due to the inactivity of the atria, no P wave can be detected on the ECG.

- The **ventricular extrasystole**: is a premature depolarization and contraction of the ventricle, followed by a resting period. A pacemaker activity in an abnormal location creates an unexpected beat. The heart rhythm is usually normal (between 60 and 100 beats per minute) and a pacemaker activity in an abnormal location of the ventricle creates an unexpected beat. On the ECG, an irregular QRS complex can be easily identified. The abnormal pacing region is the ectopic focus, and the extrasystolic beat is named the ectopic beat. The severity of a ventricular extrasystole relies on its frequency, but also on its morphology: it can be monomorphic (sustained morphology) or polymorphic (beat-to-beat variations in morphology).

- The **ventricular tachycardia** (VT): corresponds to a heart rate from 120 up to 280 beats per minute. An augmented automaticity of the ventricle leads to this abnormally fast rhythm, that can be either regular or irregular. Several extrasystoles can be responsible for this ventricular automaticity, combined with a re-entry circuit. As the ventricular extrasystole, VT can be either monomorphic or polymorphic.

- A **Torsade de Pointe**: is a specific VT characterized by irregular and rapid (about 250 beats per minute) ventricular depolarizations. A ventricular extrasystole occurring during the T wave triggers this intense tachycardia. The amplitude of the QRS complex changes as well as the electrical axes. Usually a Torsade de Pointe is a very short event and stops spontaneously. However, it can degenerate into VF.

- The **ventricular flutter**: is a form of rapid but regular VT (over 200 beats per minute). The QRS cannot be clearly distinguished since only a large sinusoidal signal appears on the ECG. As for VT, an ectopic focus (usually located in the left branch of the His bundle or in the Purkinje network) combined with a re-entry circuit allows this augmented automaticity.

- The **ventricular fibrillation (VF)**: results in an irregular cardiac rhythm with more than 300 beats per minute. A VF is the evolution of previous extrasystoles or VT (including Torsade de Pointe and flutter). The ventricular depolarization is so fast and chaotic that the resulting contraction is uncoordinated, which prevents an effective blood circulation (cardiogenic shock). As a consequence, SCD may result in a matter of minutes. VF is therefore a medical emergency.

Another category of arrhythmia is often defined separately: the branch blocks. A branch block is an abnormal conduction of the electrical flow occurring in the main conduction pathway (illustrated in Fig. 2.4(a)). Two branch blocks can be identified:

- The **AV branch block**: is an abnormal conduction of the electrical impulse at the AV node. However, different degrees of severity exists in the AV branch block. In the first degree (represented in Table 2.1), a permanent slow down in the AV conduction associated with a normal cardiac rhythm leads to a regular QRS signal, but the PR interval is slightly larger than in the sinus rhythm. The second degree is a partial branch block that can be regular or irregular. The third degree of AV branch block is a complete heart block, so that the stimulation generated

	Sinus rhythm	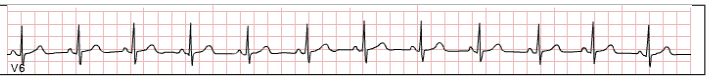
Rhythm disorders	Idioventricular rhythm	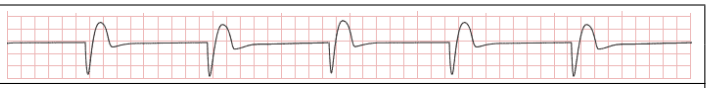
	Ventricular extrasystole	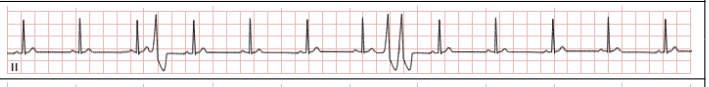
	Ventricular tachycardia	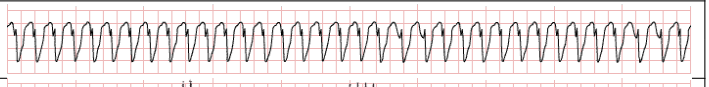
	Torsade de pointe	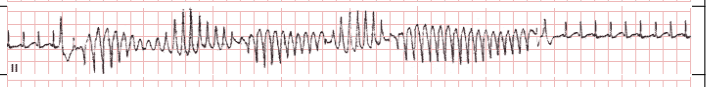
	Flutter	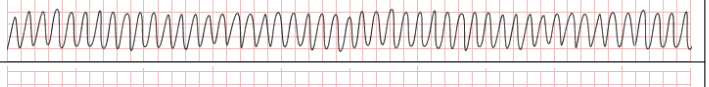
	Ventricular fibrillation	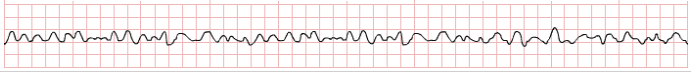
Conduction disorders	Atrioventricular branch block	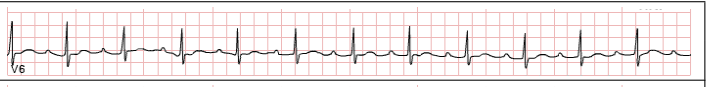
	Left bundle branch block	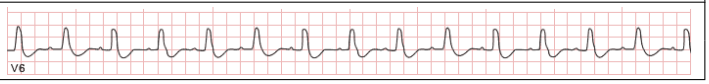

Table 2.1: ECG signals corresponding to the different mechanisms of arrhythmia. With courtesy of www.inhalotherapie.com

from the SA node does not propagate from the atrium to the ventricle, which leads to an idioventricular rhythm.

- The **bundle branch block**: is characterized by an abnormal conduction in the His bundle due to lesion or interruption of the bundle. This block can be located in the right or in the left branch, respectively named Right Bundle Branch Block (RBBB) and Left Bundle Branch Block (LBBB), and can be partial or complete. An asynchronous ventricular contraction arises as a consequence of the late depolarization of the concerned ventricle. With about 60 to 100 beats per minute, the QRS therefore looks enlarged and deformed. The bundle branch blocks can result from an underlying cardiomyopathy. The normal coordinated motion of the heart is known to optimize the pump function while minimizing the muscular work. In the case of a LBBB, the late activation of the LV implies an asynchronism, thus requiring the LV to compensate the loss of effectiveness. A cardiomegaly is therefore often associated with a LBBB. A RBBB is generally considered as benign, since the pumping function is mainly ensured by the healthy LV.

The major arrhythmias have been presented, but combinations of atrioventricular pathologies are possible. In this thesis, we will focus on two ar-

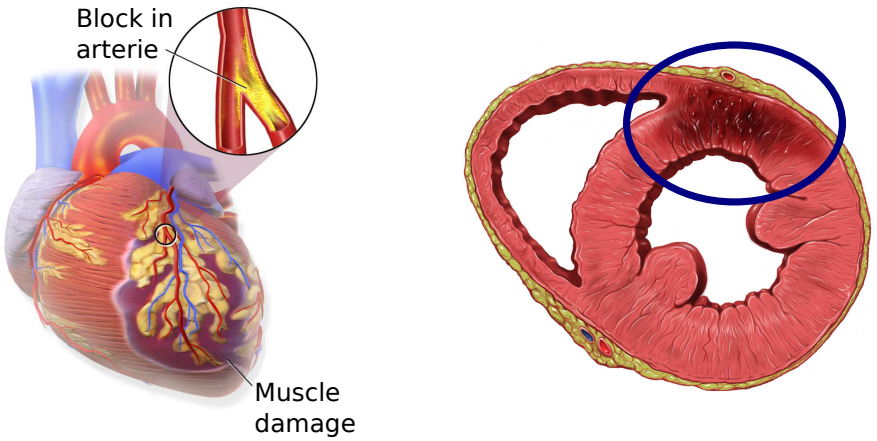

(a) Heart attack (b) Heart with infarction

Figure 2.7: Causes of an ischemic cardiac disease. Images modified from *Wikipedia*

rhythmias: the LBBB and the VT. More attention is now be given to these pathologies, their mechanism and etiology.

Both LBBB and VT have just been described as life-threatening events. Moreover, their etiology is very similar: the most common setting for both LBBB and VT is an ischemic cardiac disease. As shown in Fig. 2.7, atherosclerotic plaques may build up in the inner lining of a coronary artery (artery ensuring blood supply of the heart). When a plaque suddenly ruptures under blood pressure, it causes catastrophic thrombus formation, totally occluding the artery: this is myocardial infarction. If no medical treatment is provided, the ischemia (restriction in blood supply) ensued with oxygen shortage leads to irreversible damage or death of the myocardial cells. This ischemic cardiac disease, i.e. ischemia in the myocardium, can result in cardiac arrest or cardiac arrhythmias, such as LBBB or VT. The etiology of LBBB and VT also includes, among others, neurological causes, metabolic troubles (hyperkalemia), or medicinal treatments.

As explained previously, the mechanism of the LBBB consists in a block of conduction in the left part of the heart, thus creating an asynchronous contraction. However, the mechanism triggering VT is more complex and can be divided into two classes:

- **the re-entrant VT**: is the most complex form of VT. The myocardial tissue undergoes repetitive excitations by a propagating wave circulating around an obstacle (anatomical re-entry) or circulating freely in the tissue as a scroll wave (functional re-entry). Both anatomical and functional re-entries can degenerate into multiple re-entries, thus leading to

fibrillation. This tachycardia may remain confined in one single chamber or propagate to other chambers.

- *anatomical re-entry*: its complex propagation comes from the interaction of the depolarization wavefront with its own refractory tail. The restitution curve represented in Fig. 2.8 shows that the Action Potential Duration (APD) and the CV vary depending on the cardiac pacing rhythm. One heart has therefore different spatial patterns (short or long) for APD. In a healthy case, all cardiac regions experience the same (short or long) action potential. Strong spatial variations of this APD may appear around scar tissues. These local heterogeneities may give rise to cardiac re-entries.

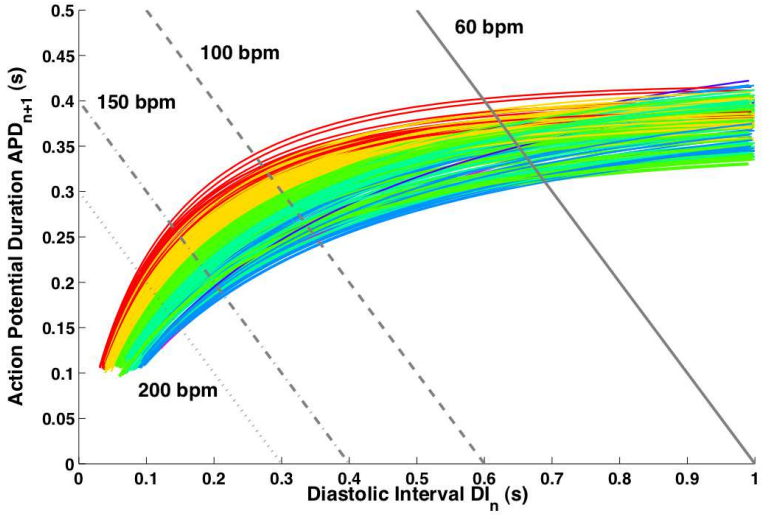

Figure 2.8: Action potential against the diastolic interval at different pacing frequencies. From Relan et al. (2011a)

- *functional re-entry*: consists in spiral or scroll waves induced by a single stimulus during the relative refractory period. An electrical impulse occurring at the end of the repolarization phase can produce a new and early depolarization. This re-entry rotates around functional obstacles which correspond to the cores of the spiral or scroll waves. Functional arrhythmias are especially dangerous and complex to treat when they are polymorphic.

- **the non re-entrant VT**: is usually generated by one or more pacemaker activities (extrasystole) located in abnormal anatomical sites (ectopic focus).

In this manuscript, the Chapter 3 focuses on LBBB. Then, the Chapter 4 addresses the issue of personalization of cardiac electrophysiology in the scope of re-entrant VT, while the Chapter 5 considers non-re-entrant VT.

2.3.2 Mapping Cardiac Electrophysiology

For clinical surgery or research, recovering the electrical activity of the heart is compulsory. These techniques for electrophysiology mapping are now presented.

ECG Detailed in Subsection 2.2.4, the ECG is a non-invasive technique widely used in clinical routine. Skin electrodes are directly placed on the torso at specific locations in order to capture the electrical signals produced by the heart. Cardiologists are trained to interpret the ECG and to detect cardiac abnormalities based on deflections from a healthy PQRST signal. The recent work of Zettinig et al. (2013) considers data from a 12-lead ECG for calibration of a cardiac electrophysiology model. This will be further discussed in Chapter 5.

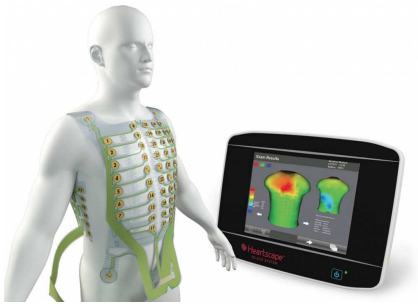

Figure 2.9: Vest used for the ECGI method. From `arwatch.co.uk`

Body surface mapping The interpretation of ECG signals allows to establish a global diagnosis. However, this technology is not suitable to obtain local information, since it measures the electrical potential reflected on the body surface. To solve the limited spatial resolution, recent work Guillem et al. (2013); Rudy (2010); Wang et al. (2007b) investigate a non-invasive technology: the electrographic imaging (ECGI). A vest with multiple electrodes measures the activity on the torso, as shown in Fig. 2.9. Based on *a priori* knowledge of solution characteristics, it evaluates the epicardial potentials and isochrones from the measured potentials. Farina et Dössel (2009) and Rudy (2010) focus on the solution of the inverse problem of the activity reflected on the body surface towards the underlying cardiac electrophysiology.

Figure 2.10: Catheterization laboratory or Cath-Lab. From www.medwow.com

The presented results are promising and could help to better understand the arrhythmia mechanisms.

Electroanatomic mapping Minimally invasive procedures make possible the *in vivo* measurements of the cardiac electrophysiology. These procedures allow an intensive electrophysiology study but require a specific equipment in the operation room, also called Catheterization Laboratory or Cath-Lab (see photo in Fig. 2.10). The cardiologist starts by inserting the mapping catheters in the femoral vein (in the groin). The venous system is preferred due to its laminar blood flow in comparison with the pulsatile arterial flow. The cardiologist then leads the catheters up to the heart under fluoroscopic guidance. This strategy gives a direct access to the right cardiac chambers. In order to access the left part of the heart, a puncture of the atrial septum is often carried out.

Once inside the targeted chamber, an electrophysiologist first reconstructs the anatomy by leaning the catheter against the inner wall of the heart. To measure the cardiac electrophysiology, two different mapping approaches are available: a contact mapping (like the CARTO EP Contact Navigation System, presented in Fig. 2.11(a)) or a non-contact mapping (like the EnSite Velocity System, presented in Fig. 2.11(b)). The former technique consists in moving the catheter along the wall to capture electrical signals, whereas the latter uses a balloon floating inside the chamber and measuring remotely the surrounding electrical activity. The main loss of accuracy in this procedure arises from the noisy reconstruction of the anatomy. Many uncontrolled parameters (breathing, motion of the patient or catheter discrepancy) can perturb the acquisition.

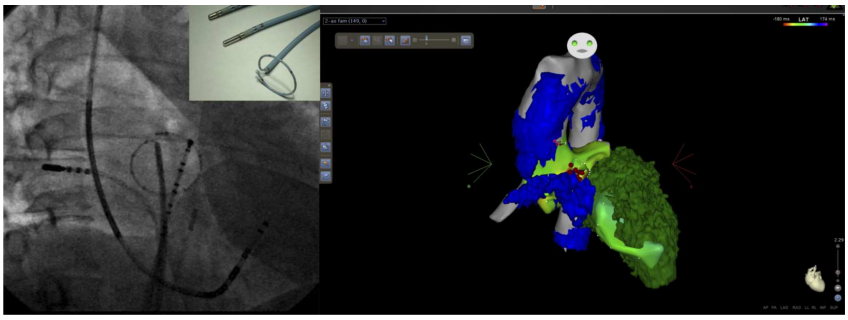

(a) CARTO navigation system: with (left) fluoroscopic images, (middle) the CARTO contact mapping catheters, (right) and the electroanatomical mapping (Images from CHU, Bordeaux)

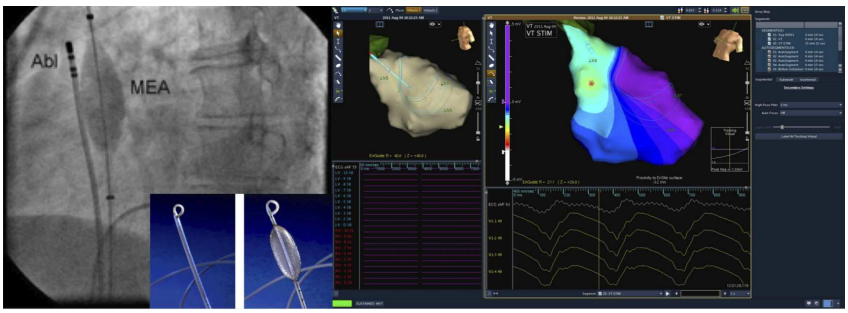

(b) EnSite navigation system: with (left) fluoroscopic images, (middle) the deflated and inflated ballon, (right) and the electroanatomical mapping (Images from KCL, London)

Figure 2.11: Two available systems for electroanatomic mapping

The electrophysiological data available in this work have been acquired using electroanatomic mapping.

Optical mapping This last method is dedicated to *ex vivo* experiments. The heart has to be perfused with a fluid containing voltage-sensitive dye. Once the voltage-sensitive dye are bound to the cardiac cell membranes, they respond to changes in transmembrane potential by changes in excitation and fluorescence spectra. As illustrated in Fig. 2.12, a setup enables to record the electrical activity at the cellular level. Latest progress from Pop et al. (2009, 2012); Rosenbaum et Jalife (2001) proposes a 3D extension of the optical mapping.

2.3.3 Treatment of Arrhythmia

Since a benign cardiac arrhythmia cannot be easily detected, only severe case of arrhythmia are treated. Several therapies exist but can all be considered as cardioversions, i.e. medical procedures aiming at converting the cardiac arrhythmia to a regular sinus rhythm.

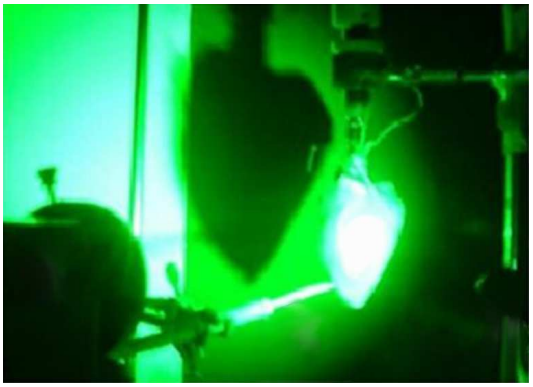

Figure 2.12: Optical mapping setup. With courtesy of Pop et al. (2012)

ICD One treatment of cardiac arrhythmia plans the permanent implantation of an ICD. This programmed device detects arrhythmia and corrects it by delivering a brief electrical impulse to the heart. ICDs are able to revert VF and now also handle VT. Similar to pacemakers, an ICD includes a battery and a wire, usually lodged in the apex of the RV. However, these devices need patient-specific physiological adjustment. In case of frequent trigger of the arrhythmia, wearing an ICD can significantly alter the quality of life by causing anxiety, or depressive symptoms.

For LBBB treatment, a unique type of cardiac pacemaker exists: the Cardiac Resynchronization Therapy (CRT). Up to three leads can be placed in the heart at precise locations. When an asynchronous depolarization is detected, the leads deliver an electrical current with a specific stimulation pattern.

Thermal Ablation For patients with specific arrhythmias (re-entrant VT) suffering from repetitive arrhythmic events, an RF ablation procedure is frequently considered. As for the electroanatomical mapping, a minimally invasive catheterization leads to the heart. Once located, the area responsible or conducting the arrhythmia undergoes permanent damages due to the RF energy delivered by a specific catheter. The ablated region loses its electrical activity, thus preventing the cells from conducting or generating an electrical current. If the procedure succeeds, arrhythmic events should not occur anylonger, thus significantly and permanently improving the quality of life of the patient.

However, the success rate of the procedure remains unsatisfactory: between 50 and 90% of success, whereas the rate of late recurrence amounts to 20 up to 40%. According to Aliot et al. (2009), the long-term success rates of RF ablation in the context of scar-related VT even falls between 30 and 60 %. Authors point out a lack of clinical consensus on the optimum RF ablation

strategy, which could explain these unstable success rates. This conclusion demonstrates the need of new predictive tools providing a substantial guidance in the definition of the optimal ablation strategy.

Even if ablation by RF remains the most widely-used technique in such scenario, other techniques such as cryoablation were recently introduced, as highlighted in Chan (2013). Cryoablation is often attempted because of proximity to sensitive areas, such as coronary arteries. A study around cryoablation simulation is conducted in Talbot et al. (2014b), more information can be found in Appendix A.

Anti-arrhythmic drugs are often prescribed in addition to all these treatments.

2.4 Modeling of the Cardiac Electrophysiology

The ionic exchanges governing cardiac action potentials have been presented in Subsection 2.2.1. Ionic channels open and close during an action potential, so that a local voltage gradient appears within the myocardium. Mathematical models tend to represent the propagation of this electrical wave. Modeling the electrical activity of the heart offers new perspectives, such as using simulation for learning, developing training system for electrocardiology, or even forecasting the optimal treatment to conduct for a specific patient based on electrophysiology simulation.

Research on cardiac electrophysiology models is very active and many mathematical models have been proposed. They can be sorted into three different classes:

- biophysical models, as ten Tusscher et al. (2004), which are complex models including the different ionic concentrations and channels, involving many parameters and simulating the electrophysiology at the cellular scale. The acquisition of the electrical activity using patch clamp improved significantly the development of these ionic models;

- phenomenological models, which are simplified models Aliev et Panfilov (1996); Fenton et Karma (1998); FitzHugh (1961); Mitchell et Schaeffer (2003) derived from the biophysical models, involving less parameters and capturing the action potential shape and its propagation at the organ scale;

- Eikonal models, developed in Keener (1991), which correspond to static non-linear partial differential equations of the depolarization time derived from the previous models. These models cannot accurately account for complex physiological states (such as reentries).

A huge range of models is therefore available from very simple models to more complex models, e.g. dedicated to particular species or regions of the heart. A study carried out in Fenton et Cherry (2008) enumerates the existing models in cardiac electrophysiology, as illustrated in Fig. 2.13. An effort was also given in order to make all these models available based on Garny et al. (2008). Models are implemented using the CellML [2] language.

The first challenge of our doctoral study is to reach fast (close to real-time) simulation of cardiac electrophysiology. In this scope, we focus on phenomenological models including fewer degrees of freedom thus lower complexity.

Phenomenological models Phenomenological models can be classified either as bi-domain or mono-domain models depending on the considered electrical potentials. Based on the conservation law of current and charge (a detailed mathematical description being given in Henriquez (1992)), the bi-domain models represent the evolution of intracellular and extracellular potentials separately. Based on an homogenization from the cellular scale to the organ scale, each bi-domain model can be written as the following reaction-diffusion equations:

$$div(D_i + D_e)\phi_e = -div(D_i \nabla V_m) \quad (2.1)$$

$$div(D_i \nabla V_m) + div(D_e \nabla \phi_e) = -\beta(C_m \frac{\partial V_m}{\partial t} + I_{ion}) \quad (2.2)$$

where ϕ_e is the extra-cellular potential, V_m is the transmembrane potential which equals $V_m = \phi_i - \phi_e$ with ϕ_i the intra-cellular potential. D_i and D_e are respectively the intra-cellular and the extra-cellular conductivity tensors, β is the ratio of surface of membrane per unit volume. In his work, Roth (1992) studied the influence of both intra- and extra-cellular anisotropy on the cardiac muscle. These bi-domain modeling are more especially used in cardiac electrophysiology embedded in a torso, as in Lines et al. (2003). However, one limitation of the bi-domain approach is the associated time-consuming system resolution. Recently, different work, such as Pathmanathan et al. (2010); Pierre (2012), paid a particular attention to this issue.

[2] CellML is an open standard based on the XML markup language. Read more about CellML here: www.cellml.org

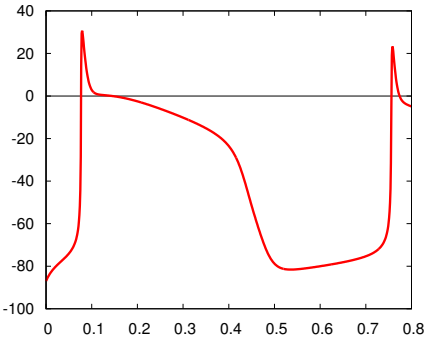

(a) Purkinje fiber model from Noble (1962)

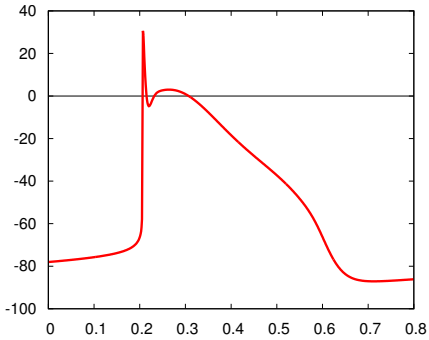

(b) Purkinje fiber model from McAllister (1975)

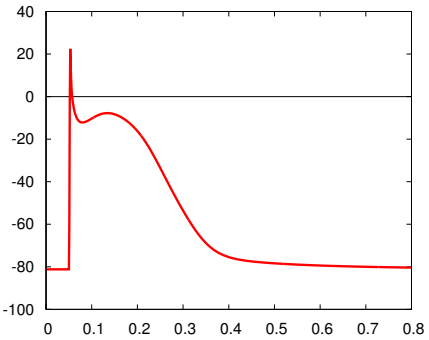

(c) Atrial model from Courtemanche (1998)

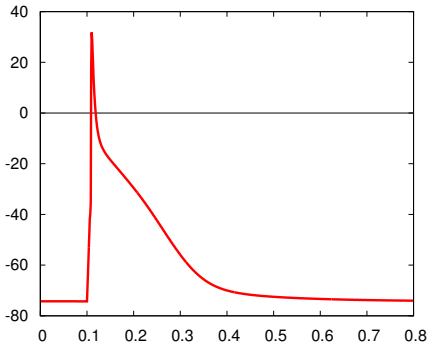

(d) Atrial model from Nygren (1998)

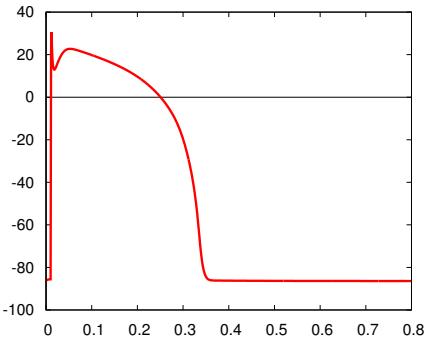

(e) Ventricular model from Ten Tusscher (2004)

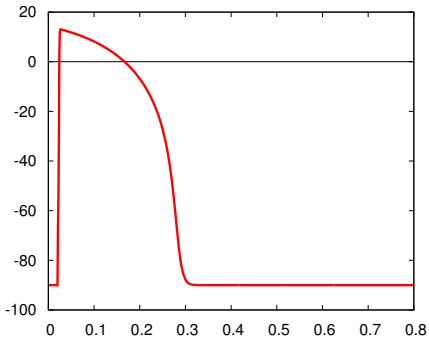

(f) Ventricular model from Mitchell & Schaeffer (2003)

Figure 2.13: Action potential (in mV) computed from (a,b) Purkinje, (c,d) atrial and (e,f) ventricular models using COR [3] against the time (in seconds)

[3]Read more about COR: http://cor.physiol.ox.ac.uk

The second category, mono-domain models, results from a reduction of the bi-domain representation assuming that the intra- and extra-cellular anisotropy ratios are equal. Only expressed according to the transmembrane potential, mono-domain models can be written:

$$\frac{\partial V_m}{\partial t} = div(D\nabla V_m) - \frac{I_{ion}}{C_m} \tag{2.3}$$

where V_m is the transmembrane potential, D the conductivity tensor, C_m is the membrane capacitance and I_{ion} is an ionic current specific to each model. This reduction to one transmembrane potential implies efficient computations while allowing complex pattern of action potential, as demonstrated in Cherry et al. (2003).

The extended mono-domain is an adaptive formulation proposed in Chhay et al. (2012); Clements et al. (2004); Potse et al. (2006) to address the limitations from both mono- and bi-domain, namely the computation cost for the bi-domain model, and the coupling issue between intra- and extra-cellular potential for the mono-domain model. This method involves one reaction diffusion equation (like the mono-domain approach) but includes a reconstruction of the extra-cellular potential (available in the bi-domain approach).

Our electrophysiology model To develop innovative simulations dedicated to teaching, training and therapy planning, a very high level of efficiency must be reached while preserving accuracy. The choice of the electrophysiological model is therefore key to achieve this interactive computation close to real-time and able to faithfully reproduce the patient electrical activity. In the following chapters, the model from Mitchell et Schaeffer (2003) is chosen as our model for electrophysiology simulation and for parameter estimation. This simplified model was derived from the ventricular model from Fenton et Karma (1998). Its main advantages are: (1) its simplicity, since it only includes two differential equations; (2) its physiological parameters making it easier to understand and interpret; (3) its ability to simulate arrhythmia macroscopically thanks to its restitution parameters.

After presenting the different electrophysiology models, and after justifying our choice of model, the Chapter 3 will now focus on the implementation of a real-time electrophysiology based on this Mitchell-Schaeffer model.

CHAPTER 3

Real-Time Cardiac Electrophysiology Computation

Contents

Based on:

Talbot et al. (2013a): H. Talbot, S. Marchesseau, C. Duriez, M. Sermesant, S. Cotin et H. Delingette. Towards an Interactive Electromechanical Model of the Heart. Journal of the Royal Society Interface Focus, vol. 3, no. 2, 2013a

In order to develop an interactive framework for rehearsal and training in the context of cardiac catheter ablation, an interactive and real-time electrophysiology model is required. In the case of severe heart failure, Cardiac Resynchronization Therapy (CRT) is preferred over RF ablation. This chapter considers the case of a Left Bundle Branch Block (LBBB) treated with CRT. The proposed interactive framework relies on two main contributions. An efficient implementation of cardiac electrophysiology is first proposed using latest GPU computing techniques. Second, a mechanical simulation is then coupled to the electrophysiological signals to produce realistic motion of the heart. We demonstrate that pathological mechanical and electrophysiological behaviour can be simulated.

3.1 The Mitchell-Schaeffer model

3.1.1 The Model

As introduced in Section 2.4, there exist several models to describe the ventricular action potential. However, only phenomenological models should be considered regarding our objective of interactive simulation. Indeed, biophysical models characterize the electrophysiology at the cellular scale which implies a high level of complexity and an important computational cost. Eikonal models are efficient algorithms but have difficulty to simulate complex electrophysiology phenomena since they rely on non-physiological parameters.

We choose the Mitchell-Schaeffer (MS) model because of its six parameters that can be physiologically identified. Moreover, it captures well the restitution properties of action potential duration compared to phenomenological models of similar complexity. The action potential shape described by the Mitchell-Schaeffer model in Mitchell et Schaeffer (2003) is given in Fig. 3.1.

The Mitchel-Schaeffer model, derived from the Fenton Karma model Fenton et Karma (1998), has two variables: u the dimensionless transmembrane potential and z a dimensionless secondary variable controlling the repolarization phase. The temporal evolution of these two variables is governed by the following equations:

$$\begin{cases} \partial_t u = div(D\nabla u) + \dfrac{zu^2(1-u)}{\tau_{in}} - \dfrac{u}{\tau_{out}} + J_{stim}(t) \\ \partial_t z = \begin{cases} \dfrac{(1-z)}{\tau_{open}} & \text{if} \quad u < u_{gate} \\ \dfrac{-z}{\tau_{close}} & \text{if} \quad u > u_{gate} \end{cases} \end{cases} \tag{3.1}$$

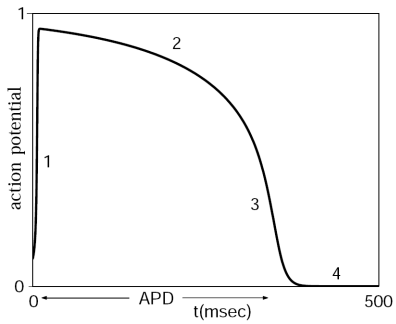

Figure 3.1: Transmembrane potential as described in Mitchell et Schaeffer (2003): (1) depolarization, (2) plateau phase, (3) repolarization and (4) rest potential

The diffusion term is defined by an 3x3 anisotropic diffusion tensor $D = d \cdot diag(1, r, r)$ so that the planar conduction velocity (CV) in the fiber direction is 2.5 times greater than in the transverse plane ($r = \frac{1}{(2.5)^2}$). d is the diffusion coefficient. The parameters τ_{in} and τ_{out} define the repolarization phase whereas the constants τ_{open} and τ_{close} manage the gate opening or closing depending on the change-over voltage u_{gate}. The default values (describing the common action potential) of these parameters are given in Mitchell et Schaeffer (2003) and a simulation of an electrophysiological wave is shown in Fig. 3.2.

The term $J_{stim}(t)$ is the stimulation current applied in the pacing area. Only a region corresponding to the extremities of Purkinje fibers in both ventricles will include this stimulation current to initiate the depolarization wave (in sinus rhythm) in the ventricles. It can be added that a secondary area can also be defined to model stimulation induced by a catheter. For our simulations, we initiate the sinus stimulus during 0.1 ms so that:

$$\int J_{stim}\ dt = 0.2 \Leftrightarrow J_{stim} = 2000\ s^{-1} \tag{3.2}$$

3.1.2 Geometry

Cardiac contractions make the acquisition of the heart geometry more complex. To access this geometrical information, Steady-State Free Precession (SSFP) Magnetic Resonance Imaging (MRI) is usually preferred due to its modification of gradient echo imaging that produces bright blood images with excellent contrast between myocardium and blood. As for the cardiac contractions, motion tracking requires displacement fields obtained through cine-Magnetic Resonance Imaging (cine-MRI) sequences. We apply our interactive framework on both SSFP MRI and cine-MRI sequences.

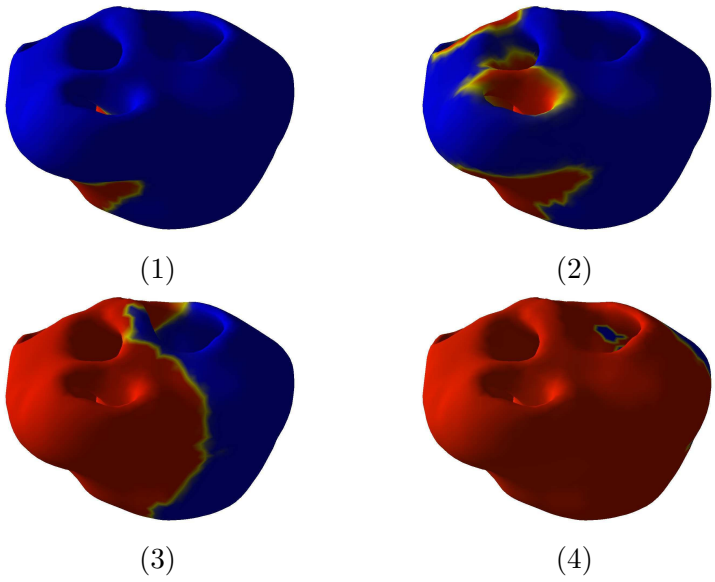

Figure 3.2: Four steps of a depolarization wave propagating inside a FEM mesh: depolarization starts in (1) and the wave then propagates in (2-3) until both ventricles are depolarized (4)

In order to build a patient-specific geometry from these sequences, a preliminary image processing stage is necessary. First, we extract the two ventricles from the SSFP sequence using a semi-automatic segmentation algorithm available in CardioViz3D[4]. This method requires to select landmarks inside and outside the myocardium to fit an implicit algebraic surface. Second, the myocardium mask is meshed using the CGAL software[5]. It results in a tetrahedral mesh made of around 65,500 linear tetrahedra. Both mechanical and electrophysiology models are highly related to the fiber directions. Realistic cardiac fibers are generated by synthetically varying the elevation angle across the myocardium wall, as illustrated in Fig. 3.3. Regarding the LV (including the septum as a part of it), the elevation angle is defined from $+70°$ on the endocardium, to $0°$ at the middle of the endocardium and to $-70°$ in the epicardium. Subsequently, the same method is applied to the RV.

[4]CardioViz3D is an open source software including processing, simulation and visualization tools for cardiac images. It can be downloaded at http://www-sop.inria.fr/asclepios/software/CardioViz3D/

[5]The Computational Geometry Algorithm Library (CGAL) is available at http://www.cgal.org

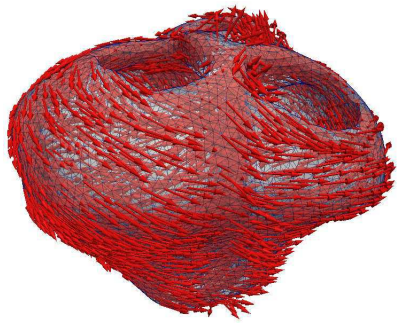

Figure 3.3: View of the heart mesh including the mapped fibers

3.1.3 Numerical Settings

We first focus on the spatial discretization method and the considered integration schemes. We subsequently detail a comparison study on the numerical settings of our simulation. Finally, we explain the way we handle the personalization of the Mitchel-Schaeffer model to make it patient-specific.

Spatial Discretization

As explained in Section 3.1.2, we compute our 3D volumetric mesh from MRI images. The bi-ventricular geometry is meshed with 65,500 linear tetrahedra using CGAL. The Mitchel-Schaeffer model and the diffusion term are implemented using the Finite Element Method (FEM). Using a weak formulation for the integration of diffusion term, it can be shown that natural boundary conditions appear on the surface of the domain. In FE modeling, the use of irregular tetrahedra allows to closely match the acquired images, whereas hexahedra are known to badly reconstruct curved surfaces. More recently, Heidenreich et al. (2010); Lamecker et al. (2009); Oliveira et al. (2012) are focusing on adaptive meshing technique, where the mesh of regions undergoing depolarization are dynamically refined. Here, tetrahedral elements are chosen to mesh the cardiac geometry.

Edge length for cardiac electrophysiology is usually lower than 0.5 mm. However, we use larger tetrahedra (with edge length about 2 mm) in our simulations. Using larger elements means less tetrahedra within the mesh, thus ensuring higher computational performances. The influence of the element size will be studied more in details in Section 3.1.3.

Recent work considered other spatial discretization methods. For instance, Rapaka et al. in Rapaka et al. (2012) present their algorithm applying the Lattice Boltzmann Method to cardiac electrophysiology (LBM-EP). In this work, the authors explain that traditional FEM models could not offer fast

electrophysiology simulations. In this chapter, we propose to use the FEM method on Graphic Process Unit (GPU) as a good alternative to compensate the FEM computational cost.

Integration Schemes

We now detail the integration schemes we considered. In their work Ethier et Bourgault (2008), Bourgault and Ethier present the main schemes used for cardiac electrophysiology. We implemented the Modified Crank-Nicholson/Adams-Bashforth (MCNAB), a second order, semi-implicit scheme. The diffusion term is implicitly integrated, whereas the ionic current term is explicitly computed. Electrophysiology equations can be generalized as follows:

$$\begin{cases} \rho \dfrac{\partial u}{\partial t} = f(u) + g(u,z) \\ \dfrac{\partial z}{\partial t} = h(u,z) \end{cases} \tag{3.3}$$

where g and h denote the ionic functions of the Mitchel-Schaeffer model and f is the additional diffusion term (see Eq. 3.1). The MCNAB scheme describes the integration scheme as shown below:

$$\begin{cases} M\dot{u}_{n+1} = \dfrac{9}{16}F(u_{n+1}) + \dfrac{3}{8}F(u_n) + \dfrac{1}{16}F(u_{n-1}) \\ \qquad\qquad + \dfrac{3}{2}G(u_n, z_n) - \dfrac{1}{2}G(u_{n-1}, z_{n-1}) \\ M\dot{z}_{n+1} = \dfrac{3}{2}H(u_n, z_n) - \dfrac{1}{2}H(u_{n-1}, z_{n-1}) \end{cases} \tag{3.4}$$

where M represents the operator obtained by integrating the term of mass density ρ. G and H denote the operator obtained by integration of the ionic term. F denotes the operator obtained by integration of the diffusion term. In this last system, the index number n refers to the n^{th} time-step. Using the MCNAB, our simulation includes a conjugate gradient coupled with a Jacobi preconditioner in order to efficiently solve the linear system ($\mathbf{A}x = b$). Since the matrix $\mathbf{A}$ is diagonal dominant, the choice of this preconditioner is straightforward. The preconditioned matrix given by the Jacobi can be updated during the simulation in order to take into account conductivity changes (due to thermo-ablation).

We also implemented a full explicit scheme with a Backward Differentiation. In the following, we name it "Explicit-BDF". It can be solved without linear solver. Using the notation from Eq. 3.3, the "Explicit-BDF" scheme is reformulated in Eq. 3.5. A comparison of the isochrones using both integration

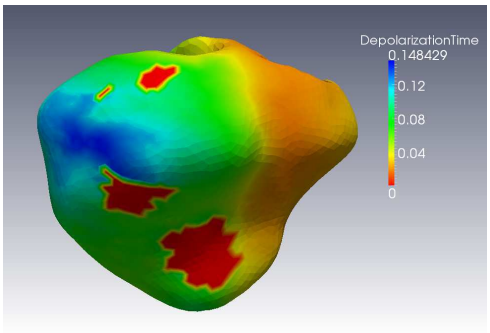

(a) Isochrones using the MCNAB solver

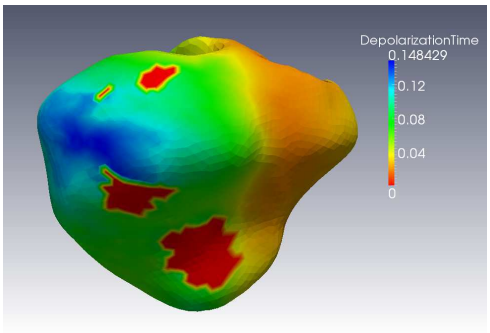

(b) Isochrones using the Explicit-BDF solver

Figure 3.4: Isochrones (in seconds) computed using the MCNAB solver and the Explicit-BDF solver. Red areas represent scars segmented from MR images

schemes is presented in Fig. 3.4.

$$\begin{cases} u_{n+1} = \dfrac{4u_n - u_{n-1}}{3} + \dfrac{2}{3}\left(F(u_n) + G(u_n, z_n)\right)\ M^{-1} \\ z_{n+1} = \dfrac{4z_n - z_{n-1}}{3} + \dfrac{2}{3}\left(H(u_n, z_n)\right)\ M^{-1} \end{cases} \tag{3.5}$$

Numerical Study

To make the best compromise between performance and accuracy, we study each of the numerical parameters of our simulation. The influence of the element size regarding the integration method is considered as well as the influence of the time step.

Element size We first focus on a crucial feature regarding the performance context: the element size. Pathamanathan et al. studied in Pathmanathan et al. (2011) the relationship between the CV and the element size depending on the integration method. We reproduced the 1D planar propagation wave based on the cell model of Mitchel-Schaeffer on a simplified geometry: a 3D cuboid as the one described in Pathmanathan et al. (2011). We implemented a lumped integration and an ionic current integration (ICI) that is studied in Pathmanathan et al. (2011). The lumping method consists in summing all the coefficients of a line onto the diagonal. The ICI interpolates the nodal ionic current linearly on each element. The results using the lumped integration and the ICI are presented in the Fig. 3.5. We obtain the same trend as Pathmanathan et al. in their work. The ICI method is a more accurate technique than the lumped integration. However, the ICI integration method is more computationally demanding than the lumping method. We therefore decide to rely on a lumped integration of the ionic term of the Mitchel-Schaeffer model.

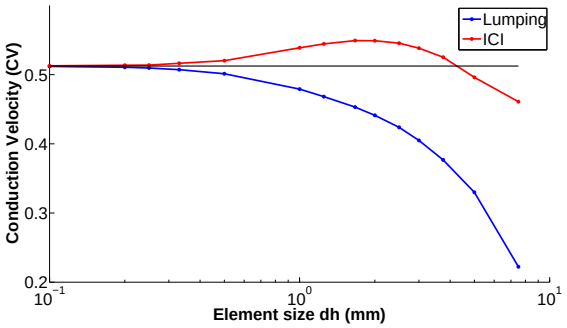

Figure 3.5: Evolution of the conduction velocity (m/s) against the edge size (logarithmic scale in mm)

As presented in Fig. 3.5, the coarser the mesh , the slower the CV (with a constant diffusion coefficient). In our approach, we propose to adapt the nodal diffusion coefficient d in order to fit the patient-specific map of depolarization times. The adapted value of our isotropic diffusion coefficient is noted d_{adapt}, so that the diffusion tensor becomes $D = d_{adapt} \cdot diag(1, 1, 1)$. The integration error due to the lumping approximation would therefore be numerically compensated while benefiting from larger elements, i.e. better performances. This will be done during the electrophysiology personalization detailed later in this subsection.

Time Step As it appears in Fig. 3.1, reaction-diffusion equations as the MS model are very stiff equations. The time integration must consequently use a very small time step to correctly capture the depolarization phase. Depending on the integration scheme used, the time step is limited either due to the diffusion term or due to the ionic term, depending whether the Explicit-BDF or the MCNAB scheme (implicit diffusion) is used. This stability conditions have already been tackled in Ethier et Bourgault (2008) and in Coudière et P. (2006). It can be shown that:

- Using the semi-implicit MCNAB scheme, the ionic current defines the limit of stability:
  $dt \leq \frac{1}{|inf(\partial R)|} = \frac{\tau_{in}\tau_{out}}{\tau_{in}+\tau_{out}} = 0.286\ ms$ where R denotes the ionic term,
- Using the Explicit-BDF scheme, the diffusion term determines the limit of stability. The time step has to be $dt \leq \min\left(\frac{dx}{2\times CV}\right)$ where dx is the characteristic length of the elements and CV is the conduction velocity of the depolarization wave inside this tetrahedron. However, the limit due to the ionic term is still active. This means that dt cannot exceed $0.286\ ms$ whatever the scheme. Using the mesh described

in Section 3.1.2, the stability limit using the Explicit-BDF scheme is $dt < 0.13\ ms$.

These stability conditions are theoretical values. In simulations, it can be noted that the time step dt can in some cases be slightly higher than these theoretical limits.

Simulation Benchmarks To validate our simulations, several benchmarks have been performed using the Explicit-BDF solver and a lumped integration method. First of all, we want to show that using coarse elements (coarser than usual electrophysiology simulation) and increasing numerically the diffusion coefficients (to fit the depolarization times) lead to good performances while keeping the reference action potential shape, Conduction Velocity (CV) and Action Potential Duration (APD). Tests have been carried out on the same simplified geometry than in paragraph *Element Size* (same as in Pathmanathan et al. (2011)) using the model parameters presented in Mitchell et Schaeffer (2003). The beam is 2 cm long and the section area is 4 mm^2. The simulation is initiated on a face at one extremity with a stimulus current (see Eq. 3.2).

Three different simulations are performed:

- The first one is using fine finite elements and fine time step: edge size $dx = 0.1\ mm$, $dt = 0.001\ ms$ and with a reference diffusion coefficient d.
- The second one is using coarse finite elements and very fine time step: $dx = 1\ mm$, $dt = 0.001\ ms$ and using an adapted diffusion coefficient d_{adapt} to fit the same depolarization times as the ones obtained in the first configuration.
- The third one is using coarse finite elements and large time step: $dx = 1\ mm$, $dt = 0.1\ ms$ and using the adapted coefficient d_{adapt} as well.

The resulting action potential shape is shown in Fig. 3.6. The curves show that the chosen time step ($dt = 0.1\ ms$) seems to correctly capture the action potential shape. Moreover, it appears from these results that the use of coarser element ($dx = 1\ mm$) does not affect the action potential shape. Nevertheless, it is known that using coarser elements slows down the propagation phenomenon (see Fig. 3.5). The diffusion coefficients need therefore to be manually adapted to compensate this slowdown.

In Table 3.1, we demonstrate that using large time step (consistently with the stability limit) does not affect neither the CV nor the APD. The edge size used for these computations is $dx = 1\ mm$ and the diffusion coefficient is adapted (d_{adapt}). From the results shown in Table 3.1, it appears that

the time step does not affect the Action Potential Duration (APD) nor the wave propagation (CV) using the semi-implicit MCNAB. However, using the Explicit-BDF scheme, the time step influences the CV. The personalization step will have to be performed with a determined time step if the Explicit-BDF scheme is used.

From now on, the following numerical settings are used for our simulations of the cardiac electrophysiology:

- average edge size is around 2 mm,
- using the MCNAB scheme: time step $dt = 0.2\ ms$, or using the Explicit-BDF scheme: time step $dt = 0.1\ ms$.

Electrophysiology Personalization

MRI images have been acquired on a patient suffering from a Left Bundle Branch Block (LBBB) as well as from post-myocardial infarction scars. The occurrence of a LBBB implies a late activation (and therefore late contraction) of the LV. Patterns of ventricular depolarization are therefore altered which can result in a prolongation of the depolarization, thus leading to a ventricular desynchronization. An electrical asynchronicity often leads to an asynchronous contraction which is detrimental to the cardiac ejection efficiency.

To simulate this patient-specific electrophysiology, we need to personalize the Mitchel-Schaeffer model from patient-specific data, such as contact and non contact intracardiac electrical mapping. We use the method presented in Relan et al. (2011b) to obtain personalized conduction parameters (the diffusion coefficients d) as well as restitution parameters (the time constants

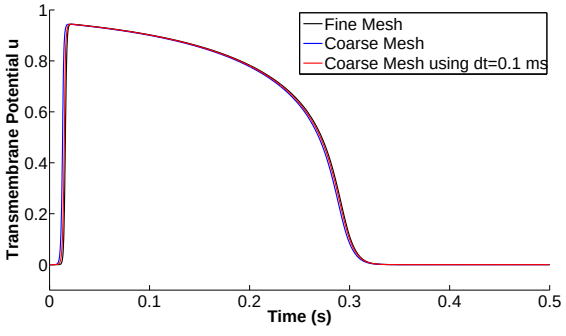

Figure 3.6: Action potential shape of one node located at the distal end of the bar using the three different simulations

Time step (s)	CV - MCNAB (m/s)	CV - Explicit (m/s)	APD (s)
$1e^{-4}$	0.683	0.646	0.279
$5e^{-5}$	0.684	0.667	0.279
$1e^{-5}$	0.685	0.681	0.279
$5e^{-6}$	0.685	0.683	0.279
$1e^{-6}$	0.685	0.685	0.279

Table 3.1: Evolution of the CV and APD depending on dt using a coarse mesh.

τ_{in}, τ_{out}, τ_{open} and τ_{close}). By estimating the diffusion coefficients d, the discretization error can be compensated. This personalization allows us to obtain simulations with less than 10 ms of error with respect to the measured depolarization times, and to also recover the restitution parameters of the action potential duration. The interested reader should refer to Relan et al. (2011b) for more details.

3.2 GPU Implementation

Developing training simulators requires to ensure interactivity during the simulation and to reach performances close to real-time. Different solutions for high performance computing could be envisioned: GPU, multi-CPU, clusters, or even supercomputer.

Recent work are addressing the issue of real-time electrophysiology. First, Bartocci et al. present in Bartocci et al. (2011) a study of five electrophysiology models accelerated using GPU computing, but only a 2D implementation is considered. In Niederer et al. (2011), Niederer et al. propose a GPU version of the TNNP ionic model from ten Tusscher et al. (2004) to simulate cardiac electrophysiology at a cellular scale. However, ionic models require the use of very fine meshes: the simulation therefore remains far from real-time. As stressed by Rapaka and colleagues in Rapaka et al. (2012), the use of classical FEM is more computationally demanding than other nodal method as the LBM electrophysiology. Rapaka and colleagues demonstrate the power of the Lattice-Boltzmann formulation in their work Rapaka et al. (2012). The GPU approach is preferred since the hardware for training needs to be reasonably compact. In this section, we detail our GPU implementation which leads to very interesting performances for cardiac electrophysiology simulations.

3.2.1 Basic GPU Computing

A simulation on GPU uses the graphic card (GPU) of the computer to perform computations instead of using the Central Processing Unit (CPU). However, an efficient implementation on GPU is very complex since every step of the computation has to be cleverly shared out among memory. In our approach, we decided to rely on CUDA toolkit (dedicated for NVIDIA's GPU) to develop a GPU version of our electrophysiology model. The SOFA public framework is already interfaced with CUDA and some codes for GPU computing are made available. Similar computations could be run using OpenCL or other GPU models.

The GPU architecture consists in several multiprocessors able to carry out highly parallel tasks independently. To benefit from the GPU computational power, the complexity of implementation lies in defining an optimal distribution of independent threads while minimizing the memory access. This is far from being trivial and is totally different from a CPU parallel approach (as domain decomposition or other strategies). Single float precision is used since it is sufficiently accurate regarding the variables of the Mitchel-Schaeffer model. Moreover, Bartocci et al. establish in Bartocci et al. (2011) the computational cost of the double precision: it has been estimated twice more computationally demanding than the single float precision.

3.2.2 GPU optimizations

For electrophysiology simulation, the main task is to efficiently implement the computations of the ionic current and the diffusion terms. Using the lumped integration method, the ionic term of Mitchel-Schaeffer is a nodal value (computed at each vertex separately). Therefore this part of the computation is a highly parallel task. This implementation uses classical parallelization methods: each thread is dedicated to one vertex and computes the contribution of the ionic term for this vertex while ensuring a tiled access in memory.

Due to strong neighboring dependencies, the memory access during the computation of the diffusion term is very sensitive. The parallel implementation of the diffusion can lead to writing conflicts: two threads solving two adjacent edges may simultaneously write on the same point. This problem can be automatically handled using the atomic function available in the latest versions of CUDA (> CUDA 2.0). However, these atomic functions are not the most efficient methods. An innovative and very efficient algorithm has been developed in Allard et al. (2011) to tackle the writing conflict issue. Originally designed for deformable finite element equations, we propose a new application of these algorithms to avoid writing conflicts. This technique consists in dividing the diffusion computation into two separate kernels. Before

the computation starts, the vertex-edge topology is saved. During the simulation, the contribution of the diffusion is first computed on all edges. Then, the contribution on each vertex is computed by accumulating the values computed on the edges using the topology information stored previously. For more efficiency, a parallel reduction can be implemented for this last accumulation step. Compared to the atomic functions proposed by NVIDIA, this method presents two main advantages: it appears to be 1.86 times faster than the recent CUDA atomic functions and does not depend on the CUDA version.

Solving the electrophysiology system results in several manipulations of large vectors. This step has a high potential of parallelism since many small operations have to be done on a large number of nodes. We therefore focus on optimizations such as summing vector or equality operations. However, these simple optimizations only offer a limited performance gain.

Minimizing the memory access latency ensures the most efficient simulation. Therefore, the communications between the CPU and GPU during the computation have to be removed. This assumes the implementation of the whole simulation using CUDA. The whole implementation allows a global acceleration of $\times 28$ (using the Explicit-BDF scheme) which is a very satisfactory result. This will be detailed in Section 3.4.

3.3 Electromechanical Coupling

The myocardium is the heart muscle which contracts depending on concentration of free calcium ions in the cells: this is called the myocardial contractility. In this section, we focus on simulating the mechanical behaviour of the heart and defining the electromechanical coupling. Existing models proposed in the last 20 years only differ in the choice of mechanical material, electrophysiology model or electromechanical coupling. Our approach is based on the Bestel-Clément-Sorine model (BCS) Bestel et al. (2001) that has been later improved by Sainte-Marie in Sainte-Marie et al. (2006) and Chapelle in Chapelle et al. (2012).

This mechanical model does not include any stretch-activated ionic channels. This means only a control of the mechanics by the electrophysiology is possible and no feedback from mechanics to electrophysiology. This coupling can be useful to study the mechanical response related to several stimulation patterns. Such an approach has been shown to be predictive in a limited number of heart failure cases in Sermesant et al. (2012). The mechanics-based motion could also be used to generate clinical images from simulation.

3.3.1 The Electromechanical Model from Bestel-Clément-Sorine

The myocardium is a muscle contracting depending on the cellular ion concentrations along preferred directions. The muscle is contracting along fibers which are bundles of myofibril (see Fig. 3.7). These myofibrils can be detailed in series of sarcomeres which are complex structures including:

- thin filaments (actin) and thick filaments (myosin) responsible for the contraction and relaxation,
- elastic filaments (titin) bounding sarcomeres and Z-discs.

In the cardiac extracellular matrix, connecting tissues, mainly made up of collagen and elastin, are surrounding fibers.

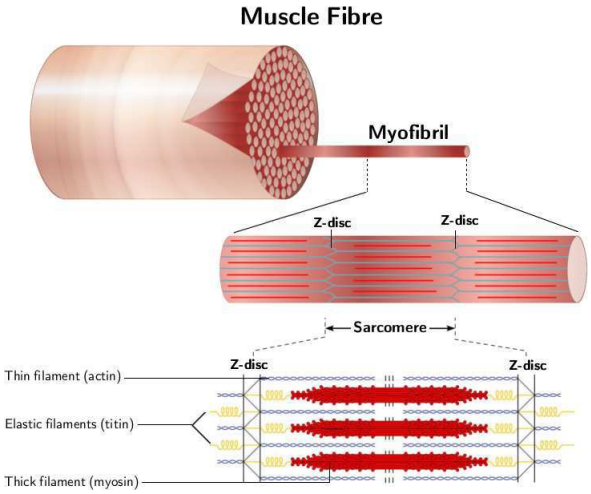

Figure 3.7: Structure of the heart muscle fiber

The study of Sainte-Marie et al. Sainte-Marie et al. (2006) demonstrates the good properties of the BCS model. This model based on a multiscale physiological description is consistent with the laws of thermodynamics.

The BCS model is decomposed into two different parts:

- a passive isotropic visco-hyperelastic component corresponding to the natural elasticity and friction of connecting tissues;
- an active component accounting for the contraction induced by the electrical impulses.

This has been implemented in SOFA Marchesseau et al. (2012a) using an Euler implicit solver and is detailed in the following sections.

Passive Non-Linear Elasticity

The first component of the BCS approach is a passive hyperelastic material modeling the behaviour of the connecting tissues (extracellular matrix). In our simulation, we consider the Mooney-Rivlin model with isotropic properties. Our BCS formulation therefore assumes a transverse isotropy. The strain energy described by the Mooney-Rivlin material is given in the Eq. 3.6.

$$W_e = C_1(\bar{I}_1 - 3) + C_2(\bar{I}_2 - 3) + \frac{K}{2}(J-1)^2 \tag{3.6}$$

where C_1, C_2 are material parameters that need to be determined and K is the Bulk modulus. $\bar{I}_1$ and $\bar{I}_2$ are the isochoric invariants of the right Cauchy deformation tensor noted $\mathbf{C} = \nabla\phi^T\nabla\phi$. The first invariant verifies $\bar{I}_1 = J^{-2/3}I_1$, and the second invariant is $\bar{I}_2 = J^{-4/3}I_2$ where $I_1 = tr\mathbf{C}$, $I_2 = \frac{1}{2}((tr\mathbf{C})^2 - tr\mathbf{C}^2)$ and J is the Jacobian $J = det\nabla\phi$.

Again, we implemented our passive hyperelastic material using the FEM. However, the strain energy is not computed using the classical Galerkin FEM formulation but we propose to use the Multiplicative Jacobian Energy Decomposition (MJED) method presented by Marchesseau et al. in Marchesseau et al. (2010).

This discretization of non-linear hyperelastic materials on a linear tetrahedral mesh leads to faster stiffness matrix assembly than the classical Garlerkin formulation. It is based on the multiplicative decomposition of terms that depend on J from the terms that only depends on the invariants of the Cauchy deformation tensor. The MJED method proved to be about 2.7 times faster than standard FEM on all hyperelastic materials, isotropic or anisotropic.

Active Fiber Contraction

As explained previously, the muscle fibers are bundles of myofibrils. In the BCS mechanical model, we describe the myocardial contraction with an active component that depends on the transmembrane action potential v.

As shown in Fig. 3.8, the active part can be divided into three elements. First, a viscosity element depending on parameter μ is in parallel with the contraction stress tensor noted σ_c. The viscosity element accounts for the energy dissipation due to friction inside the sarcomeres. The resulting stress can be written $\sigma_c = \tau_c + \mu\dot{\varepsilon}_c$.

Second, an elastic component with Young modulus E_s verifying $\sigma_s = E_s\,\varepsilon_s$ is defined in series with the previous elements. This mimics the elastic behavior of the filaments (titin) joining sarcomeres with the Z-discs. The addition of this component leads to a global passive stiffness corresponding to the two passive elements added in parallel, being therefore a transversally anisotropic material with a different stiffness along the fiber direction than in its transverse

direction. This approach corresponds to a classical Hill muscle model which has the advantage to correctly represent isotonic (for ejection and relaxation phases) and isometric (for isovolumetric phases) contraction.

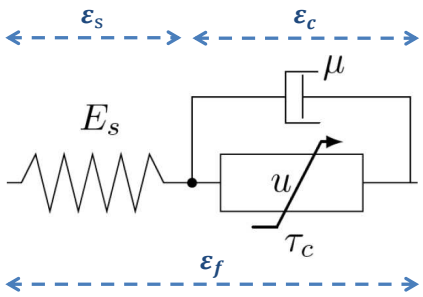

Figure 3.8: Mechanical system of the active fibers

The stress and strain are related by:

$$\begin{cases} \varepsilon_f = \varepsilon_s + \varepsilon_c \\ \sigma_c = \sigma_s \end{cases} \tag{3.7}$$

where ε_f is the projection of the Green-Lagrange tensor $\mathbf{E}$ on the fiber ($\varepsilon_f = f^T\ \mathbf{E}\ f$). Based on the Huxley model Huxley (1957) and on statistical mechanics, the mechanical behaviour of the nanoscopic myosin and actin filaments (see Fig. 3.7) can be characterized by the differential equations (see Eq. 3.8) at the macroscopic scale. These equations link the active stiffness k_c with the active stress τ_c.

$$\begin{cases} \dot{k_c} = -(\mid v \mid + \alpha \mid \dot{\varepsilon_c} \mid)k_c + n_0 k_0 \mid v \mid_+ \\ \dot{\tau_c} = -(\mid v \mid + \alpha \mid \dot{\varepsilon_c} \mid)\tau_c + \dot{\varepsilon_c} k_c + n_0 \sigma_0 \mid v \mid_+ \end{cases} \tag{3.8}$$

where α is a constant related to the cross-bridge release due to high concentration rate, k_0 is the maximum stiffness and σ_0 is the maximum contraction. The reduction factor n_0 enables to introduce the fact that the maximum contraction depends on the fiber strain ε_c. This is called the *Starling effect*. Finally, the "potential" v is a control variable derived from the electrophysiology model (Mitchel-Schaeffer model in our case).

$$\begin{cases} v(t) = k_{ATP} & \text{when } \ T_d \leq t \leq T_d + APD \\ v(t) = -k_{RS} & \text{when } \ t < T_d \ \text{ and } t > T_d + APD \end{cases} \tag{3.9}$$

This variable v is related to a free calcium concentration and varies depending on the depolarization time T_d and the action potential duration APD. k_{ATP} and k_{RS} are kinetic constants, respectively describing the rate of myosin ATPase activity (responsible for contraction) and the rate of calcium pumped back into the sarcoplasmic reticulum (responsible for relaxation).

Haemodynamic Model

The whole BCS model describes the complex mechanical behaviour of the heart tissue. However, the blood flow is not considered in the equation. A haemodynamic model needs to be defined in order to take into account the presence of blood inside the ventricles.

Chapelle et al. propose in Chapelle et al. (2012) a constraint formulation to simulate the blood circulation. The blood circulation in each ventricle (and the associated constraint) can be written in four phases:

- Ventricular filling: the atrial pressure (P_{at}) is higher than the ventricular pressure (P_v) driving blood to flow from the atrium to the ventricle through the open mitral or triscupid valve:
  $q = K_{at}(P_v - P_{at})$ where K_{at} corresponds to a linear law,
- Isovolumetric contraction: the valves close and the ventricle contraction starts:
  $q = K_{iso}(P_v - P_{at})$ where K_{iso} relaxes the usual isovolumetric constraint ($q = 0$),
- Ejection: semilunar (aortic and pulmonary) valves open under the ventricular pressure (higher than the arterial pressure $P_v > P_{ar}$) and the blood ejection occurs:
  $q = K_{ar}(P_v - P_{ar}) + K_{iso}(P_{ar} - P_{at})$ where K_{ar} corresponds to a linear law,
- Isovolumetric relaxation: the valves close while the relaxation starts and the atrium slowly fills up with blood:
  $q = K_{iso}(P_v - P_{at})$.

This constraint is solved efficiently in SOFA using a prediction/correction algorithm, avoiding the addition of the unknown ventricular pressure P_v as a state variable by projecting the corrected nodal velocities directly on the constrained space. The details of such algorithm are explained in Marchesseau et al. (2012a).

3.3.2 Parameter Calibration from Medical Images

In order to better fit the patient-specific heart motion, its deformation field is needed. To compute this motion field, we use the iLogDenons tool developed by Mansi et al. Mansi et al. (2011a) using non-rigid registration. A dense non-linear transformation is applied to our 4D clinical data (cine-MRI data). Using elastic and incompressible regulizers into the registration, this tool even

allows to recover some components of the twist motion of the heart. This motion field is then used to estimate the ventricular volumes in the calibration phase. Indeed, to globally estimate the mechanical parameters, a sensitivity study is first performed to detect which parameters are sensitive to which clinical observations. The Unscented Transform is then applied and allows

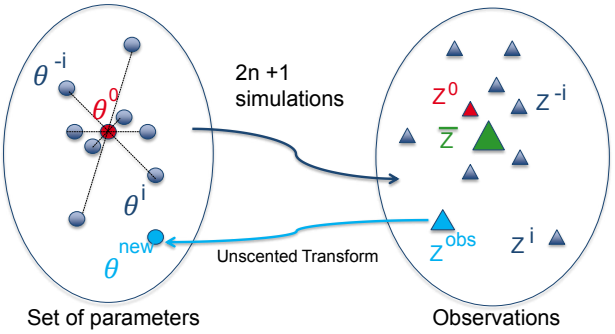

Figure 3.9: Schematic representation of the Unscented Transform algorithm

to estimate 4 parameters in one iteration minimizing the differences between observations extracted from the simulated volume and the measured volume, see Marchesseau et al. (2012a). This algorithm, represented in Fig. 3.9, builds a covariance matrix between the relevant parameters and the observations $\mathbf{Z}$ (in our case the minimum of the LV volume and the minimum and the maximum of its derivative) spread around some initial parameter set θ^0. The new parameters are then found to minimize the difference between the mean simulated observations $\bar{\mathbf{Z}}$ and the measured observations $\mathbf{Z}^{obs}$ with

$$\left(\theta^{new} - \theta^0\right) = \mathbf{Cov}(\theta, \mathbf{Z})\ \mathbf{Cov}(\mathbf{Z}, \mathbf{Z})^{-1}\ \left(\mathbf{Z}^{obs} - \bar{\mathbf{Z}}\right). \tag{3.10}$$

More parameters can be estimated when pressure curves are available, as shown in Marchesseau et al. (2012b).

3.4 Results

3.4.1 Real-Time Electrophysiology Simulation

Performances

As presented in the Section 3.2, the computation of electrophysiology can be accelerated with GPU computing. The hardware used in our GPU simulation is a GeForce GTX580 with 512 cores. The results obtained using GPU are compared with computation made on a CPU Intel Xeon Z3550. Table 3.2 summarizes the performances using either the Explicit-BDF solver or the MC-NAB solver. Performance is evaluated with the "real-time ratio" r_{RT} which

can be expressed as the ratio of the duration of the computation against the time that is simulated.

	Explicit-BDF	MCNAB
CPU	29.39	32.19
GPU	1.05	4.40

Table 3.2: Real-time ratio r_{RT} using CPU or GPU.

It can be noted from Table 3.2 that the performance gain is less important using the MCNAB than using the Explicit-BDF scheme. Solvers (including preconditioner) used with the MCNAB require a lot of matrix-vector multiplications that cost a lot even using GPU. We can see from Table 3.2 that using the Explicit-BDF solver allows to reach real-time performances. This means one cardiac cycle ($\approx 0.92\ s$) can be computed within less than $0.97\ s$.

3.4.2 Coupled Electromechanical Model

Interactive Mechanics

Simulation of the whole mechanical model (BCS model with haemodynamical constraint) is sequentially computed. In our approach, cardiac mechanical contraction is solely driven by electrophysiology, thus ignoring a mechano-electric feedback.

The dynamic equations of motion are solved here, on the same tetrahedral mesh as used for the electrophysiological model. They are discretized using an Euler Implicit scheme and then solved using the Conjugated Gradient algorithm. First, we solve the electrophysiology on a static mesh which gives the action potentials for each node. Thresholding these action potentials gives depolarization times which are used as input for the mechanical simulation. The computation time of the cardiac mechanics during one cardiac cycle requires (for our 65,500 linear tetrahedral mesh) about 10 minutes. Nevertheless, the simulation keeps being tractable which allows to consider efficient personalization strategies. Screenshots of the simulation are shown in Fig. 3.10.

Realistic Simulation

By using a personalized real-time electrophysiology with a calibrated mechanical model, realistic simulation of the cardiac cycle can be achieved. The late activation (i.e. late contraction) due to LBBB can be observed for instance in the Fig. 3.10. Our approach allows also to produce realistic pressure-volume loops as plotted in the Fig. 3.11.

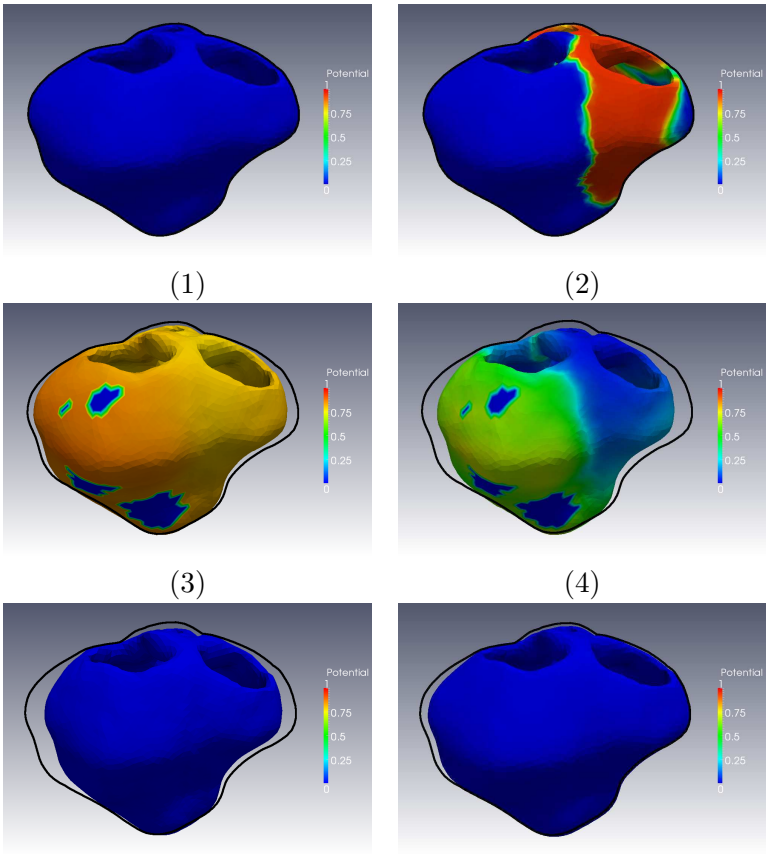

Figure 3.10: Resulting simulation of the electrophysiology and the coupled mechanical model. The cardiac geometry is contracting with the associated dimensionless transmembrane potential in colors compared to the rest geometry (black contours): (1) rest position, (2) depolarization propagates, (3) end of depolarization and contraction starts, (4) repolarization propagates, (5-6) relaxation phase

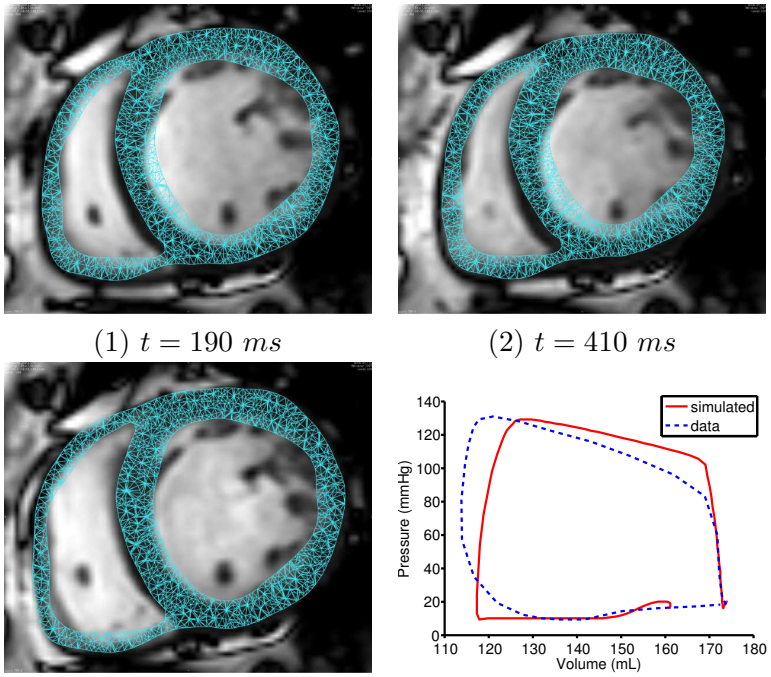

(1) $t = 190\ ms$ (2) $t = 410\ ms$

(3) $t = 720\ ms$ (4) PV loop

Figure 3.11: (Left) Short axis view of the simulated mesh overlaid on the MRI at different times. (Right) Resulting Pressure-Volume loop

CHAPTER 4

Personalization of Electrophysiology Model

Contents

Based on:

Talbot et al. (2014a): H. Talbot, C. Duriez, M. Sermesant, S. Cotin et H. Delingette. Personalization of Electrophysiology Model based on Data Assimilation. to be submitted, 2014a

Personalization of electrophysiology models using clinical data is needed to better understand the mechanism of cardiac arrhythmia. Furthermore, relying on an in silico modeling of a patient-specific electrophysiology, cardiology interns could used personalized models to train on the analysis and diagnosis of the pathology. The development of training simulations based on clinical data is therefore the first significant outcome of the personalization. Today, arrhythmia including VT are frequently treated using RF ablation. As pointed out by Aliot et al. (2009), unstable success rates of the RF ablation reflect a lack of clinical consensus on the optimum RF ablation strategy. As a consequence, the predictive power of patient-specific simulations could also provide a substantial guidance in defining the optimum ablation strategy, since all possible ablation strategies could be tested in silico. In this chapter, we propose an innovative and efficient personalization method based on Kalman filtering.

In this chapter, we focus on three patients suffering from an ischemic cardiomyopathy. The narrowing or occlusion of a coronary artery causes a myocardial hypoxia, which compromises the heart's ability to efficiently pump blood. Ischemic cardiomyopathy may lead to heart failure. Depending on their LV function, patients with ischemic cardiomyopathy may benefit from ICD implant for primary prevention. According to the NICE guidelines detailed in NICE (2007), an electrophysiology study must be conducted in order to determine if an ICD implant would be tolerated. In this scope, patient-specific simulations may help cardiologists to better interpret the arrhythmic complex. More challenging, these predictive computations could even assist the surgeon in the placement of the ICD leads. Patient-specific features, such as depolarization times, repolarization times, CV, APD and their restitution, are extracted from this electrophysiology mapping and then used as input to the personalization process. In this work, we want to assess our electrophysiology model personalization in terms of efficiency and accuracy.

Personalizing a mathematical model consists in estimating the model parameters that best fit experimental or clinical electrophysiology data. If the choice of the algorithm directly impacts the personalization, the choice of the electrophysiology model may also strongly affect the efficiency and the accuracy of the personalization outcome. The complex biophysical models imply high computational cost and a lack of observability of the parameters. Modeling the propagation of the action potential without modeling the action potential itself, the Eikonal formulation appears to be unsuitable for arrhythmia prediction due to the complexity of both the refractoriness and the curvature of the wavefront. With an intermediate complexity and a relative computational efficiency, phenomenological models turn out to be an

interesting compromise. As in Chapter 3, the Mitchell Schaeffer model, which is a phenomenological model, is chosen for our personalization task.

Personalization of electrophysiology models assume to fit patient data, such as ECG or electrophysiology mapping. These intra-operative measurements can then be translated into patient-specific features (depolarization and repolarization times, APD, and restitution parameters) compatible with the mathematical models. In this chapter, our contribution in patient-specific modeling exclusively focuses on the estimation of the apparent conductivity, i.e. the model personalization does not cover the estimation of restitution parameters. Cardiac tissue conductivity is crucial for the detection of conduction pathologies. With respect to Eq. 3.1, the local apparent conductivity is characterized by a diffusion coefficient d.

In this chapter, an exhaustive state of the art regarding the electrophysiology model personalization is first established and discussed. Our personalization method based on data assimilation is then introduced, and finally evaluated and compared to previous work.

4.1 State of the Art

For the last decades, computational modeling of the cardiac electrophysiology has been experiencing a significant progress. In their studies Dössel et al. (2012) and Veneziani et Vergara (2013), the authors emphasize that the transition from synthetic simulations to patient-specific models is now crucial for the clinical application of the cardiovascular modeling.Recent work in the field of parameter estimation dedicated to electrophysiology models already provides very promising results (as in Relan et al. (2011b); Zettinig et al. (2013)).

Electrophysiology model personalization can be basically addressed as an optimization solving an inverse problem. Model parameters are optimized,

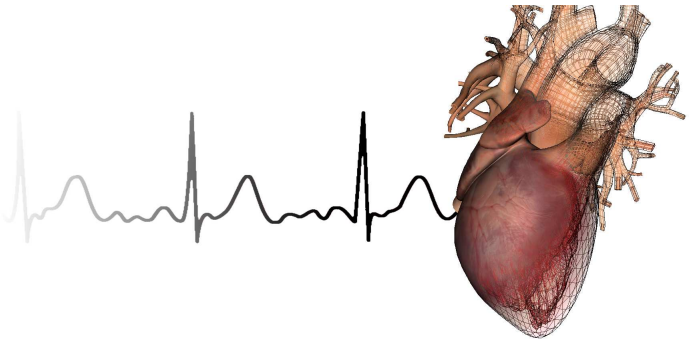

Figure 4.1: Model personalization: from patient data, an optimization of our mathematical models must be performed to reach patient-specific simulations

so that the simulation fits experimental or clinical data. Using our personalization framework to guide the choice of the ablation strategy during the operation strongly constraints the computation time. Many algorithms are at our disposal, but their use in clinical routine may reduce the choice of the optimization method. Indeed, computing a patient-specific set of parameters must be fast, as hours of computation would not be satisfactory. We also want our algorithm to faithfully reproduce and accurately predict the patient electrophysiology. Here, we introduce a classification of optimization methods including a review of electrophysiology model personalization.

4.1.1 Resolution Methods for Personalization

To accurately capture patient-specific electrophysiology, the apparent conductivity is often estimated on a set of regions realizing a partition of the myocardium. To each region R corresponds a diffusion coefficient d_R that needs to be personalized. The anisotropic diffusion tensor D is defined as $D = d_R \cdot diag(1, r, r)$ where r is the anisotropic ratio due to the fiber orientation (see Section 3.1). Our parameter estimation therefore falls into the scope of multidimensional optimization. The cost function to minimize or maximize is denoted $f(x)$ where the vector x contains all regional diffusion coefficients, and N is the the number of regions, thus corresponding to the dimension of the optimization problem. The parameter estimation results in finding the set x^* verifying:

$$x^* = \arg\min_x f(x) \tag{4.1}$$

Optimization methods can be sorted into five categories: methods that compute the gradient of our function $\nabla f(x)$ knowing its analytical form, gradient-free methods numerically evaluating the gradient, stochastic optimization methods, statistical estimation and data assimilation methods.

Gradient or Hessian-dependent Methods Years of research lead to several advanced and well-known algorithms based on the gradient information. Gradient methods are efficient to find local optima, but convergence can be slow in case of ill-conditioned problems. All these algorithms assume to compute the analytical formulation of the gradient (1^{st} order derivative) or even the Hessian (2^{nd} order derivative) of f. Implicitly, the function f must be continuously differentiable and must even be of class C^2 when the Hessian is considered.

Proposed by Hestenes and Stiefel in 1952 (see Hestenes et Stiefel (1952)), the *conjugate gradient method* is maybe one of the most widely used 1^{st} order derivative method. Based on the steepest descend method, the conjugate

gradient optimizes its descent steps by using directions constructed to be conjugate to the previous descent directions, as shown in Fig. 4.2. Let f be a non-linear function and x_0 the initial vector. The first iteration of the algorithm is a simple gradient step with $d_0 = \nabla f(x_0) = \nabla f_0$. Then, at the i^{th} iteration, the optimization evolves such as:

$$x_{i+1} = x_i + \alpha_i d_i \tag{4.2}$$

where the step α_i is determined by any linear search method. Subsequently, a new estimation of the gradient ∇f_{i+1} is performed to build a new descent direction:

$$d_{i+1} = -\nabla f_{i+1} + \beta_{i+1} d_i \tag{4.3}$$

Different methods (Fletcher et Reeves (1964), Polak et Ribiere (1969), and others) exist to compute the term β_{i+1} appearing in the last equation. According to the Fletcheer-Reeves formulation, we have:

$$\beta_{i+1} = \frac{\nabla f_{i+1}^T \ \nabla f_{i+1}}{\nabla f_i^T \ \nabla f_i} \tag{4.4}$$

The main advantage of the conjugate gradient method is that it provides the exact solution of a quadratic function f after N iterations. However, the conjugate gradient may be very expensive for ill-conditioned matrix. In such cases, a precondionning step can be applied before starting the process to improve the gradient descent, but this can be computationally demanding.

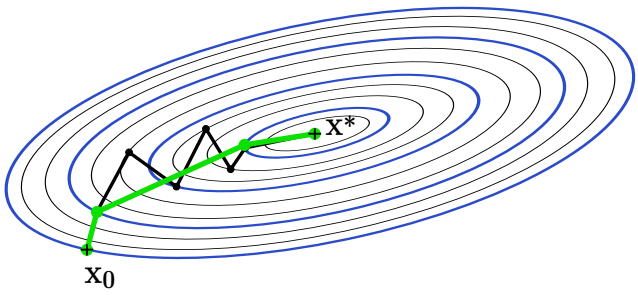

Figure 4.2: Illustration of the conjugate gradient algorithm (green line) compared to the steepest descent method (black line)

As for the conjugate gradient, the *Newton's method* aims at iteratively converging towards x^* from an initial guess x_0. At each iteration, $x_{(i+1)}$ is computed using a second order Taylor so that:

$$x_{(i+1)} = x_{(i)} - H^{-1} f(x_{(i)}) \ \nabla f(x_{(i)}) \tag{4.5}$$

where $Hf(x)$ is the Hessian and $\nabla f(x)$ the gradient of f. The use of the second derivative of f implies that the function needs to be twice-differentiable. The

converge rate of the Newton's method is at least quadratic if $f'(x_i) \neq 0$, else the method only allows a linear convergence rate. To avoid computing this second derivative term, the *quasi-Newton* (also called *variable metric*) *method* was proposed in 1959 and further developed in Shanno (1970). In this last work, Shanno et al. present the BFGS algorithm, widely used nowadays. It iteratively updates an estimation of the inverted Hessian matrix, thus reducing the complexity to $\mathcal{O}(N^2)$.

Gradient-Free Methods The analytical expression of the function f and its derivatives are sometimes not available. To overcome this issue, a second category of algorithms proposes an alternative method: a numerical estimation of the derivatives.

The downhill simplex method, proposed in Nelder et Mead (1965), carries out an optimization while only requiring function evaluations. From a starting guess x_0, the algorithm iteratively looks for its way downhill using $N+1$ evaluation points through the complex N-dimensional topography. These $N+1$ evaluation points create an initial simplex, so that each point i is defined by: $x_i = x_0 + \delta e_i$ where e_i are N unit vectors and δ an estimation of the problem's characteristic length. After evaluation of all $f(x_i)$, the point where the function f is the highest (in case of a minimization, respectively the lowest in case of a maximization) is reflected through the opposite face of the simplex. The reflection step is followed by an expansion or a contraction step depending on the evaluation of f at this new reflected point. Finally, when the optimization reaches the valley floor, the method contracts itself to refine the solution. The optimization process is illustrated in Fig. 4.3. The convergence of this algorithm is robust and its implementation is easy. The method may however fail for complex domain definition or of the optimum is located near the domain border. In these cases, degeneration of the simplex may be observed during the optimization process. With an order of $\mathcal{O}(N^2)$, this method is also known as being slow for high dimensions N.

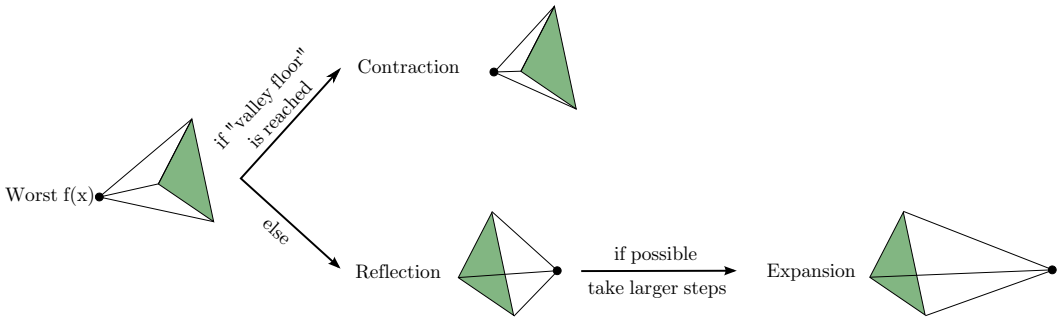

Figure 4.3: Illustration of the downhill simplex algorithm

The downhill simplex method computes a reflection of the worst point to define descent directions, but the set of directions could be updated and optimized all along the process, as referred in direction set methods. In Powell (1964), Powell first proposed a direction set method producing N mutually conjugate directions: the *Powell's method*. Let x_0 be the starting point in the design space and u_i the descent directions, usually defined as $u_i = e_i$ (unit vector in the x_i -coordinate direction). As in the conjugate gradient, non-interfering directions are computed in order to ensure a more efficient convergence. Then, $f(x)$ is successively minimized along the line through x_i in the direction u_i. At the end of the cycle, a minimization of $f(x)$ along the line through x_0 in the direction of $u_{N+1} = x_0 - x_N$ leads to x_{N+1}. The process can thus be repeated. Much faster than the downhill algorithm, the Powell's method requires a smooth function. Proof is given that N $(N + 1)$ line minimization are required to exactly optimize a quadratic form of $f(x)$. The main deficiency of the method therefore resides in the number of iterations required. Furthermore, Powell's method can have directions becoming linearly dependent, thus distorting the optimization process. To overcome this problem, three different solutions are available:

- reinitialize the set of directions u_i to the basis vector e_i after N or $N+1$ cycles,
- reset the directions to columns of any orthogonal matrix,
- or drop the property of quadratic convergence in favor of finding some new directions along narrow valleys (using heuristic schemes).

The step of line minimization required in the Powell's method can be done in several ways. Techniques for line minimization rely on the ability to bracket the minimum between three points A, B and C, such as $f(x_A) > f(x_B)$ and $f(x_C) > f(x_B)$. The simplest method, named the golden section search (similar to the bisection method), consists in evaluating f in a new point D halfway between B and C. As explained in Fig. 4.4, if $f(x_D) > f(x_B)$, the point D is selected to become the new point C. Otherwise, the point B is set to D and A to B. The process repeats itself setting D alternatively on the AB segment and on the BC segment until convergence ($f(x_A) = f(x_B) = f(x_C)$). The golden section search suits any function f. Nevertheless, it can be slow to converge.

More advanced techniques exist for the line minimization problem: the Brent's method developed in Brent (2013) is a popular root-finding algorithm combining the bisection method, the secant method and inverse quadratic interpolation. Given a smooth function f, this method uses a parabola fitting the three points A, B, and C in order to reach the minimum in far fewer

steps. As in the golden section search, a fourth point D is defined but Brent's precept is to set D to the minimum of the parabola. The analytical equation for D is written:

$$x_D = x_B - \frac{1}{2} \cdot \frac{(x_B - x_A)^2 \cdot (f(x_B) - f(x_C)) - (x_B - x_C)^2 \cdot (f(x_B) - f(x_A))}{(x_B - x_A) \cdot (f(x_B) - f(x_C)) - (x_B - x_C) \cdot (f(x_B) - f(x_A))} \tag{4.6}$$

A comparison of the golden section search and the Brent's method is given in Fig. 4.4.

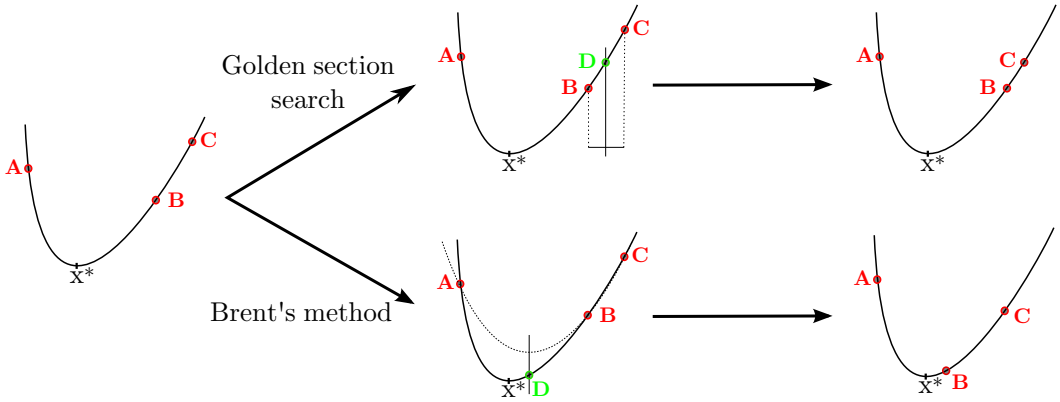

Figure 4.4: Illustration of one iteration of the line minimization process using both golden section search and Brent's method

Both simplex and Powell's methods approximate the function derivatives by a discrete function evaluation. The convergence rate of these methods remains lower than using an analytical expression of the gradient but the computational cost per iteration may be significantly lower. The choice of the evaluation points is decisive in the efficiency of the method.

An alternative to these methods is the automatic differentiation (Bischof et al. (2002); Griewank et Walther (2008)). Instead of computing finite differences to approximate the derivative, the concept of the automatic differentiation algorithm is to consider a computer program as a mathematical function. For any complexity, the function to derive is defined as a composition of elementary function (+, -, $\times$, $\div$ operators). Relying on the chain rule, the derivative of the composition of two functions f and g is written:

$$(f \circ g)' = (f' \circ g) \times g' \tag{4.7}$$

This second gradient-free method prevents from any truncation or approximation error, while preserving a low computational cost. However, issues may arise from the domain definition or from the analysis of complex codes and discontinuities can be introduced due to conditional instructions in the code.

Stochastic Optimization Methods Another strategy consists in solving the optimization problem while ignoring the gradient information. These methods are known as 0^{th} order derivative methods or direct methods. The power of such algorithms is that the process starts from an initial guess and converges towards x^* without deriving or computing gradients. This gradient-free property can be extremely interesting to solve discrete or non-formalized problems. However, all these methods are time consuming: the lack of optimal directions or optimal step size implies an important number of iterations before convergence.

Some optimization methods, that conceptually differ from traditional mathematical programming techniques, have been developed, such as evolutionary algorithms. These methods are labeled as modern or nontraditional methods of optimization. Most of these methods are based on certain characteristics and behavior of biological, molecular, swarm of insects (ants for instance) and neurobiological systems. One of them is the *genetic algorithm* developed in Fraser (1957), which is based on the principal of natural genetics and natural selection. This heuristic method is characterized by mixed continuous-discrete variables, discontinuous and non-convex design spaces. Although randomized, the genetic algorithm is a simple random technique that efficiently explores the new combination according to the available knowledge to produce a new generation with better fitness value. It starts with a set of random samples called a population and each sample is considered as an individual. During the evolution process, at each generation, we determine the fitness value f for each individual and later perform selection, crossover, mutation, elitism to reassure the convergence. Again, computationally demanding samples (individuals) imply huge computation times.

Statistical Estimation None of the methods presented till now includes statistical information. Uncertainty and statistics can be included in all previous optimization methods by defining a Mahalanobis distance, instead of a usual Euclidian distance. Stochasticity may prevent from converging towards local modes. Moreover, it can significantly improve the optimization process with additional information about $f(x)$ and its domain.

The *Monte Carlo method* detailed in Metropolis et Ulam (1949) is a reference in the field of random optimization methods. This algorithm aims at computing a very large number of random samples to estimate the distribution of f seen as an unknown probabilistic entity. The Monte Carlo method can be extremely relevant when no *a priori* on f is available, or when many local minima make the search of the global minimum more complicated. In case of computationally demanding samples (evaluation of f) or constraints regarding the computation time, the use of the Monte Carlo method would

not be recommended.

The Monte Carlo approach gave rise to many computational algorithms solving a Bayesian inference. Methods for Bayesian inference require prior probabilities and a likelihood function. Based on the dynamical analysis of a sequence of sampled data, these methods estimate a posterior probability density function recursively over time according to the Bayes' rule:

$$p(H|E) = \frac{p(E|H) \cdot p(H)}{p(E)} \tag{4.8}$$

where H relates to any hypothesis, E stands for the evidence related to the sampled data, $p(H)$ is the prior probability of H before E is observed, $p(E|H)$ is the likehood, i.e. the probability of observing E given H and $p(H|E)$ is the computed posterior probability. The *particle filters* (also called the sequential Monte Carlo method) first introduced by Handschin et Mayne (1969), or the *Markov chains Monte Carlo* (see the Metropolis-Hastings method in Hastings (1970), or the Gibbs formulation from Geman et Geman (1984)) methods both belong to the class of Bayesian inference.

Data Assimilation Data assimilation arises from the meteorology field, and more generally from geosciences. Data assimilation is an inverse problem aiming at identifying unknown variables using observations of a dynamical system. At each analysis cycle, a forecast from the numerical model (in our case the electrophysiology model) and the assimilated observations are analyzed. This analysis computes the best estimation of the current state regarding the uncertainty in the state and in the observations. An *a priori* knowledge of the probabilistic distribution of the state and observations must be provided. The overall assimilation procedure therefore corresponds to a recursive Bayesian estimation.

Data assimilation estimates the behavior of a dynamic system. At state k, the system can be formulated as follows:

$$x_k = \mathbf{f}(x_{k-1}, u_{k-1}) + w_k \tag{4.9}$$

$$z_k = \mathbf{h}(x_k) + v_k \tag{4.10}$$

in which x_k is the estimated state, z_k the observation of the system and u_k the control vector at time $t(k)$. The state x_k usually includes the state variables of the system and the parameters being optimized. $\mathbf{f}$ corresponds to a (possibly) non-linear system model applied on the previous state. $\mathbf{h}$ is the (possibly) non-linear observation operator. Both w_k and v_k are respectively the independent random noise of the state and of the observations of the system. As in all optimization process, the data assimilation process relies on a cost function

written $J(x)$ to personalize the model. For data assimilation problems, we present here two different methods: a variational and a filtering approach.

First, the variational formulation of data assimilation is a gradient-dependent approach. The concept of variational methods consists in minimizing the cost function $J(x)$. The *3D variational method* (3D-Var) is an algorithm suited to systems which do not depend on time. Its cost function is written:

$$J(x) = (x - x_\diamond)^T P^{-1}(x - x_\diamond) + (z - Hx)^T R^{-1}(z - Hx) \tag{4.11}$$

where P denotes the background error covariance matrix (on the state), R is the observational error covariance matrix, $x_\diamond$ is the *a priori* value of the state, z is the current observation vector and H is the observation operator linearized at the current state x. The optimization of the cost function $J(x)$ requires a gradient descent, so that:

$$x^{(k+1)} = x^{(k)} + \rho^{(k)} \nabla J(x^{(k)}) \tag{4.12}$$

$$\text{with} \qquad \nabla J(x) = 2P^{-1}(x - x_\diamond) - 2H^T R^{-1}(z - Hx) \tag{4.13}$$

The generalization of the 3D-Var method for time-dependent systems is the *4D variational method* (4D-Var). The observations of the system are distributed in time and the cost function then becomes:

$$J(x) = (x - x_\diamond)^T P^{-1}(x - x_\diamond) + \sum_{i=0}^{n} (z_i - H_i x_i)^T R^{-1}(z_i - H_i x_i) \tag{4.14}$$

In the 4D case, the algorithm requires to compute a forward and a backward step to estimate P. As for the conjugate gradient, both 3D and 3D variational formulations are efficient but require the knowledge of H^T to compute the adjoint dynamics. The observation operator transforms the estimated state into estimated observations. In our case, no analytical expression of the transformation of conductivities into depolarizations is available. The variational approach can therefore not be investigated.

The *Kalman filter* (KF) introduced in Kalman (1960) is an alternative method for data assimilation problems, but it focuses on linear systems. Such filters follow a dynamic system through measurements over time and attempt to characterize some parameters modeling the system. In other words, it operates recursively on a stream of measurements (observations) to produce statistically optimal estimates of unknown variables (state). The strength of KF resides in its ability to process data (both observations and state), which includes noise along their uncertainties.

As stated by Rawlings et Bakshi (2006), the original KF is known as the optimal state estimator for unconstrained, linear system with normal distributed

state and observation noise. In KF, the evolution of the dynamic system is described at time $t(k)$ by the same equation than Eq. 4.10. Each iteration of the KF follows two steps:

- the prediction: gives an *a priori* estimation $\hat{x}_{k|k-1}$ of the current state from the previous one $\hat{x}_{k-1}$ through the system model F. The control-input model B_k may be applied to the control vector u_k. The uncertainty regarding the state is defined by the *a priori* predicted estimate covariance $P_{k|k-1}$ including a noise Q_k^{state}.

$$\hat{x}_{k|k-1} = F_k \; \hat{x}_{k-1|k-1} + B_k u_{k-1} \tag{4.15}$$
$$P_{k|k-1} = F_k \; P_{k-1|k-1} \; F_k^T + Q_k^{state} \tag{4.16}$$

- the update: corrects the previous prediction using the present observations (including noise Q_k^{obs}). By comparing the current observations with the estimated ones, we compute the innovation y_k and its uncertainty S_k, see Eq. 4.17. The state correction relies on the Kalman gain K_k (defined in Eq. 4.18) and *a posteriori* updated estimate covariance is calculated for the next iteration, as written in Eq. 4.19.

$$\begin{cases} y_k = z_k - H_k \; \hat{x}_{k|k-1} \\ S_k = H_k \; P_{k|k-1} \; H_k^T + Q_k^{obs} \end{cases} \tag{4.17}$$

$$K_k = P_{k|k-1} \; H_k^T \; S_k^{-1} \tag{4.18}$$

$$\begin{cases} \hat{x}_{k|k} = \hat{x}_{k|k-1} + K_k \; y_k \\ P_{k|k} = (I - K_k H_k) \; P_{k|k-1} \end{cases} \tag{4.19}$$

The original KF is reliable for linear (or almost linear between each observation) systems, and optimal for normally distributed state. However, most of the time, physical systems exhibit non-linear dynamics, i.e. the operators H and F cannot be considered as linear. In such cases, if the frequency of observations is not sufficient to assume the system as linear, the KF is not suitable and methods handling non-linear systems should be preferred.

To apply the KF on non-linear systems, researchers from the NASA developed in Smith et al. (1962) a crude generalization of the KF: the *Extended Kalman Filter* (EKF). The EKF linearizes the non-linear functions $\mathbf{f}$ and $\mathbf{h}$ by expanding them in Taylor series, which gives for F_k and H_k:

$$F_k = \left. \frac{\partial \mathbf{f}}{\partial x} \right|_{\hat{x}_{k-1|k-1}, u_{k-1}}$$
$$H_k = \left. \frac{\partial \mathbf{h}}{\partial x} \right|_{\hat{x}_{k|k-1}}$$

In this extended formulation, the mean propagates through the entire non-linear model but the covariance propagates through the linearization. Even with a perfect model, the EKF may diverge. With a relative complexity, the EKF demonstrated its effectiveness in some cases but it exists many pitfalls where the assimilation fails. Due to its naive linearization, the EKF remains at best an ad hoc solution for complex problem.

The *Unscented Kalman Filter* (UKF) proposed in Julier et al. (1995) overcomes the limitations of both KF and EKF. This filter only differs from both KF and EKF on the prediction step. The UKF strategy avoids a naive linearization by sampling the non-linear response at several points to approximate the prior distribution. An *a priori* estimate of the state and the associated observations are evaluated at sampling points, which are deterministic particles called sigma points. The mean and covariance are therefore expressed using a transformed parameterization. The number, positions, and weights of sigma points is chosen regarding the given starting mean and covariance. Sigma points define a discrete distribution and give a valuable estimation of the Jacobian of the observation. In his thesis, Uhlmann (1995) demonstrates that $N+1$ sigma points are necessary and sufficient for a N-dimensional system. Different sets of sigma points exist, as detailed by Moireau et Chapelle (2011):

- the simplex sigma points: involving the smallest number of necessary sigma-points $(N+1)$ and each point is located on a regular polyhedron around the mean,
- the canonical sigma points: involving $2N$ sigma points aligned with the canonical base,
- the star sigma points: adding the origin to the previous canonical points (involving $2N+1$ points).

UKF thus amounts to a linear regression of the functions $\mathbf{f}$ and $\mathbf{h}$ through some regression points. Then, the EKF correction step is applied. Compared to KF and EKF, UKF is easier to implement and produces prediction of state and covariance more accurate. Moreover, the algorithm uses the minimum set of sigma points to capture the prior distribution, thus preserving a low complexity (from $\mathcal{O}(N)$ up to $\mathcal{O}(2N)$).

4.1.2 Optimization Methods for Electrophysiology Personalization

In addition to the increasing computational power, improvements in cardiac imaging and electrophysiology mapping techniques now allow to generate

patient-specific models. Since the late 2000's, different works focusing on electrophysiology personalization have been conducted. To present these contributions, we use the classification of the previous Subsection 4.1.1.

Gradient-dependent Method From 12-lead ECG, Zettinig et al. (2013) propose a calibration of a Mitchel Schaeffer model using a Lattice-Boltzmann formulation. After coupling the thoracic ECG with the myocardial LBM model, a *multivariate polynomial regression* estimates the model parameters in the right and left ventricles. The inverse problem $x = g(\delta_{QRS}, \alpha)$ is solved, where x is the set of model parameters, δ_{QRS} is the QRS duration and α the mean electrical axis angle. Interesting results are shown with a prediction error less than 5 ms for QRS duration, yet the use of thoracic ECG compromises the modeling of local or complex electrophysiology patterns.

Regarding personalization of the atrial electrophysiology, authors in Weber et al. (2010) propose a gradient-dependent method using either bipolar or unipolar electrode measurements. The signals are approximated by a cosine function, which is then minimized. A sequential quadratic programming algorithm is used to solve the optimization problem. For unconstrained problems, this method reduces to the Newton's method. The average CV error is about 5.4 cm/s corresponding to 5% up to 10% of error and the processing time for 5 s of signal is about 0.5 s. However, as in Zettinig et al. (2013), the method faces the extremely ill-posed problem due to the inverse problem of ECG.

Gradient-free Methods In Liu et al. (2011), Liu et al. propose a modified formulation of the Nelder-Mead algorithm: the MH-NMSS-PSO standing for Modified Hybrid Nelder-Mead Simplex Search and Particle Swarm Optimization. This work aims at estimating parameters of the Bueno-Orovio phenomenological model or minimal model from Bueno-Orovio et al. (2008), but it provides only few interpretable results.

Some significant work recently introduce the Powell's method as personalization tool for electrophysiology models. All three studies Chinchapatnam et al. (2008); Relan et al. (2011a); Sermesant et al. (2009) present a Powell's optimization (using the Brent's method for line minimization) to estimate regional apparent conductivities. Authors choose an Eikonal model to virtually model the endocardial electrophysiology and patient data are acquired by non-contact electrophysiological mapping of the endocardial surface. Chinchapatnam et al. (2008) propose a multilevel approach, thus allowing a subdivision of the region with the maximum value of the regional cost function. Validated on clinical data, the optimization process is applied on a 256 node mesh in about 10 minutes with a root mean square error about 27 ms. Despite the coarseness of the mesh and the relatively large root mean square error, Chinchapatnam

et al. present a proof of concept able to simulate a LBBB pathology and the electrical wave propagation for different pacing modes. Sermesant et al. (2009) apply the parameter estimation developed in Chinchapatnam et al. (2008) to predict the acute effects of CRT. The comparison proposed between measurements and model prediction under sinus rhythm or under two pacing conditions gives promising results. In 2011, Relan et al. (2011a) integrate the personalization of the restitution properties. The Eikonal model is still used to estimate the conductivity parameters but additional parameters related to the action potential duration restitution are estimated using a Mitchell Schaeffer model. This coupled personalization proposed by Relan et al. involves two steps: the Purkinje activity is first approximated using the Eikonal model on the LV endocardial surface; subsequently, the myocardial conductivity is globally estimated for both LV and RV using the MS model. Despite the good prediction of the induction of VT (mean absolute error on depolarization times is about 7.1 ms using the Eikonal model and 18.5 ms using the Mitchell Schaeffer model), this two step process does not guarantee to capture the myocardial activity. Estimation of the apparent conductivity requires about 30 to 40 minutes.

A second set of work (Relan et al. (2009a,b, 2011b)) conducted by Relan et al. concentrates on optical and MRI data from *ex vivo* porcine heart. The three contributions rely on the Mitchell Schaeffer model. The personalization consists in a Powell's optimization again using the Brent's method for line minimization, but the regions are defined using a trust region algorithm. Depending on the regional value of the objective function f, the algorithm can expand the region (if the model fits well the patient data) or conversely contract the region. In the latest version of this work, the mean absolute error regarding the depolarization time is 8.7 ms and the entire computation requires several hours (about 12 hours).

Stochastic Method Based on the Eikonal equation solved using the fast marching method, Camara et al. (2010) apply the genetic algorithm to the personalization of the fast conduction Purkinje system. The authors thus estimate a regional distribution of Purkinje end-terminals. No computation time is mentioned but Camara et al. reached a mean error of about 17 ms regarding the endocardial activation time.

Statistical Methods A probabilistic approach of the model personalization using *Bayesian inference* is proposed by Konukoglu et al. (2011). This probabilistic modeling formulates each parameter of an Eikonal model as a random variable. Each variable is defined by its distribution which reflects its possible range and its expected value. The Bayesian inference computes the posterior

distribution of the parameters for a given set of observations. Since no analytical solutions exist, the posterior distribution is estimated using samples. A spectral representation based on polynomial chaos expansions is preferred. This spectral approach allows to decrease the number of evaluation of the model, i.e. decrease the computational cost. The resulting personalization runs within 5 hours, the root mean square error on endocardial depolarization times is about 15.3 ms and error on epicardial depolarization times amounts to 32.2 ms.

Data Assimilation Both work Wang (2009); Wang et al. (2010) from Wang et al. are the only application of UKF filtering on cardiac electrophysiology. These work estimate patient-specific volumetric myocardial transmembrane potential from given body surface potentials. Two different models are defined: a phenomenological model simulating the transmembrane potential introduced in Luo et Rudy (1991) and another model mapping the transmembrane potential to body surface (torso) potential. In their assimilation process, Wang et al. define as state of the assimilation the transmembrane potential and their observation operator corresponds to their mapping model (transmembrane to body surface potential). Authors attest that local details of arrhythmic activities can be depicted and that arrhythmogenic substrates are identified inside the myocardium. However, the coarseness of the mesh (only 2000 to 5000 nodes) seems not sufficient, even with phenomenological models.

Personalization of mechanical models of the heart are also widely investigated. Moreover, many of these research studies rely on data assimilation techniques. Marchesseau et al. (2012a) consider a reduced-order UKF whereas both Delingette et al. (2012) and Billet (2010) preferred the 4D variational approach. Data assimilation methods will be presented in more detail in the next sections.

4.2 Data Acquisition

In this work, we consider three patients suffering from ischemic cardiomyopathy. All patients underwent an electrophysiology study to determine the effectiveness of an ICD implant. These patient data from Kings College London were made available for research work in the scope of the european project euHeart. This section details how the patient data were acquired and then processed in order to make the model personalization possible.

4.2.1 Image Processing

Two different acquisitions were conducted, both using a Philips Achieva 1.5T. First, the whole cardiac anatomy needs to be reconstructed. To obtain high resolution images, balanced SSFP free-breathing scans were performed for each of the three patients. The isotropic resolution was 1.8 mm^3 and a respiratory motion correction was used for the purpose of segmentation.

Second, as all patients present an ischemic cardiomyopathy, a high resolution imaging of the scars is compulsory. The localization of the scars and grey zones (border areas around scars) are key in the arrhythmic mechanism. The grey zones consist in damaged and healthy tissues which make these areas high potential arrhythmogenic substrates. To acquire scars, a gadolinium contrast agent was injected (Gadobutrol 0.2 mmol/kg) and sequences were recorded 20 minutes post intravenous injection with a voxel size 1.3x1.3x2.6mm^3.

The 3D balanced SSFP images are processed in the open source framework GIMIAS to recover the four chambers of the heart (for more details see Tobon-Gomez et al. (2013)). The signal intensities included in the late Gadolinium enhancement images allow us to threshold the scars and the grey zone, as shown in Fig. 4.6.

4.2.2 Mesh Generation

To be incorporated in our electrophysiology simulation, all patient hearts must be meshed. We use the open source library CGAL, which allows to mesh labeled masks with heterogeneous element sizes, as illustrated in Fig. 4.5. Scar information is labeled in the whole heart image provided by the balanced SSFP, so that we obtain adaptive meshes with refinements in the arrhythmogenic grey zones. Table 4.1 details the structural information of all three meshes.

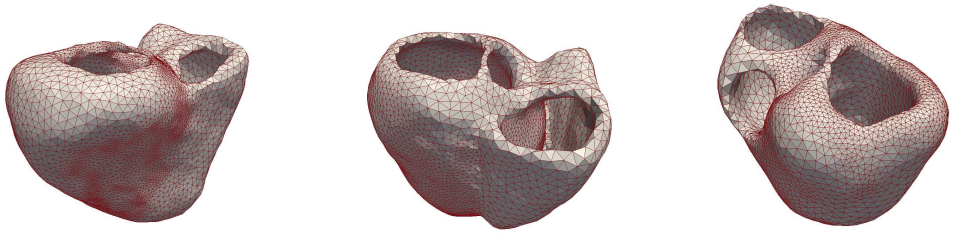

(a) Patient 1 (b) Patient 2 (c) Patient 3

Figure 4.5: Adaptive meshes with local refinements in the scar border zones obtained from patient data (SSFP and LGE imaging)

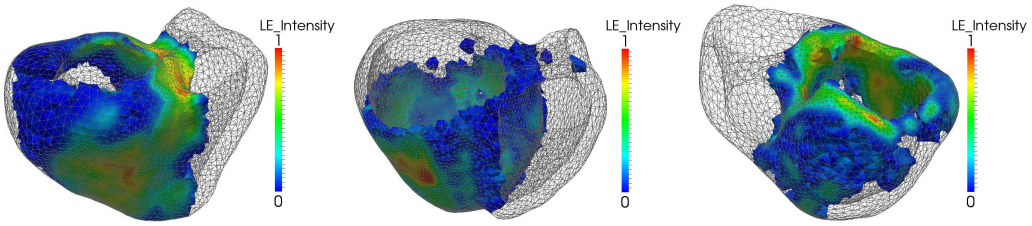

(a) Patient 1 (b) Patient 2 (c) Patient 3

Figure 4.6: Unitary intensity of the late enhancement imaging (Gadolinium), characterizing the scars and grey zones, within the generated meshes

4.2.3 Electrophysiology Mapping

Electrical data were recorded during a non-contact electro-anatomic mapping using a multi-electrode steerable catheter (EnSite Velocity System, St Jude Medical, MN, USA). To reach the LV, the cardiologist must lead the catheter from the femoral artery to the heart via the aorta. Once inside the targeted cardiac chamber, the reconstruction of endocardial electrical potentials can start using the Ensite system. All three patients underwent a VT stimulation procedure following the Wellens protocol proposed in Wellens et al. (1985) in order to determine if an ICD should be implanted.

The electrophysiology catheter tracked in the operating room measured unipolar electrograms. The signals were filtered and then exported using the Ensite Velocity System recorder. An offline signal processing was performed to detect the depolarization times from the QRS window and the repolarization times from the ST window. Finally, the activation resulting from the stimulation at different pacing frequencies (400, 500 and 600 ms) allows us to establish the relationship between the DI of one cycle and the APD of the following cycle. The non-linear equation representing the restitution curves will be later estimated based on these relationships.

	Patient 1	Patient 2	Patient 3
Number of elements	65,198	67,415	61,557
Number of nodes	14,102	14,914	12,162
Smallest edge size (mm)	0.54	1.45	0.48
Largest edge size (mm)	7.00	8.21	9.60

Table 4.1: Structural information of the heterogeneous patient-specific meshes computed using CGAL

4.3 Personalization based on Data Assimilation

In Veneziani et Vergara (2013), the authors emphasize the promising progress in the field of patient-specific optimization. Simulation can provide virtual training for the RF ablation procedure but it also appears to be a promising tool to help cardiologists find an optimum RF ablation strategy. To reach these challenging objectives, clinical requirements must be met. The personalization process along with the simulation must be fast, accurate to reproduce patient's arrhythmia and must involve as few pre-processing as possible.

The works from Wang (2009); Wang et al. (2010); Zettinig et al. (2013) all rely on body surface measurements to personalize their electrophysiology models. As mentioned in Zettinig et al. (2013), using torso acquisitions leads to solve an ill-posed problem transforming thoracic measurements into epicardial signals, which implies to make mathematical assumptions. The intrinsic ill-posed nature of the ECG inverse problem is developed in Zettinig et al. (2013). A promising technology developed by the CardioInsight[6] company computes epicardial 3D electro-anatomic maps using a multi-sensor vest. This innovative vest may help to non-invasively reconstruct an accurate electro-anatomical map. However, this technology is not available in clinical centers yet. Compared to electrical measurements on the torso, the intra-cardiac electrophysiology mapping measures the cardiac activity more closely, although it is prone to noise and perturbations due to the muscle contractions. The study conducted by Steinhaus (1989) highlights these non-ideal conditions of intra-operative recordings.

Relan et al. (2011a) define a proportional relationship between CV and the conductivity (see Eq. 4.40), only valid in the asymptotic case, i.e. for planar depolarization wave. In cardiac electrophysiology, the depolarization wave cannot be assumed planar due to the fiber anisotropy and the tissue heterogeneity. No analytical expression therefore exists between the depolarization times and the conductivity. As a consequence, algorithms requiring the gradient ∇f or the analytical form of f itself should be considered for our optimization process.

To match the MS simulation with the clinical data, samples evaluating the depolarization times given a set of regional conductivities d_R can be computed. Moreover, we can take advantage from the efficiency of the GPU implementation, introduced in Chapter 3, to speed up the optimization process. However, the use of stochastic methods involving many evaluations, i.e. many simulations, may result in a time-consuming optimization.

In this work, we therefore propose to reformulate the cardiac electrophysiology into a recursive Bayesian representation using one of the Kalman

[6]For more information, see: www.cardioinsight.com

filters. Characterized by a strongly non-linear activity, the transmembrane potential could not be accurately approximated by an original KF or an EKF. We choose to rely on the UKF, which has many interesting properties: not only does the UKF handle function non-linearities, but it also presents a low complexity (only $\mathcal{O}(2N)$) while taking into account model and data uncertainties. Applying a Bayesian estimation including a physiological-model-constrained observation model $\mathbf{h}$ may result into a smoothing of the noisy recordings by this electrophysiology model. The assimilation process of model parameters based on the UKF will now be presented.

4.3.1 The Unscented Kalman Filtering

At the end of the Subsection 4.1.1, we carefully compared the UKF with the original KF and the linearization approach of EKF. Now, the UKF algorithm is detailed. As all Kalman filters, the UKF is made up of sequential steps: a prediction (or forecast) and an update (or correction), but it additionally requires an initialization step.

Initialization step From a given initial state x_0, the UKF starts by computing $\hat{x}_0$ the expected value of x_0 and P_0 the initial *a priori* covariance on the state:

$$\hat{x}_0 = E[x_0] \tag{4.20}$$
$$P_0 = E[(x_0 - \hat{x}_0)(x_0 - \hat{x}_0)^T] \tag{4.21}$$

As written in Eq. 4.22, the UKF directly includes the noise on the state (noted w) and the noise on the observations (noted v) within the "augmented" state vector. Uncertainty regarding the noise is also included in an "augmented" covariance matrix, see Eq. 4.23.

$$\hat{x}_0^a = E[x_0^a] = [\hat{x}_0^T \ 0 \ 0]^T \tag{4.22}$$
$$P_0^a = \begin{bmatrix} P_0 & 0 & 0 \\ 0 & P_w & 0 \\ 0 & 0 & P_v \end{bmatrix} \tag{4.23}$$

Both w and v are set to zero at the beginning of the assimilation process. From now on, the algorithm can be generalized at any iteration k. At the k^{th} iteration, the assimilation process computes the square root matrix of the posterior covariance at $k-1$ ($P_{k-1} = S_{k-1} \ S_{k-1}^T$) using a Cholesky factorization.

$$S_{k-1} = chol\left(E[(x_{k-1} - \hat{x}_{k-1})(x_{k-1} - \hat{x}_{k-1})^T]\right) \tag{4.24}$$

Our computation relies on the star configuration including $2N+1$ sigma points: $2N$ canonical points (X^i_{k-1} and X^{i+1}_{k-1}) and the origin (X^0_{k-1}):

$$X^0_{k-1} = \hat{x}^a_{k-1} \tag{4.25}$$

$$X^i_{k-1} = \hat{x}^a_{k-1} + \sqrt{\frac{N}{1-W^0}}\, S^i_{k-1} \quad \text{for } i = 1, \dots N \tag{4.26}$$

$$X^i_{k-1} = \hat{x}^a_{k-1} - \sqrt{\frac{N}{1-W^0}}\, S^{i-N}_{k-1} \quad \text{for } i = N+1, \dots 2N \tag{4.27}$$

where the weight $W^0 \in [-1; 1]$. The associated weights equal:

$$W^i = \frac{1-W^0}{2N} \quad \text{for } i = 1, \dots 2N \tag{4.28}$$

$$\text{respecting} \quad \sum_{i=0}^{2N} W^i = 1 \tag{4.29}$$

Model forecast step The specificity of the UKF resides in the use of the sigma points in the forecasst step. Each sigma point is propagated through the (probably) non-linear process model $\mathbf{f}$:

$$X^{\mathbf{f}}_{k|k-1} = \mathbf{f}(X_{k-1}) \tag{4.30}$$

The mean $\hat{x}^-_k$ and covariance P^-_k of the transformed forecast value $X^{\mathbf{f}}_{k|k-1}$ are computed :

$$\hat{x}^-_k = \hat{x}_{k|k-1} = \sum_{j=0}^{2n} W^j X^{\mathbf{f},j}_{k|k-1} \tag{4.31}$$

$$P^-_k = \sum_{j=0}^{2n} W^j (X^{\mathbf{f},j}_{k|k-1} - \hat{x}^-_k)(X^{\mathbf{f},j}_{k|k-1} - \hat{x}^-_k)^T + Q^{state}_{k-1} \tag{4.32}$$

We then propagate the sigma points through the non-linear observation model $\mathbf{h}$:

$$Z_{k|k-1} = \mathbf{h}(X^{\mathbf{f}}_{k|k-1}) \tag{4.33}$$

The mean $\hat{z}^-_k$ and covariance $P_{\hat{z}_k}$ (innovation covariance) of the resulted transformed observations, as well as cross variance $P_{\hat{z}_k\hat{x}_k}$, are computed:

$$\hat{z}^-_k = \sum_{j=0}^{2n} W^j Z^j_{k|k-1} \tag{4.34}$$

$$P_{\hat{z}_k} = \sum_{j=0}^{2n} W^j (Z^j_{k|k-1} - \hat{z}^-_k)(Z^j_{k|k-1} - \hat{z}^-_k)^T + Q^{obs}_k \tag{4.35}$$

$$P_{\hat{z}_k\hat{x}_k} = \sum_{j=0}^{2n} W^j (X^{\mathbf{f},j}_{k|k-1} - \hat{x}^-_k)(Z^j_{k|k-1} - \hat{z}^-_k)^T \tag{4.36}$$

Update step As in KF, the information obtained in the forecast step can be combined with the new observation measured z_k. It can be written:

$$x_k = \hat{x}_k^- + \mathbf{K}_k(z_k - \hat{z}_k^-) \tag{4.37}$$

where $\mathbf{K}_k$ is the Kalman gain:

$$\mathbf{K}_k = P_{\hat{z}_k\hat{x}_k}(P_{\hat{z}_k})^{-1} \tag{4.38}$$

$$P_k = P_k^- - \mathbf{K}_k\, P_{\hat{z}_k}\, \mathbf{K}_k^T \tag{4.39}$$

As all optimization methods, the choice of initial parameters is crucial in the UKF proceedings.

4.3.2 Region Definition

The estimation of patient-specific model parameters at each node of the cardiac mesh would imply a huge computational cost. To decrease the number of variables while preserving a spatial accuracy, we estimate the model parameters in regions. Some works (see Relan et al. (2009a,b, 2011b)) base their personalization process on the cardiac zones defined by the American Heart Association (AHA zones). For the LV, the number of AHA zones amounts to 17. Since the UKF sampling is based on star sigma points, one single application of UKF would require 35 simulations. Such a high number of samples per iterations may increase the total computation time. Moreover, the 17 regions have no physiological meaning regarding the conductivity. AHA regions do not appear suitable for our problem.

Some previous works presented in Subsection 4.1 also include an adjustment of the regions along the optimization process: trust regions are investigated in Relan et al. (2009a,b, 2011b), whereas multi-level zonal decomposition is chosen in Chinchapatnam et al. (2008); Sermesant et al. (2009)).

In this work, we propose to use regions based on the CV for our optimization. No analytical expression defines a relationship between CV and the MS conductivity d for non-planar waves, but we know that CV is directly impacted by the cell conductivity. We want to take advantage of this *a priori* knowledge on the MS conductivity to create meaningful regions and improve the efficiency of our personalization. Regions are thus constructed depending on the CV extracted from the clinical data, i.e. the measured depolarization times. As shown in Eq. 4.40, CV is obtained by computing the gradient of the depolarization times:

$$\mathrm{CV} = \frac{\partial x}{\partial t_{depo}} = (\nabla t_{depo})^{-1} \tag{4.40}$$

After processing the intra-operative electrical recordings, the depolarization times are computed and projected on the endocardial surface of the reconstructed mesh (see Fig. 4.7(a) to 4.7(c)). To define myocardial regions,

we need to extrapolate the surface CV information through the cardiac wall. To do so, we numerically diffuse the surface CV field through the entire myocardium. However, the values of CV computed from the clinical measurements are scattered. A logarithmic representation of CV is actually used to create the regions, since it better packs the CV values. Using this logarithmic scale, the zones are constructed following an arithmetic progression, i.e. regular subdivision regarding $log(CV)$.

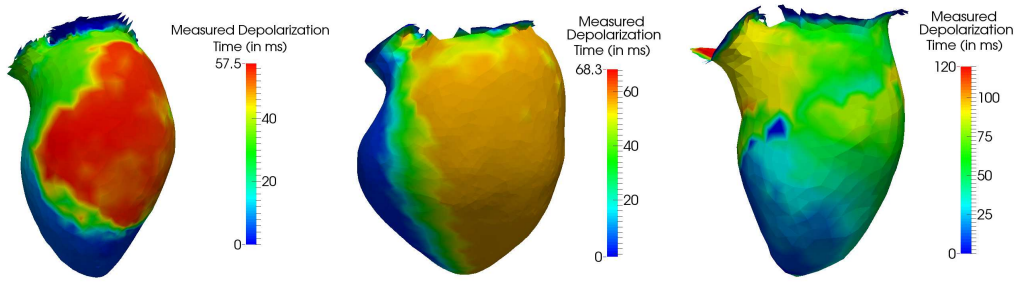

(a) Patient 1 (b) Patient 2 (c) Patient 3

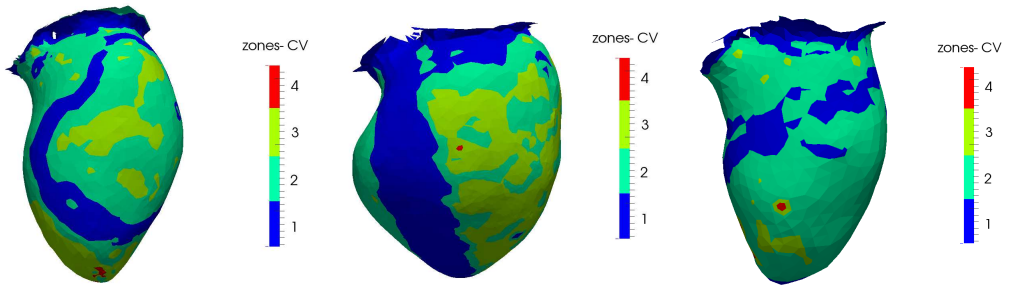

(d) Patient 1: generated regions (N=4) (e) Patient 2: generated regions (N=4) (f) Patient 3: generated regions (N=4)

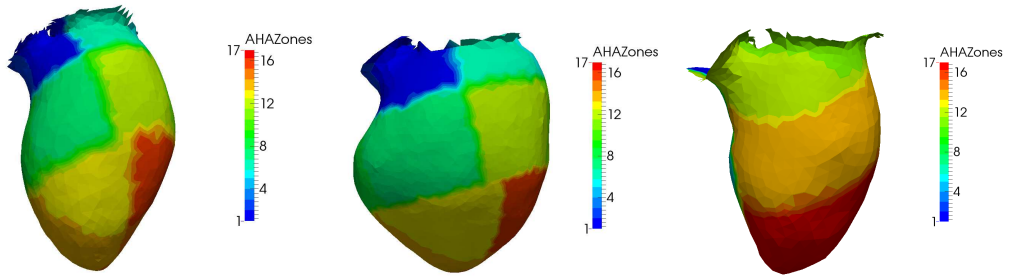

(g) Patient 1: AHA regions (N=17+1) (h) Patient 2: AHA regions (N=17+1) (i) Patient 3: AHA regions (N=17+1)

Figure 4.7: (a-c) Depolarization times mapped on the patients' endocardium computed from electrophysiology mapping; (d-f) Four regions clustered from the CV information; (g-i) AHA regions

Let m be the minimum value of our $log(CV)$ distribution and M its maximum value. The i^{th} zone corresponds to:

$$m + (i-1) \cdot \left(\frac{M-m}{N}\right) \quad < \quad log(CV)_i \quad < \quad m + i \cdot \left(\frac{M-m}{N}\right) \tag{4.41}$$

where $i \in [1, N]$ and N is the number of regions.

In this study, we consider a clustering based on CV involving: 4 zones and 8 zones. Using different numbers of zones enables to analyze their influence on the personalization. The Fig. 4.7(d) to 4.7(f) illustrate 4 zones generated for each patient case. As shown from Fig. 4.7(g) to 4.7(i), American Heart Association (AHA) zones are also constructed to allow a direct comparison with our CV-based regions. These AHA regions divide the heart into regions based on the cardiac axes. Regarding the LV, 17 different regions are segmented. For each of our three patients, the 17 AHA zones for the LV are computed and an additional zone corresponds to the RV (18 regions in total).

4.3.3 Restitution

Electrophysiological restitution defines the property of cardiac tissue to adapt its electrophysiology depending on the heart rate. As noticed in Clayton et Holden (2004), the spatial heterogeneity of the restitution properties (especially APD restitution) has a crucial role in arrhythmogenesis. In order to faithfully model the patient's arrhtyhmia, the restitution parameters need to be estimated. To do so, we apply the optimization method detailed in Relan et al. (2011a).

In Chapter 2, the restitution curves are introduced in Fig. 2.8. They define the relationship between APD and DI. The model from Mitchell et Schaeffer (2003) presents parameters controlling this APD restitution:

$$APD_{n+1} = \tau_{close} \ln \left\{ \frac{1 - (1 - h_{min}) e^{\frac{-DI_n}{\tau_{open}}}}{h_{min}} \right. \tag{4.42}$$

where $h_{min} = 4(\tau_{in}/\tau_{out})$ and n depicts the number of cycles. By explicit derivation, the model even provides:

$$APD_{max} = \tau_{close} \ln \left(\frac{1}{h_{min}}\right) \tag{4.43}$$

Based on Relan et al. (2011a), only APD restitution is computed, i.e. both τ_{open} and τ_{close} are first adjusted on the endocardium to fit the measurements at different pacing frequencies. The ratio h_{min} is kept to the literature value $h_{min} = 0.2$. The τ_{open} and τ_{close} values are finally diffused in order to obtain smooth restitution parameters within the myocardium.

4.3.4 Our Personalization Approach

State and Observation We present here a modified version of the UKF based on the Verdandi library [7]. For each patient, the challenge consists in efficiently personalizing regional conductivities given one depolarization time map recorded intra-operatively. In our application, the state x estimated by the UKF corresponds to the regional conductivities d_R. Since the optimization process may lead to negative values of the conductivities, the state vector does not directly include the regional conductivities, but their absolute values: $x = |d_R|$. Regarding the observation of the system, clinical recordings provide only one set of depolarization times. Although the depolarization wave describes a spatial and temporal evolution of the transmembrane potential, the proposed assimilation process estimates a system with a unique observation vector z including the depolarization times. This application of the UKF can therefore be considered as static.

Operators As we use the UKF in a static way, the time update handled by the function $\mathbf{f}$ becomes $X^f = \mathbf{f}(X) = X$. The non-linear observation model $\mathbf{h}$ corresponds to our electrophysiology simulation in SOFA, which outputs depolarization times using the conductivity information as input. The electrophysiology model is the MS model presented in Chapter 3, which is implemented on GPU, as explained in Section 3.2. From a given set of regional conductivities, the simulation computes a cardiac cycle. As soon as the whole ventricular myocardium is depolarized, simulated depolarization times corresponding to the estimated observation vector $Z_{k|k-1}$ are returned to the data assimilation.

Convergence By applying recursively the UKF, we take advantage of the power of the UKF gain (noted $\mathbf{K}$ in the Eq. 4.38) obtained from the sigma point evaluation to improve iteratively the estimation of x. Following the Eq. 4.37, the state converges towards a final estimation. If both confidences in the state and in the observations remain constant over the iterations, the process undergoes oscillations due to an over-confidence in our measurements. To get an optimal estimation of the state, the error variance regarding the state is progressively decreased to increase the confidence in x over the iterations: as soon as an oscillation effect is detected, a factor ρ is used to damp the *a priori* state covariance P_0. Finally, the optimization process ends using either a maximum number of iterations or a tolerance criterion regarding the

[7] Verdandi is a generic C++ library developed at INRIA for data assimilation. Fore more information: verdandi.sourceforge.net

convergence of x. The structure of the entire iterative algorithm is shown in Fig. 4.8.

Numerical settings Kalman filters are known to be very sensitive to the filter parameters. All features of our algorithm were manually calibrated using the data from patient 1. For the state, the initial regional conductivity is defined as $x_0 = 5 \cdot 10^{-3}$ m^2/s. This set of values simulates a depolarization wave faster than the clinical recordings. A faster depolarization wave implies a stronger constraint on the time step dt to ensure stability (see the paragraph "Time Step" in Subsection 3.1.3). By choosing high conductivities as first state, we ensure stable electrophysiology simulations during the optimization. SOFA simulations run using a time step of $dt = 10^{-5}$ s.

The confidence in the input state is characterized by the *a priori* state covariance $P_0 = 0.2$. For the observations (recorded depolarization times), a high confidence is defined to help our algorithm to converge towards patient-specific data. The *a priori* observation covariance amounts to $R_0 = 10^{-5}$. The damping factor ρ used for a better convergence equals 0.25.

The optimization process is controlled by a tolerance criterion of $\Delta x = |x_{k+1} - x_k| < 10^{-5}$ m^2/s and a maximum number of iterations amounting to 20 iterations. As soon as one of both conditions is reached, the algorithm ends.

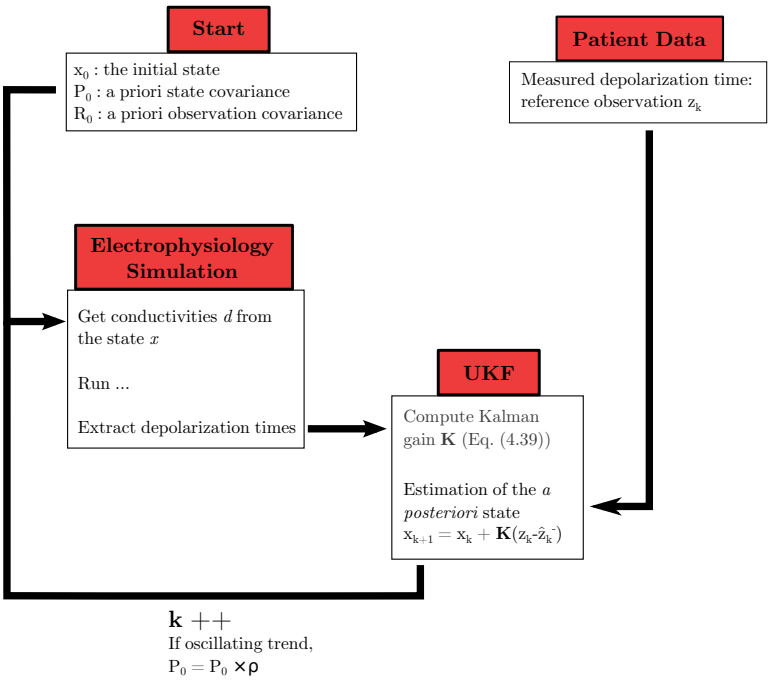

Figure 4.8: Structure of the iterative "static" UKF applied to our patient data in order to personalize regional conductivities

4.4 Results

In this section, the optimization process described previously is applied on the three clinical datasets. All three patients suffer from ischemic cardiomyopathy. During the procedure, the electrophysiologists stimulated the RV apex using an intra-cardiac catheter in order to trigger the arrhythmia. Due to this pacing, a re-entrant VT was induced for both patient 1 and 2. As for the patient 3, no arrhythmic response was triggered due to the electrical catheter stimulation.

The sensitivity of the algorithm regarding the choice of regions and the numerical settings is studied. For each parameter estimation, the resulting conductivities are assessed *in silico*, i.e. if the set of conductivities leads to the same pacing response as the clinical procedure. The results are also evaluated regarding the computation time and the end condition is given. The default settings of the method are defined in Table 4.2.

x_0	$5 \cdot 10^{-3}$ m^2/s
P_0	0.2 $\mathrm{m}^4/\mathrm{s}^2$
R_0	10^{-5} s^2
Sigma points	star ($2N+1$ points)

Table 4.2: Default numerical settings of the UKF-based algorithm

In this section, specific notation is used in the tables to sum up the optimization results. For each patient, the Maximum Depolarization Time (MDT) recorded on the endocardium is given. For the breaking condition,

- "Iter" means that the maximum number of iterations (20) is exceeded,
- "Tol" means that the convergence tolerance is reached $\Delta x < 10^{-5}$ m^2/s.

For the induction response:

- ✓ means that a re-entrant VT was induced during the clinical procedure,
- × means that NO re-entrant VT was induced during the clinical procedure,
- green background: means that the simulation gives the same pacing response as the VT Stim procedure,
- red background: means that the simulation gives the opposite pacing result to the VT Stim procedure.

4.4.1 Sensitivity regarding regions

Firstly, the influence of the optimization regions on the algorithm is detailed. The computation relies on the heterogeneous meshes illustrated in Fig. 4.5. For each patient, we compute three parameter estimations using three different zones:

- 18 AHA zones (noted AHA) displayed from Fig. 4.7(g) to Fig. 4.7(i),
- 8 zones computed from the logarithm of the recorded CV (noted CV-8),
- 4 zones computed from the logarithm of the recorded CV (noted CV-4) shown from Fig. 4.7(d) to Fig. 4.7(f).

Results are given in Table 4.3. The use of 4 zones based on CV give very good results: the convergence is short, the error on depolarization times is low and a re-entrant VT is induced for both patient 1 and 2. The parameters obtained for patient 3 also trigger re-entrant waves after pacing in the RV, whereas no re-entrant VT was noticed intra-operatively. This difference may be explained by the sparsity of the clinical measurements. This dataset reveals a poor sampling regarding the depolarization map, which makes the personalization hazardous.

Compared to these 4 zones based on CV, the personalization using 8 zones gives worse errors. The increasing number of zones requires more iterations and filter parameters need to be adjusted to reach more accurate results. As

	Patient 1 (MDT = 58.0 ms)			Patient 2 (MDT = 72.8 ms)			Patient 3 (MDT = 120.0 ms)		
Zones	AHA	CV-8	CV-4	AHA	CV-8	CV-4	AHA	CV-8	CV-4
Mean error (ms)	9.38	10.2	9.99	11.2	10.2	8.47	27.1	24.3	16.2
Max error (ms)	36.2	48.2	50.8	34.3	37.7	35.6	97.7	97.5	91.6
Computation Time (min)	63.1	34.7	20.5	68.1	28.6	16.3	79.3	32.2	18.4
Breaking condition	Iter	Iter	Tol	Tol	Tol	Tol	Tol	Tol	Tol
Able to reproduce re-entrant VT	✓	✓	✓	✓	✓	✓	×	×	×

Table 4.3: Influence of the type and the number of zones on the error regarding the depolarization times, on the computation time and on the ability to reproduce the VT-Stim protocol

indicated in Table 4.3, the conductivities resulting from these 8 zones allow to recreate the same arrhythmic activity as the VT Stim procedure.

As expected, the state in AHA zones evolves to minimize the error on depolarization times, but the lack of physiological meaning prevents from faithfully mimicking the patient electrophysiology. Consequently, the error on the depolarization times remains important and no re-entrant waves can be reproduced *in silico*.

4.4.2 Other numerical parameters

The accuracy and the efficiency of the algorithm may depend significantly on the UKF parameters. This subsection concentrates on the influence of each UKF parameter: the input state x_0, the *a priori* state covariance P_0, the *a priori* observation covariance R_0, and the sigma points. In the remainder, sensitivity regarding the numerical settings of the optimization is studied only using the 4 CV-based regions and using the patient 1 dataset (for which a re-entrant VT was induced intra-operatively).

Input state First, three different initial conductivity values are tested. The first configuration defines an identical low conductivity $x_0 = 0.2 \cdot 10^{-3}$ m^2/s in the four regions. The second computation uses an identical high conductivity $x_0 = 5 \cdot 10^{-3}$ m^2/s in the four regions. The third initial state takes advantage

	$x_0 = \{0.2, 0.2, 0.2, 0.2\}$	$x_0 = \{5, 5, 5, 5\}$ ***default***	$x_0 = \{2, 4, 6, 8\}$
Mean error (ms)	10.3	9.99	9.99
Max error (ms)	49.7	50.8	49.2
Computation Time (min)	28.4	20.5	16.9
Breaking condition	Tol	Tol	Tol
Final regional conductivities (in 10^{-3} m^2/s)	$x(1) = 0.12$ $x(2) = 1.36$ $x(3) = 3.02$ $x(4) = 1.61$	$x(1) = 0.13$ $x(2) = 0.96$ $x(3) = 5.26$ $x(4) = 5.46$	$x(1) = 0.13$ $x(2) = 1.04$ $x(3) = 5.19$ $x(4) = 8.04$
Able to reproduce re-entrant VT	✓	✓	✓

Table 4.4: Influence of the input state x_0 including the initial regional conductivities in 10^{-3} m^2/s (only on patient 1)

of the *a priori* knowledge on the CV-based regions. Since the regions are clustered depending on the local CV, a low conductivity is associated to the low-CV zone, respectively a high conductivity is set for the high-CV zone. The third state equals $x_0 = \{2, 4, 6, 8\} \cdot 10^{-3}$ m^2/s. The Table 4.4 shows the output results.

Compared to the default configuration ($x_0 = 5 \cdot 10^{-3}$ m^2/s), starting from a lower conductivity ($x_0 = 0.2 \cdot 10^{-3}$ m^2/s) causes slower depolarization waves and therefore longer computation time. Moreover, the initial state using $x_0 = 0.2 \cdot 10^{-3}$ m^2/s is far from the solution and no re-entrant VT is simulated using the resulting conductivities. To obtain better results than those presented in Table 4.4, the *a priori* state covariance should be increased to improve the convergence of this first configuration.

From this table, it also appears that defining an initial state, of which conductivities are related on the measured CV, allows faster convergence rate: the third configuration only requires 16.9 minutes of computation while reproducing the re-entrant VT by pacing in the RV.

***A priori* state covariance** The influence of the *a priori* state covariance is now detailed. The Table 4.5 presents the results using three different covariance values: $P_0 = 0.05$ m^4/s^2, $P_0 = 0.2$ m^4/s^2 and $P_0 = 0.5$ m^4/s^2. Defining a low *a priori* state covariance $P_0 = 0.05$ m^4/s^2 corresponds to a high confidence in the initial state. The UKF produces only small variations of x and the algorithm needs therefore more iterations to converge. In 20 iterations, the resulting state does not allow to simulate the induction of a re-entrant arrhythmia.

Conversely, a high *a priori* state covariance amounts to a low confidence in the state. The algorithm evolves faster away from the initial guess. The resulting set of conductivity succeeds to reproduce the re-entrant *in silico*. However, an excessively high *a priori* state covariance would lead to an unstable behavior diverging from the solution.

***A priori* observation covariance** After considering the state, we now focus on the influence of the *a priori* observation covariance. The Table 4.5 presents the results using three different covariance values: $R_0 = 10^{-4}$ s^2, $R_0 = 10^{-5}$ s^2 and $R_0 = 10^{-6}$ s^2. Compared to our default value $R_0 = 10^{-5}$ s^2, the first column increases the *a priori* observation covariance up to 10^{-4} s^2, which means a lower confidence in the observations. This implies smaller evolutions of the state at each filtering step, thus slowing down the convergence. Since the resulting state remains far from the solution, no re-entrant VT are simulated.

Decreasing the *a priori* observation covariance depicts a higher confidence in the observations. The state will undergo larger changes, which accelerates

	$P_0 = 0.05$	$P_0 = 0.2$ ***default***	$P_0 = 0.5$
Mean error (ms)	10.9	9.99	9.96
Max error (ms)	50.1	50.8	50.8
Computation Time (min)	18.6	20.5	17.7
Breaking condition	Iter	Tol	Tol
Final regional conductivities (in 10^{-3} m^2/s)	$x(1) = 3.01$ $x(2) = 0.75$ $x(3) = 4.04$ $x(4) = 5.23$	$x(1) = 0.13$ $x(2) = 0.96$ $x(3) = 5.26$ $x(4) = 5.46$	$x(1) = 0.14$ $x(2) = 0.91$ $x(3) = 6.06$ $x(4) = 5.67$
Able to reproduce re-entrant VT	✓	✓	✓

Table 4.5: Influence of the *a priori* state covariance P_0 in m^4/s^2 starting with $x_0 = \{5, 5, 5, 5\} \cdot 10^{-3}$ m^2/s (only on patient 1)

	$R_0 = 10^{-4}$	$R_0 = 10^{-5}$ ***default***	$R_0 = 10^{-6}$
Mean error (ms)	11.2	9.99	10.5
Max error (ms)	50.5	50.8	49.5
Computation Time (min)	17.3	20.5	21.1
Breaking condition	Iter	Tol	Iter
Final regional conductivities (in 10^{-3} m^2/s)	$x(1) = 4.14$ $x(2) = 0.99$ $x(3) = 2.69$ $x(4) = 5.07$	$x(1) = 0.13$ $x(2) = 0.96$ $x(3) = 5.26$ $x(4) = 5.46$	$x(1) = 1.96$ $x(2) = 0.56$ $x(3) = 8.80$ $x(4) = 8.94$
Able to reproduce re-entrant VT	✓	✓	✓

Table 4.6: Influence of the *a priori* observation covariance R_0 in s^2 starting with $x_0 = \{5, 5, 5, 5\} \cdot 10^{-3}$ m^2/s (only on patient 1)

the convergence of the algorithm. As for the *a priori* state covariance, an excessive value of R_0 would make the algorithm diverge: here $R_0 = 10^{-6}$ s^2 gives an over-confidence in the observation, and the diverging optimization does not

allow to simulate the ventricular re-entrant waves observed in operation.

	Simplex (N+1)	Canonical (2N)	Star (2N+1) ***default***
Mean error (ms)	10.0	10.0	9.99
Max error (ms)	48.6	50.7	50.8
Computation Time (min)	9.45	16.6	20.5
Breaking condition	Tol	Tol	Tol
Final regional conductivities (in 10^{-3} m^2/s)	$x(1) = 0.13$ $x(2) = 1.17$ $x(3) = 5.02$ $x(4) = 5.42$	$x(1) = 0.13$ $x(2) = 0.98$ $x(3) = 5.25$ $x(4) = 5.46$	$x(1) = 0.13$ $x(2) = 0.96$ $x(3) = 5.26$ $x(4) = 5.46$
Able to reproduce re-entrant VT	✓	✓	✓

Table 4.7: Influence of the sigma points starting with $x_0 = \{5, 5, 5, 5\} \cdot 10^{-3}$ m^2/s (only on patient 1)

Sigma points In Table 4.7, all different distributions of sigma points seem to provide very similar results. All the estimated conductivies reproduce a re-entrant VT after pacing in the RV. However, since the number of samples depends on the chosen distribution, the type of sigma points influences the computation time. The simplex distribution involves $N + 1$ sampling points, thus allowing a shorter computation time compared to the canonical points requiring $2N$ evaluations, where N denotes the number of zones. Regarding the efficiency of our method, the distribution of sigma points appears as an important factor.

4.4.3 Performances

CPU/GPU optimization We finally propose to compare the performance of the algorithm using the GPU electrophysiology model with a full-CPU version. Using the default parameters of Table 4.2 and the 4 zones computed from the recorded CV of patient 1, the GPU version runs within 20.5 minutes whereas the CPU version requires 49.1 minutes. The GPU electrophysiology simulation therefore allows a speedup of about $\times 2.4$ compared to a classical CPU implementation.

	Patient 1	Patient 2	Patient 3
Personalized regional conductivities (in 10^{-3} m^2/s)	$x(1) = 0.13$ $x(2) = 0.98$ $x(3) = 5.26$ $x(4) = 5.46$	$x(1) = 0.09$ $x(2) = 1.26$ $x(3) = 3.85$ $x(4) = 4.94$	$x(1) = 0.01$ $x(2) = 0.10$ $x(3) = 0.97$ $x(4) = 4.65$
Time step (s)	$2.5 \cdot 10^{-5}$	$1.05 \cdot 10^{-4}$	$1.85 \cdot 10^{-4}$
Real time ratio	6.57	1.71	0.85

Table 4.8: Performance results of our three patient-specific electrophysiology simulations using our GPU implementation presented in Chapter 3

Patient-specific simulation The personalization method using 4 zones based on CV is applied on the three patients using the parameters described in Table 4.2. The personalized regional conductivities are then given to the MS model implemented on GPU. The performance study is detailed in Table 4.8.

Regarding the patient 1, the recorded depolarization is very short (about 58 ms), i.e. the conduction velocity is locally high, which strongly constraints the time step for stability reasons. The resulting simulation presents a performance far from real-time. Patients 2 and 3 have a slower ventricular activation, respectively 72 and 120 ms. The time step can be consequently adapted and both simulation are real-time (patient 3) or close to real-time (patient 2).

4.5 Conclusion

In this chapter, we present a personalization method of our MS electrophysiology model based on an UKF. After detailing the existing methods, the UKF is preferred since this data assimilation algorithm does not require any gradient information. The MS conductivity is thus optimized by regions created from the intra-operative CV information. Once calibrated, the iterative application of the UKF reaches a good accuracy compared to previous work with an error of 9.23 ms in average regarding the depolarization times. The more accurate process was proposed by Relan et al. (2011a) with an error of 7.1 ms using the Eikonal model and 18.5 ms using the Mitchell-Schaeffer model. Other previous work were presenting errors on depolarization times higher than 15 ms. Moreover, our personalization succeeds to simulate the re-entrant VT triggered by pacing in the RV for patient 1 and 2. Results for patient 3 present higher errors and simulates a re-entry whereas none was obtained during the operation. This can be explained by the poor quality of

the input measurements.

With the low complexity of the UKF and the computational efficiency of our GPU electrophysiology model, the parameter estimation requires less than 10 minutes to compute myocardial conductivities. This estimation of the myocardial conductivity outperforms previous work in term of efficiency: multizonal personalization from Relan et al. (2011a) requires from 30 to 40 minutes, the Bayesian inference from Konukoglu et al. (2011) requires 5 hours and the Powell's optimization from Relan et al. (2011b) runs in about 12 hours. Using the regional MS conductivities given by the personalization, the patient-specific simulations run in real-time or close to real-time. Only the personalized simulation of patient 1 is significantly slower than real-time due to his fast depolarization pattern. The personalized electrophysiology of each patient is illustrated from Fig. 4.9 to Fig. 4.11.

In the future, the sensitivity of the algorithm regarding the mesh refinement will be assessed using different meshes. Afterwards, our personalization approach should be applied on more patients and on patients suffering from various types of arrhythmia. The performance could also be improved by integrating the recent multithreading approach now available in Verdandi.

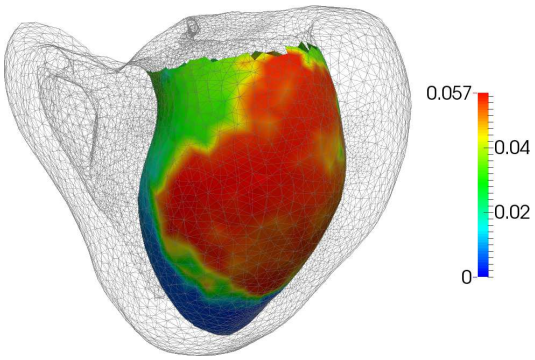

(a) Measured depolarization times (s)

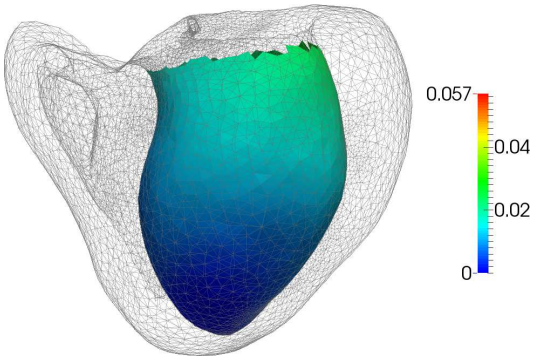

(b) Simulated depolarization times before optimization (s)

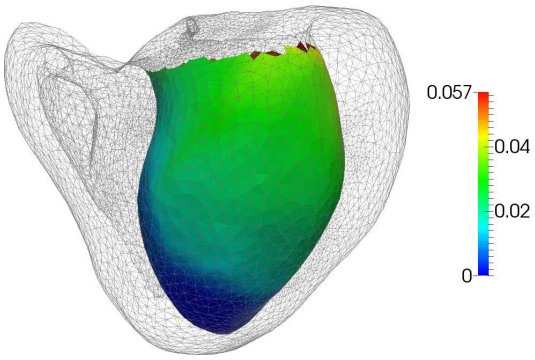

(c) Simulated depolarization times after optimization (s)

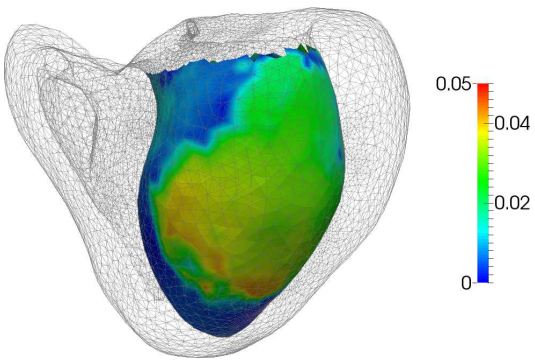

(d) Error map on depolarization time (s)

Figure 4.9: Evaluation of the personalized simulation: Patient 1

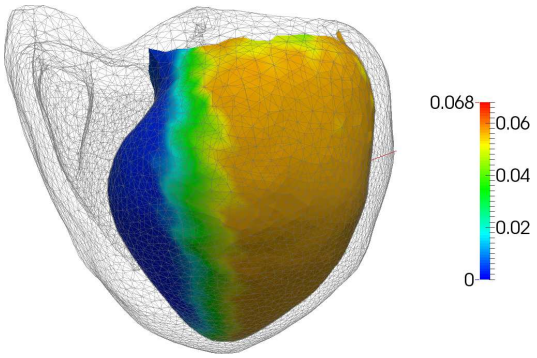

(a) Measured depolarization times (s)

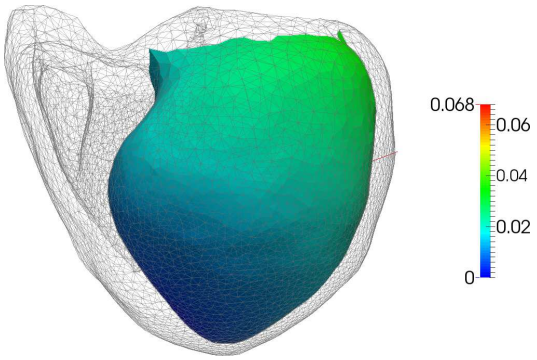

(b) Simulated depolarization times before optimization (s)

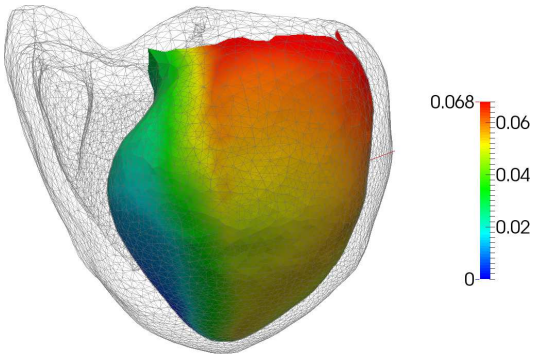

(c) Simulated depolarization times after optimization (s)

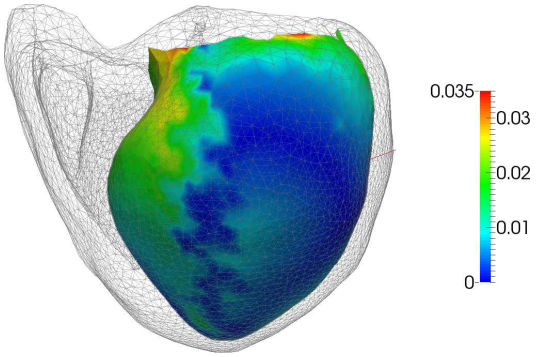

(d) Error map on depolarization time (s)

Figure 4.10: Evaluation of the personalized simulation: Patient 2

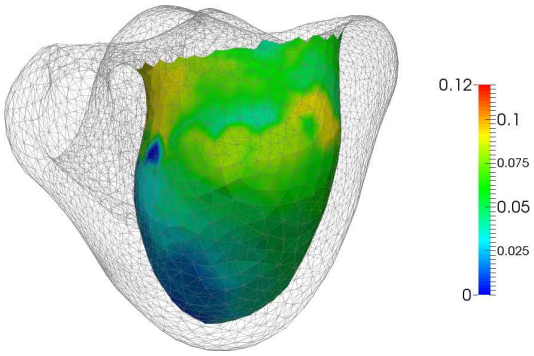

(a) Measured depolarization times (s)

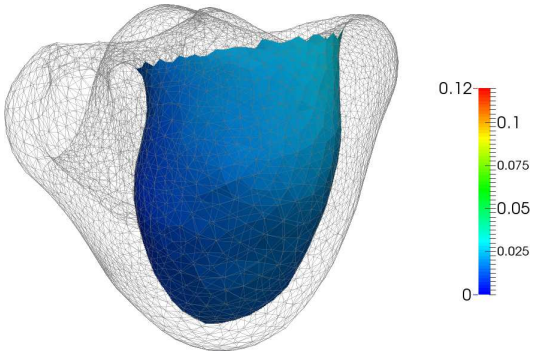

(b) Simulated depolarization times before optimization (s)

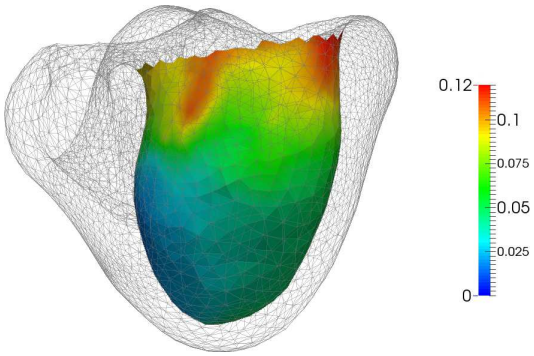

(c) Simulated depolarization times after optimization (s)

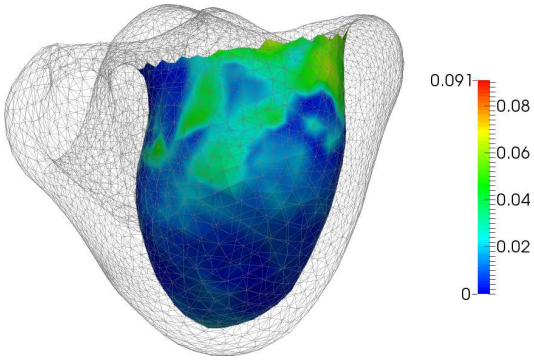

(d) Error map on depolarization time (s)

Figure 4.11: Evaluation of the personalized simulation: Patient 3

CHAPTER 5

Interactive Training System for Interventional Electrocardiology Procedure

Contents

Based on:

Talbot et al. (2014c): H. Talbot, F. Spadoni, C. Duriez, M. Sermesant, M. O'Neil, S. Cotin et H. Delingette. Interactive Training System for Interventional Electrocardiology Procedures. to be submitted, 2014c

Recent progress in cardiac catheterization and devices allowed to develop new therapies for severe cardiac diseases like arrhythmias and heart failure. The skills required for such interventions are still very challenging to learn, and typically acquired over several years. Virtual reality simulators can reduce this burden by allowing to practice such procedures without consequences on patients. In this paper, we propose the first training system dedicated to cardiac electrophysiology, including pacing and ablation procedures. Our framework involves a catheter navigation that faithfully reproduces issues intrinsic to intra-cardiac catheterization and an efficient GPU-based electrophysiological model. A multithreading approach is proposed to compute both real-time simulations (navigation and electrophysiology) asynchronously. With this method, we reach high computational performance that allows to account for user interactions in real-time. Based on a scenario of cardiac arrhythmia, we demonstrate the ability of the user-guided simulator to navigate inside vessels and cardiac cavities with a catheter and to reproduce an ablation procedure involving tasks: extra-cellular potential measurements, endocardial surface reconstruction, electrophysiology mapping, RF ablation, as well as electrical stimulation. This works is a step towards computerized medical learning curriculum.

In previous chapters, we developed a GPU electrophysiology simulation and we used its computational efficiency to propose a fast electrophysiology personalization based on UKF. It aimed at training cardiology interns and guiding cardiologists in an optimal choice of the ablation strategy using patient-specific simulations. This chapter focuses on the last step of our project, namely the design of a framework to rehearse an ablation procedure and interactively simulate patient-specific cardiac electrophysiology.

In the remainder, we consider arrythmias created by ventricular extrasystole, i.e. VT caused by ectopic foci. An ectopic focus is an abnormal self-excitable area (outside of the SA node) that initiates abnormal beats. Such pathologies can occur upon changes in the heart structure following a coronary artery disease or as chronic consequences of hypertension, diabetes or cardiomyopathy, as stated in Maron et al. (2006).

Considering an ectopic focus located inside the RV, the procedure first consists in inserting catheters in the femoral vein to benefit from a direct access to the RA. During this first stage, cardiologists can only rely on fluoroscopic imaging. Under this guidance, endovascular navigation not only requires a good knowledge of the vascular system but also a good hand-eye coordination. Once the RA is reached, the catheter must be skillfully handled in order to penetrate inside the RV through the tricuspid valve. An electro-

physiology mapping is then performed by exploring the endocardial surface with catheters to map the activation patterns. These patterns allow to locate the ectopic focus responsible for the arrhythmia. Each pathological region found by electrophysiology mapping will eventually be ablated, as illustrated in Fig. 5.1. RF ablation consists in heating the cardiac tissue next to the ectopic focus, that leads to cellular death, thus suppressing the related abnormal beats.

All these steps require a lot of experience in navigating through the cardiac anatomy. Till now, residents in cardiology train on patients by separately learning each step of the procedure under supervision of a senior cardiologist. In order to shorten the training period and to allow a virtual training on complex patient cases, we propose a training system for interventional cardiology based on the simulation of electrophysiology.

Specifications First, an endovascular catheterization must be provided in the training so that cardiology interns practice navigation in minimally invasive conditions. Then, our biophysical simulation has to reproduce as realistically as possible the cardiac electrophysiology. Thus, the trainee can interact with the simulated electrophysiology, i.e. analyzing the extra-cellular potentials, mapping activation times on the reconstructed endocardium and ablating the arrhythmia. Using our simulation framework for virtual training assumes to reach accurate and fast computations of both navigation and electrophysiology. Spatial and temporal discretizations must be sufficiently small to faithfully reproduce the effect of an ectopic focus, whereas computational efficiency is key to ensure interactivity while navigating inside the blood vessels or interacting with the cardiac electrophysiology (e.g. intracardiac measurements, RF ablation or electrical stimulation). To make this framework even more immersive, the simulation environment has to mimic

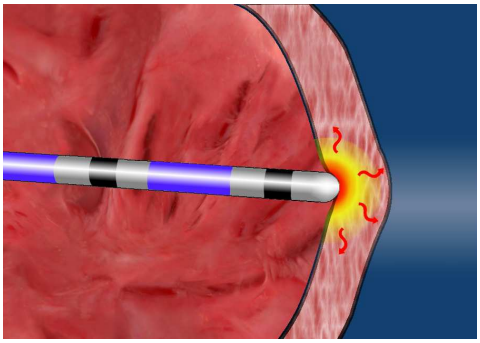

Figure 5.1: RF ablation: the catheter heats the endocardial surface to damage the tissues responsible for the pathology

Figure 5.2: Setup of our training system using the Mentice VIST device and inspired by the "cath lab"-like environment

the environment of the operating room.

Previous work Previous research projects already led to training simulators in cardiology as Dawson et al. (2000). The most recent simulator is proposed by Chiang et al. (2013) and focuses on intra-ventricular navigation. The contribution of this work consists in virtually reproducing the conditions for the slip and nonslip interaction of the catheter. Authors present a qualitative analysis of the catheterization training using experimental data on a porcine LV, as well as an user evaluation. Few training systems succeeded to be commercialized such as Cathi from Siemens Siemens (2006), VIST (Vascular Intervention Simulation Trainer) from Mentice Mentice (2012), Simantha from SimSuite Corporation (2013), CathLabVR from CAE HealthCare HealthCare (2013) and Angio Mentor from Simbionix Simbionix (2012). All these simulators are mostly focusing on the endovascular navigation including pre-recorded ECGs, but none of these simulators neither includes a biophysical modeling of the cardiac electrophysiology, nor models the interaction between a catheter and a cardiac electrophysiology.

Simulating the human cardiac electrophysiology is a wide field of research. However, only recent work Bartocci et al. (2011); Rapaka et al. (2012); Talbot et al. (2013a) investigate high performance computing applied to cardiac electrophysiology in order to achieve quasi real-time simulations. Therefore, coupling a simulation of endovascular navigation with a model of cardiac electrophysiology while keeping performances close to real-time is extremely challenging.

Proposed framework Here, we present a training system dedicated to interventional electrocardiology procedures that combines endovascular catheterization with a biophysical modeling of cardiac electrophysiology. The proposed endovascular navigation takes place inside a beating heart model using

a steerable model of catheter. A phenomenological model of cardiac electrophysiology based on a GPU implementation allows to reach a high level of interactivity. Using a multithreading approach, we couple cardiac electrophysiology and catheter navigation simulations, both running separately in real-time but at different time steps. This contribution enables the simulation to meet the requirements related to training systems in terms of computational efficiency and accuracy. With this framework, the user can visualize interactively bipolar potentials, reconstruct the endocardial surface while mapping activation times, perform RF ablation or electrical stimulation in real-time. Inspired by the setup of a catheterization laboratory (or cath lab, see Fig. 2.10), our framework reproduces fluoroscopic images, intra-cardiac ECG plots. As shown in Fig. 5.2, it is also interfaced with a tracking device Mentice (2012).

This chapter is written according to the structure of the training simulator displayed in Fig. 5.3. First, we focus on the catheter navigation in the scope of electrocardiology, i.e. with a moving environment. Second, the computational model chosen to simulate cardiac electrophysiology is presented. Third, we describe how the navigation and electrophysiology simulation are integrated and interfaced in our framework. Finally, a performance analysis and a clinical evaluation are conducted based on a synthetic case of ventricular extrasystole.

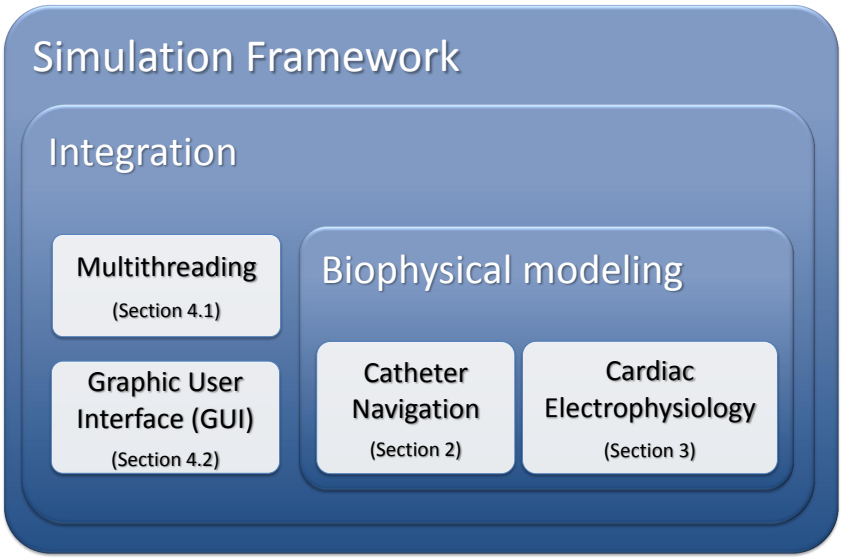

Figure 5.3: Overview of the structure of the chapter

5.1 Catheter Navigation in Cardiology

The simulator is developed using SOFA[8] Faure et al. (2012) and reproduces an intervention aiming at ablating an ectopic focus located in the RV. In this section, we first provide the background on the catheter navigation model. Then, we present a beating heart model extracted from cine MRI data and its coupling with the collision response process. The section ends with the presentation of our steerable catheter model.

5.1.1 Background on Catheter Navigation Models

The real-time simulation of the catheter behavior during endovascular procedures is particularly challenging and has been the central interest of several research work. Catheters are wire-like structures characterized by stiff and light materials, high tensile strength and low resistance to bending. In continuum mechanics, the behavior of such structures falls into the category of rods. The beam theory, built on Kirchhoff rods hypothesis, is widely used for FEM of such structures and is described in several publications, such as Przemieniecki (1985). This approach is completed by Cosserat brothers in Cosserat et al. (1909) who describe wire-like structures as a set of oriented micro-solids. Starting from these theoretical work, many variations and dedicated algorithms (referenced by Theetten in Theetten et al. (2008)) have been developed to simulate rod deformation.

Our work relies on the FEM introduced by Duriez et al. in Duriez et al. (2006) and further developed by Dequidt et al. in Dequidt et al. (2008), both in the context of coil embolization in neurology. This method is based on Kirchhoff rod theory, so that our catheter results in a serial set of beam elements, as it appears in Fig. 5.4. We choose this corotational approach since it handles geometric non-linearity due to large changes in the shape of the object. Defined in a Cartesian coordinate system, the contact resolution also results in the assembly of a block-tridiagonal matrix, efficient to solve. Other models exist for wire-like structures as the inextensible super-helices model proposed by Bertails et al. Bertails et al. (2006) or a linear representation of angular springs in Wang et al. Wang et al. (2007a). However, super-helices from Bertails involve a quadratic time complexity regarding the number of helical elements. In comparison, corotational beam approach offers a linear complexity. Based on non-physical angular springs, the representation chosen by Wang implies non-physical behavior.

The corotational model assumes that the deformations remain "small" in a local frame defined at the level of each element. In our scope of endovascular

[8]SOFA is an open source framework for interactive numerical simulations in medicine. More information about SOFA can be found at http://www.sofa-framework.org

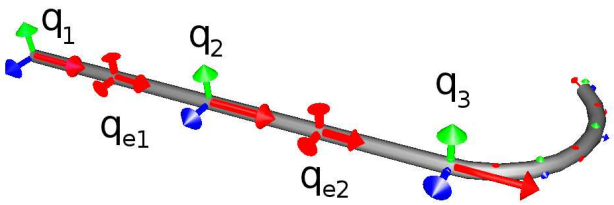

Figure 5.4: Catheter beam model in its curved rest shape: with the tricolor nodal frames; and the red frames matching the middle of each beam

navigation, the catheter undergoes large displacements but only small deformations, which meets the corotational assumption. One beam element is delimited by two nodes that have 6 degrees of freedom (DOF) each: 3 angular $\mathbf{q}_r$ and 3 spatial positions $\mathbf{q}_t$. The beam element includes a 12x12 symmetric stiffness matrix $\mathbf{K}_e$ that relates the nodal degrees of freedom of a beam element to the forces and torques applied to them. The final internal forces $\mathbf{f^i}$ generated by the deformation of the structure at one node i are:

$$\mathbf{f}^i = \sum_{e=i-1}^{i} \mathbf{R}_e(\mathbf{q})\ \mathbf{K}_e\ (\mathbf{R}_e(\mathbf{q})^T(\mathbf{q} - \mathbf{q}_e) - \mathbf{p}_{\text{rest}}) \tag{5.1}$$

where e is the index of the two beams connected to this i^{th} node. $\mathbf{q_{i-1}}$, $\mathbf{q_i}$ and $\mathbf{q_{i+1}}$ are the vectors of the 6 DOF position of the three nodes (respectively $i-1$, i, $i+1$) and belong to the two beams in the global frame (quaternions are used for rotations). In Fig. 5.4, tricolor frames depict these nodal frames. $\mathbf{q}_{ej}$ denotes the middle frame of the j^{th} beam (red frames) that is computed as an intermediate 6 DOF position between the two nodes of the beam. $\mathbf{p}_{\text{rest}}$ corresponds to the 6 DOF rest position of these nodes in the local frame. Rotation matrix $\mathbf{R}_e$ is used for the mapping of vectors defined in the local frame to the global frame. As the rotation is not the same for the two beams, matrices $\mathbf{R}_e$ cannot be factorized. It results that the formulation of the internal force is a non-linear function of the nodal positions. We also integrate a mass matrix to obtain a dynamic model and we use a backward Euler integration with a time step of $dt_N = 0.02$ s. This model has been validated experimentally in Dequidt et al. Dequidt et al. (2008) by studying the coil rest shape under deformation.

For the catheter navigation, the main challenge remains the collision response with the vessel or heart walls. Even with static vessels, quick changes of the catheter velocity and stick/slip transitions generate non-smooth dynamics of the catheter. The collision detection is performed using first a Bounding Volume Hierarchy (BVH) for the broad phase, and then computing local minimal distances, as introduced in Johnson et Willemsen (2004). The simulation model is based on Signorini's and Coulomb's laws that are solved using the

constraint-based process described in Duriez et al. (2005) and optimized for catheter navigation in Duriez et al. (2006). For every contact between the catheter and the vessel, we can build a mapping function $\mathbb{A}$ that links the relative positions in the contact space[9] to the motion space. For each contact, $\mathbb{A}$ includes three DOF: one normal component for the contact response and two tangential components characterizing the friction.

$$\boldsymbol{\delta}_\alpha = \mathbb{A}_\alpha(\mathbf{q}, t) - \mathbb{A}_\alpha(\mathbf{x}, t) \tag{5.2}$$

with $\boldsymbol{\delta}_\alpha$ the relative displacement between the catheter and the vessel walls. $\mathbb{A}_\alpha(\mathbf{q}, t)$ and $\mathbb{A}_\alpha(\mathbf{x}, t)$ are respectively the mapping function of the catheter and the vessel walls. Both depend on the contact α, the catheter position $\mathbf{q}$ and the wall position $\mathbf{x}$.

To obtain a kinematic relation between both contact and motion spaces, we use a linearization of Eq. 5.2 according to the position of the catheter nodes. Hence, for each contact, we build the Jacobian of the mapping function: $\mathbf{H}_\alpha = \frac{\partial \mathbb{A}_\alpha}{\partial \mathbf{q}}$

In the model, we consider that the motion of the vessel is not influenced by the collision response, so there is no need to compute the Jacobian with respect to the vessel node position. We end up with the formulation of the relative displacements in the contact space:

$$\boldsymbol{\delta} = \underbrace{\mathbb{A}_\alpha(\mathbf{q}^{\text{free}}) - \mathbb{A}_\alpha(\mathbf{x})}_{\boldsymbol{\delta}^{\text{free}}} + \mathbf{H} d\mathbf{q}^{\text{cor}} \tag{5.3}$$

with $\mathbf{q}^{\text{free}}$ being the *free* position of the catheter (i.e. position obtained when no contact force applies) and $d\mathbf{q}^{\text{cor}}$ being the unknown corrective motions due to collision response. This corrective motion is obtained by solving Eq. 5.3 based on the Signorini's law through a Linear Complementarity Problem (LCP), as presented in Duriez et al. (2006). A combination with the Coulomb's law leads to a NLCP (Non-linear complementarity problem) solved using a Gauss-Seidel algorithm (see Duriez et al. (2005) for details).

5.1.2 4D-Image Based Model of the Heart

In this section, we describe the generation of realistic cardiac motion through time series of images, also called 4D (3D + time) images of the heart. We then describe how this animated mesh is included within the collision pipeline in order to provide a faithful behavior of the catheter.

[9] The first dimension of the contact space is along the surface normal due to the frictionless response of the Signorini's law. The two other dimensions of the contact space are tangential to the surface according to the Coulomb's friction law.

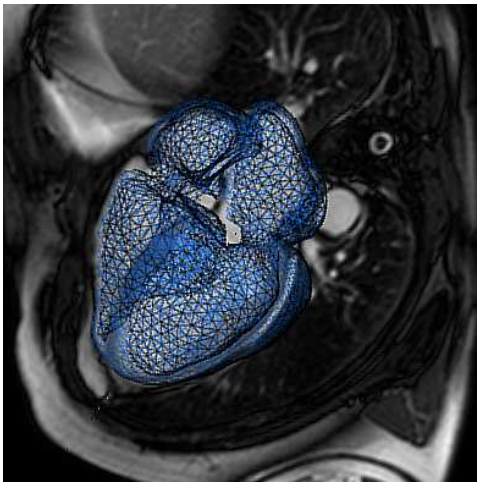

Figure 5.5: 3D SSFP slice with the static mesh resulting from segmentation (animation is then computed from the 4D cine MRI images)

Beating Heart Model

For a realistic navigation, we first need to recover the cardiovascular structure. Patient data were acquired in the framework of the European euHeart project[10] Talbot et al. (2013b). As shown in Fig. 5.5, 3D MRI are preoperatively obtained in order to reconstruct the patient-specific heart anatomy. Both atria and ventricles are labeled using a plugin tool implemented in GIMIAS[11]. The mask resulting from the segmented SSFP image is then meshed using the CGAL library[12]. Dedicated to endovascular navigation, a first mesh generation provides us the four heart chambers including 12,950 triangular elements. A second, static and finer mesh, only modeling the ventricles, is extracted for the electrophysiology computation including 30,807 linear tetrahedra.

However, the catheter navigation step also requires a mesh of the venous system leading to the heart, since navigation starts from the femoral vein. Regarding blood vessels, synthetic data of the inferior vena cava are extracted from the Zygote data set[13]. The resulting mesh for navigation fuses the generic model of vena cava with the patient-specific mesh of the heart (presented in Fig. 5.6).

After re-ordering the 60 cardiac phases (from passive filling to ventricular

[10]For more information about the euHeart project: www.euheart.eu

[11]GIMIAS is an open source framework providing image visualization, manipulation, and annotation. For more information: www.gimias.net

[12]CGAL is an open source software library that provides algorithms in computational geometry. For more information: www.cgal.org

[13]The Zygote data are a set of 3D anatomical models sold by the company Zygote Media Group. For more information: www.zygote.com

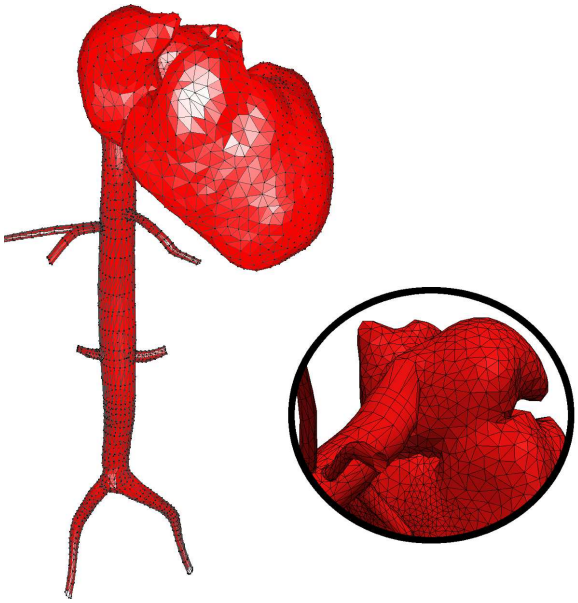

Figure 5.6: Resulting triangular mesh used for collision detection during cardiovascular navigation, and zoom on the connection between the inferior vena cava and the right atrium

isovolumetric relaxation), we estimate the cardiac motion from 4D cine MRI information using a Demon-based registration algorithm detailed in Mansi et al. (2011b). The estimated deformation field is resampled onto vertices of the navigation mesh, thus resulting in a realistic beating heart model, ready to be integrated in the simulation of catheter navigation. More important is that the resulting animated mesh stays coherent from a frame to another, i.e. the mesh topology is retained during the animation. The benefit of this coherent animated mesh will be detailed in the next sections.

Using Heart Motion in the Collision Pipeline

Accounting for the cardiac motion during catheter navigation is key to improve the realism of the simulation. Duriez et al. Duriez et al. (2006) and Dequidt et al. Dequidt et al. (2008) only consider static walls for their endovascular navigation since they concentrate on a neurological application. In the scope of cardiology, navigation becomes more complex due to contractions of the heart. Not only the heart is contracting but the surrounding vascular system is moving as well. An extension of the collision detection handling rigid moving cavities is therefore proposed. The catheterization procedure starts from an insertion point in the femoral vein, up to the heart chamber of interest (here, the RV).

The evaluation of the relative distance between the walls and the catheter is given in the Eq. 5.3. With a static environment, positions of the vessels

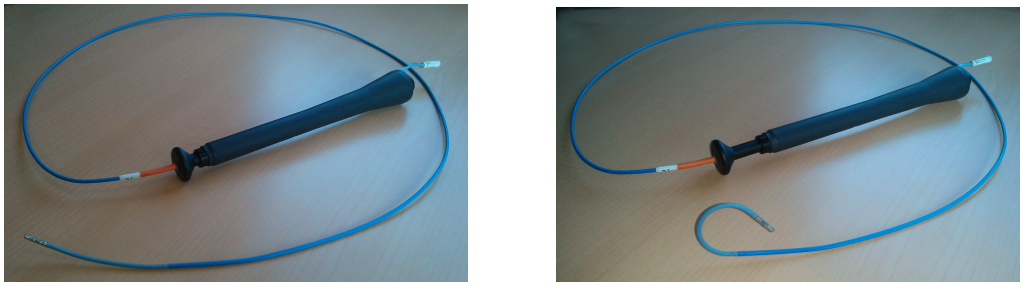

(a) Rest position (b) Bending position

Figure 5.7: Pneumatic steerable catheter used by cardiologists during electrophysiological procedures

$\mathbf{x}$ (corresponding to the mesh in Fig. 5.6) remain constant. To account for the cardiac motion, $\mathbf{x}$ therefore needs to be updated at every time step of the navigation. Subsequently, all bounding volume boxes used for collision detection are recomputed. Finally, the relative distance $\boldsymbol{\delta}$ can be re-estimated to compute the collision response, thus accounting for the vessel/heart motion.

In the previous section, the extraction of a coherent and animated mesh from medical images was detailed. Regarding the collision detection, BVH and proximity computations are preferred to distance maps since distance maps would need to be recomputed at each navigation step and previous positions of the catheter are translated into the new map. In our BVH-proximity approach, the conservation of the mesh topology ensures efficiency and more continuity (i.e. stability) since contact properties can be easily maintained from a frame to another. During the simulation, the computation time required for one collision detection step ranges from 3.99 ms to 6.54 ms. High level of performances can therefore be reached but the number of Frame Per Second (FPS) strongly depends on the number of contacts. Below 50 contacts real-time performance is ensured, whereas navigation is twice slower than real-time with more than 100 contacts. Details about the hardware configuration will be given in Section 5.4.

5.1.3 Navigation of the Steerable Catheter

To mimic the endovascular navigation, our framework is coupled with the VIST Mentice device Mentice (2012) (see Fig. 5.2), which measures the catheter insertion depth and rotation. This information is conveyed to the simulation and taken into account in real-time to drive the catheter. Providing buttons, pedals as well as joysticks, this device allows us to manage all possible interactions, e.g. moving the C-Arm used for the fluoroscopy.

Catheter navigation is a complex task even guided with fluoroscopic im-

ages. Reaching the heart cavities becomes even more challenging since the heart beats and the path to follow is not straightforward anymore. To go from the RA to the RV, the catheter must bend to face the tricuspid valve. To do so, the cardiologist uses a specific steerable catheter as the one presented in Fig. 5.7. Steerable catheter can use either pneumatic or mechanical actuators. Due to its bending feature, this catheter makes the access to the RV easier thanks to its curved shape.

In order to offer the user the same tools as in the operating room, our catheter model needs to be steerable as well. The catheter geometry is characterized by its rest shape, corresponding to the geometry without any force or constraint applied to the catheter. In our representation, the curvature of the rest shape is described by a curvature angle. The higher the angle, the more the catheter is bent. Set to zero, the catheter is straight. Dynamically controlled by the user through the Mentice device (see Fig. 5.8), the curvature can be changed to better navigate inside heart cavities.

5.2 Cardiac Electrophysiology

After detailing the navigation aspect, we now focus on the second crucial aspect of our simulation: the cardiac electrophysiology. In the context of a training simulator, the simulation of cardiac electrophysiology must be real-time while preserving accuracy to allow interactions with a realistic electrophysiology. First, the electrophysiology model is briefly introduced, then all interactions allowed with this electrophysiology are developed.

5.2.1 GPU Electrophysiology Model

Our work is based on the Mitchell Schaeffer (MS) model from Mitchell et Schaeffer (2003) since (*i*) it has only 5 parameters, (*ii*) each parameter has a

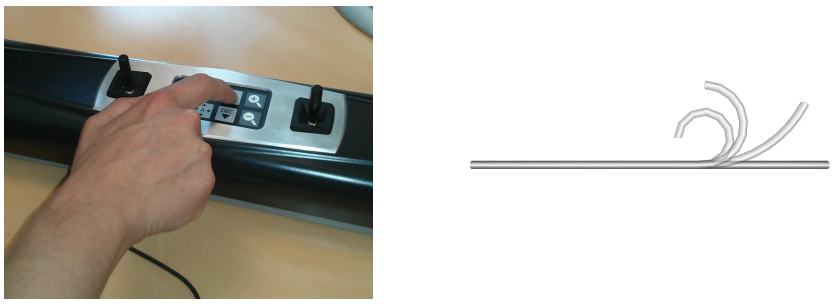

(a) Controlled by the device

(b) Bending motion in the simulation

Figure 5.8: Steerable catheter controlled in the simulation using the Mentice device

physiological meaning and (*iii*) it provides a better estimation of the action potential compared to other phenomenological models (as the Aliev-Panfilov model Aliev et Panfilov (1996)). The Sections 3.1 and 3.2 gave an exhaustive description of the model and its GPU implementation. The MS model is a two-variable model derived from the Fenton Karma model and its equations are given in the Eq. 3.1. Since it only captures the transmembrane potential, the MS model is a "mono-domain" model. Only "bi-domain" models can simulate both intra-cellular and extra-cellular potentials.

To ease the discussion, the normalized transmembrane potential is noted V_m, where $V_m = U_i - U_e$. Here, U_i denotes the intra-cellular potential, whereas U_e depicts the extra-cellular potential. The Eq. 3.1 becomes:

$$\begin{cases} \partial_t V_m = div(D\nabla V_m) + \dfrac{zV_m^2(1-V_m)}{\tau_{in}} - \dfrac{V_m}{\tau_{out}} + J_{stim} \\ \partial_t z = \begin{cases} \dfrac{(1-z)}{\tau_{open}} & \text{if} \quad V_m < V_{gate} \\ \dfrac{-z}{\tau_{close}} & \text{if} \quad V_m > V_{gate} \end{cases} \end{cases} \tag{5.4}$$

To increase computation efficiency, the electrical activity of the heart is only simulated for the ventricles. This consideration is acceptable since atria and ventricles are electrically isolated as mentioned previously. In our model, the stimulation is therefore induced by the Purkinje fibers. The implementation of Eq. 3.1 relies on the FEM. As explained in Subsection 5.1.2, the ventricular electrophysiology is computed on a static mesh using 30,807 linear tetrahedra. Moreover, the implementation of the weak form of reaction diffusion equations leads to zero Neumann boundary conditions, i.e. the electrical current is null in the orthogonal direction of the border. Based on our previous work Talbot et al. (2013a), the entire electrophysiology model is implemented on GPU. As explained in Subsection 3.1.3, the simulation time step is constrained by the coarseness of the mesh. In this simulation, we use a full explicit BDF integration scheme with a time step $dt_E = 10^{-4}$ s compatible with the stability conditions.

We run the electrophysiology simulation alone on a NVidia GTX 580 card. Using our implementation, one cardiac cycle (0.92 s) can be computed in less than 0.788 s, i.e. 1.15 times faster than real-time.

5.2.2 Interactive Model

In the scope of ventricular extrasystole, the most time consuming step of the RF ablation procedure consists in locating and ablating the pathological area: the ectopic focus. These areas include an excitable group of cells initiating a premature heart beat, called an ectopic beat. This premature beat has a

specific electrical pattern. Ectopic beats often appear sporadically and several steps are required to define the exact location of the pathological cells. Once catheters are positioned inside the heart cavities, the cardiologist needs to reconstruct the endocardial surface. Afterwards, the recording of the electrical activity is performed by acquiring a map of activation times. The pathological area can be localized since the ectopic focus corresponds to the region with the earliest activation time. Latest electrophysiology mapping systems are able to automatically detect an ectopic pattern from the analysis of the body surface ECG. As soon as an ectopic beat occurs, the system computes and maps the local activation time on the 3D reconstructed endocardial surface. By scanning the entire cavity, the ectopic focus can be found and then ablated. To end the operation, stimulation procedures check that a healthy sinus rhythm is restored.

The complexity of this procedure highlights the importance of interactions in our simulation. Based on an optimal GPU implementation, we propose new interactive features reproducing clinical gestures: extra-cellular potential measurements, reconstruction of the endocardial surface, mapping of ventricular activation times, RF ablation as well as electrical stimulation using the catheter. The interactions using the Mentice VIST device will now be detailed.

From Navigation to Electrophysiology Data

In order to keep a very high flexibility, our framework handles different meshes for electrophysiology and for navigation. However, the electrophysiology computation requires information about the catheter collision in order to allow interactions using the catheter. Measurement of the extra-cellular potential, electro-anatomical mapping, RF ablation and catheter stimulation are only possible when the catheter is in contact with the endocardium. The communication between electrophysiology and navigation is eased by the use of coherent meshes (i.e. unchanged topology), as explained in Section 5.1.2. The mapping developed between electrophysiology and navigation is now detailed.

While navigating inside the heart cavities, the collision detection returns each triangle τ_N of the navigation mesh colliding with a point of the catheter noted P. Using different meshes for navigation and electrophysiology requires to find the corresponding triangle τ_E of the electrophysiology mesh that includes the projection of P on the electrophysiology mesh. To start the search, we use a look-up table that associates the closest triangle of the electrophysiology mesh τ_E^{close} to each triangle of the navigation mesh. This look-up table is precomputed before the simulation starts. Moreover, the table remains valid during the simulation since the navigation mesh is coherent during the animation, as explained in Section 5.1.2. From this initial guess

τ_E^{close} given by the table, we look for τ_E regarding the barycentric coordinates of the projection of P. The desired triangle τ_E finally corresponds to the triangle having all barycentric coordinates positive. In this process, the use of the precomputed look-up table makes the catheter interaction more efficient.

Extra-Cellular Potential Measurement

During the procedure, cardiologists use catheters to interpret the electrical activity of the heart. These catheters can measure either unipolar or bipolar potentials, respectively measuring the extra-cellular potential U_e or a difference of extra-cellular potentials ΔU_e. Bipolar potentials are often preferred as they remove the far field potentials and provide sharper depolarizations. As detailed previously, the MS model only simulates the evolution of the transmembrane potential, noted V_m. Using the MS model, we do not directly simulate the extra-cellular potential measured with a catheter.

A realistic modeling of the displayed signals is key for our training simulator since cardiologists mainly rely on electrophysiological signals to understand the cardiac arrhythmia and guide the ablation procedure. To reach this level of realism, real unipolar signals acquired at CHU Bordeaux are mapped on the simulated transmembrane potentials. Each consecutive pair of electrodes (shown in the X-Ray view of Fig. 5.9) thus computes one bipolar signal obtained by the difference of the two unipolar signals. The resulting bipolar signals acquired *in silico* are presented in Fig. 5.10. In the simulation, four electrodes are defined along the catheter tip and three bipolar signals ("Cath1", "Cath2" and "Cath3") can be displayed. If one of the electrodes loses contact, noisy measurements are recorded. If both electrodes are in contact with the endocardium, the bipolar signal driven by our MS model is computed.

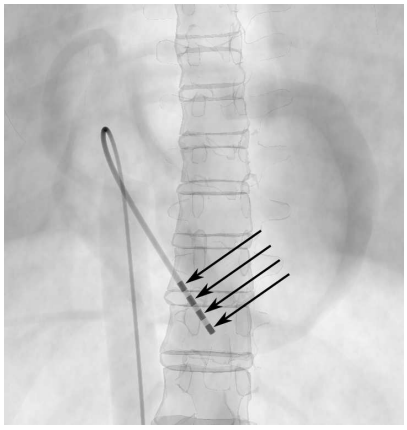

Figure 5.9: Fluoroscopic view of four electrodes (arrows) at the distal extremity of the catheter: each pair of electrodes measuring a bipolar extra-cellular potential

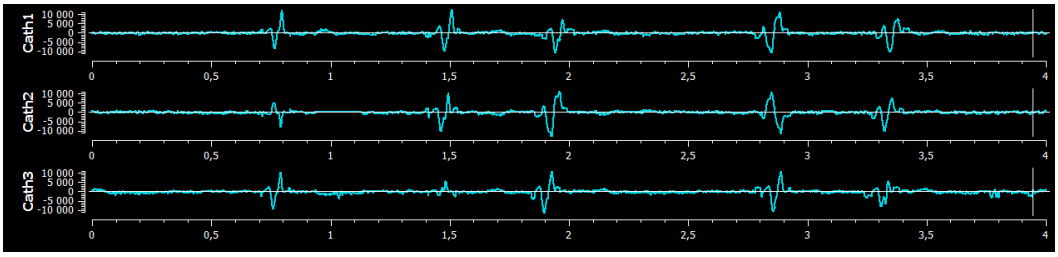

Figure 5.10: Three bipolar signals virtually measured by the four electrodes located along the catheter tip

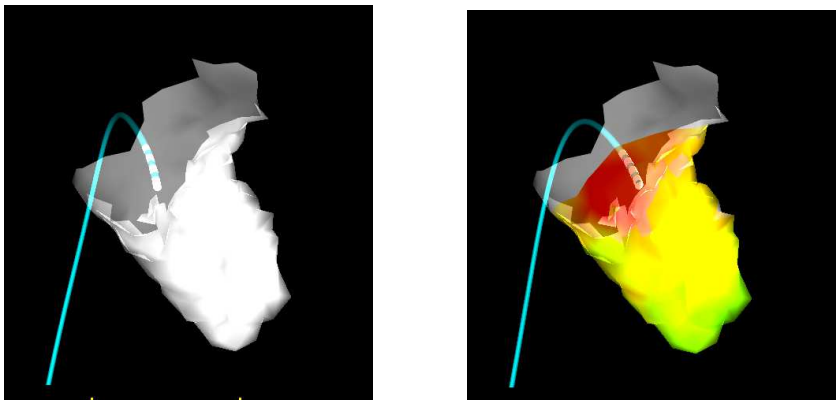

(a) Reconstruction of the 3D RV endocardium

(b) Extrasystolic activation times plotted on the reconstructed surface

Figure 5.11: Simulated electro-anatomic mapping done in two steps: endocardial surface reconstruction, then mapping of the extrasystolic activation times (red corresponds to short activation times)

Electro-Anatomical Mapping

Once inside the targeted cardiac chamber, the electro-anatomical mapping starts in order to localize the arrhythmic substrate, here an ectopic focus. Using a button on the Mentice device, the user can trigger the reconstruction of the endocardial surface. As with a real mapping system, the position of the catheter is tracked and the endocardium is partially reconstructed when the catheter touches the heart wall. In other words, as soon as a collision between the catheter and the endocardium occurs, the intersected triangles of the navigation mesh are displayed. Noise is added, so that the reconstructed surface looks realistic. The surface resulting from the virtual reconstruction is shown in Fig. 5.11(a).

After reconstructing the endocardium, the simulation allows to build a map of activation times based on the extra-cellular measurements. When an

ectopic stimulation starts while mapping, our framework computes local activation times, which are mapped on the endocardial surface. The activation times correspond to the elapsed time between the depolarization of the ectopic focus and the depolarization of the point currently in contact with the catheter. By measuring the extrasystolic activation times on the endocardium, the cardiology trainee can thus determine the exact location of the arrhythmia. The Fig. 5.11(b) captures this electro-anatomical mapping simulated during our virtual procedure.

RF Ablation

Once a target region has been identified, the cardiologist performs the RF ablation by heating the tissues using a RF (usually from 300 to 700 kHz) alternating current. This energy is delivered through an electrode in contact with the target tissue. When the temperature exceeds 60^oC, denaturing of proteins leads to a cellular death with coagulation necrosis. To be efficient, the temperature must nevertheless not exceed 100^oC. After ablation, cardiac cells lose their electrical conductivity. As a consequence, a successful procedure assumes that the regions originally responsible for the electrical disorder are well electrically isolated.

In our simulation, the ablation step is modeled by a progressive decrease of the electrical conductivity inside the tetrahedra. A zero conductivity is associated to dead cardiac cells. The effect of ablation gradually propagates from edge to edge through the myocardium. The longer the ablation duration, the larger the ablation area. Our training simulator also allows to set the desired power of ablation, thus making the ablation process faster or slower. During the simulation, the ablation is triggered by one of both pedals provided with the tracking device. The electrical conductivity of the tissue is consequently updated in real-time.

Stimulation

In the MS equation 3.1, the term $J_{stim}(t)$ is a stimulation current that can be added in the equation. This nodal term is used to apply any stimulation. Since we focus on ventricular extrasystole, there are three possible current sources.

- First, the heart has its own natural pacemaker called the SA node. These specific cardiac cells generate a regular electrical impulse (action potential) that propagates inside the atria. Since we only consider the ventricular electrophysiology, a regular stimulus is simulated starting from the Purkinje fibers at the apex of the heart. As in Mitchell et Schaeffer

(2003), we assume the stimulation current to be:

$$v_{stim} \approx \int J_{stim} dt \tag{5.5}$$

$$v_{stim} = 0.1 \tag{5.6}$$

- Second, the ectopic focus is the pathological area that causes random premature heart beats. This abnormal stimulation has also to be taken into account using an irregular current in the ectopic region. During the calculation, a stimulus current $J_{ectopic-stim}(t)$ is irregularly applied to the nodes characterizing the ectopic focus.

- Finally, the catheter can generate electrical impulses. This stimulation can be used by the cardiologist to assess the success of the ablation procedure. When the catheter touches the heart wall, an electrical current can be delivered in the region of contact. Moreover, the current value of this catheter stimulus $J_{cath-stim}(t)$ is interactively set by the user. As for the ablation, the stimulation is triggered by the user using the second pedal of the Mentice device. If no abnormal activity is detected during the stimulation process, the arrhythmic substrate is successfully ablated.

5.3 Integration of Electrophysiology and Navigation Simulations

Coupling the catheter navigation and the cardiac electrophysiology is far from being trivial. This first assumes to run both simulations together while keeping computation times close to real-time. Even if each separate simulation runs in real-time (depending on the number of contacts for the navigation), a serial execution of navigation and electrophysiology would result in low performances. Second, data have to be shared between navigation and electrophysiology to make user interactions possible. Therefore, both models have to communicate whereas they run at different time steps.

In this section, a powerful multithreading approach is presented that manages an asynchronous coupling while keeping good performances. Then, details are given about the graphical user interface, specifically designed to increase the sense of immersion.

5.3.1 Multithreading Approach

To integrate both electrophysiology and navigation simulations, we exploit the CPU parallelism and we choose a task scheduling architecture. This technique is an efficient way to scale the computation to all the CPU cores available.

The work load is broken down into tasks and a scheduler maps the tasks on each single CPU. A task is a block of code that executes a fraction of the work independently of other tasks and can run concurrently. The scheduler creates a thread for each processor, takes care of the thread synchronization and maps the task execution into threads, finding a new task to start when one ends.

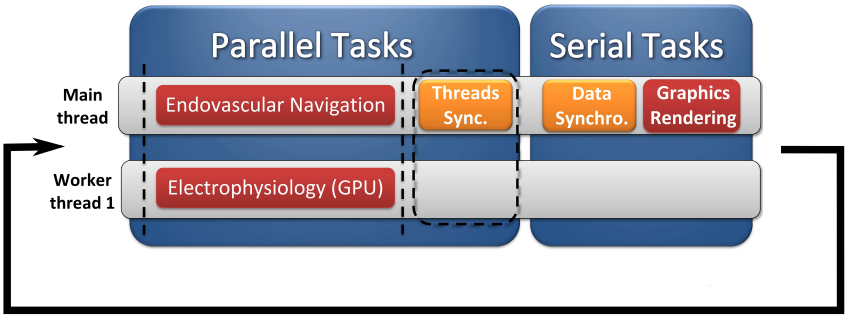

Figure 5.12: Multi-thread architecture: asynchronous navigation and electrophysiology threads, with a serial graphics rendering

Main Simulation Tasks Design

We know the electrophysiology computation is carried out onto GPU and it has been noticed that the graphics task is only a small fraction of the computation time. From these observations, we build our specific multithreading architecture. As detailed in Fig. 5.12, the main loop of our multithreading architecture is split into a parallel part executing concurrently the endovascular navigation and electrophysiology simulations and a serial part executing the graphics rendering.

Electrophysiology simulation requires a very low time step $dt_E \leq 1.5 \cdot 10^{-4}$ s for stability reasons, whereas navigation simulation is running with $dt_N \leq 0.02$ s. Based on our multithreading structure, several time integration loops of the electrophysiology are computed in the electrophysiology task whereas only one step is performed for the navigation. We assessed that 175 integration steps of electrophysiology for one step of navigation with a global time step $dt_N = 0.02$ s is the best compromise, i.e. for electrophysiology $dt_E = 1.15 \cdot 10^{-4}$ s. Our framework can then be depicted as an asynchronous simulation based on multithreading.

Communication between Tasks

The challenge in multithread design resides in handling the data synchronization between concurrent tasks. An optimal implementation assumes to find

the best trade-off between avoiding the increase of the serial execution time and avoiding the use of synchronization locks.

To avoid the use of synchronization locks, each main task has its own copy of the data. Data synchronization is performed before the graphics task, as it appears in Fig. 5.12. The choice of running the graphics task serially prevents us from a data synchronization between graphics and the other main tasks, thus reducing the amount of data exchange after each simulation loop.

During the step of data synchronization, few data are exchanged, as summed up in the Fig. 5.13. First, the tracking device must pass on information regarding the catheter motion to the navigation part, and update information about user interactions for the electrophysiology part. Secondly, the electrophysiology thread needs to recover all collision information, so that the user can interact with the patient electrophysiology using the catheter.

5.3.2 Graphical User Interface

To increase the realism of our training system, a graphical user interface (GUI) inspired of the setup inside the operating room (Fig. 2.10) is designed. Radiology interventions for RF ablation of cardiac arrhythmia are usually based on three main information sources:

- fluoroscopic images, sporadically acquired when the cardiologist needs it. These images are displayed on a dedicated screen.

- electrical signals, gathered on one unique screen. As mentioned previously, these signals are key in the procedure to detect the abnormal electrical activity of the ectopic focus.

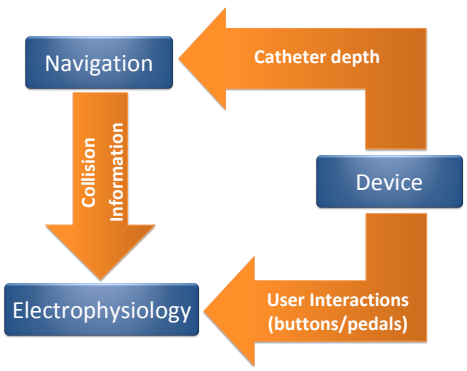

Figure 5.13: Exchange of data during data synchronization that is crucial for user interactions

- a 3D electro-anatomical map including the moving catheter. During real intracardiac interventions, the 3D endocardial surface is recontructed by tracking collisions between the catheter and the heart walls. The simulator described in Chiang et al. (2013) achieves a virtual reconstruction of the anatomical model of a ventricle. Our simulation reproduces not only the endocardium reconstruction but the mapping of activation times as well. From the analysis of this activation map, the ectopic focus can thus be located.

Our GUI mimics the layout of an operating room and incorporates the equivalent information available during the procedure. A global view of our GUI is shown in Fig. 5.14.

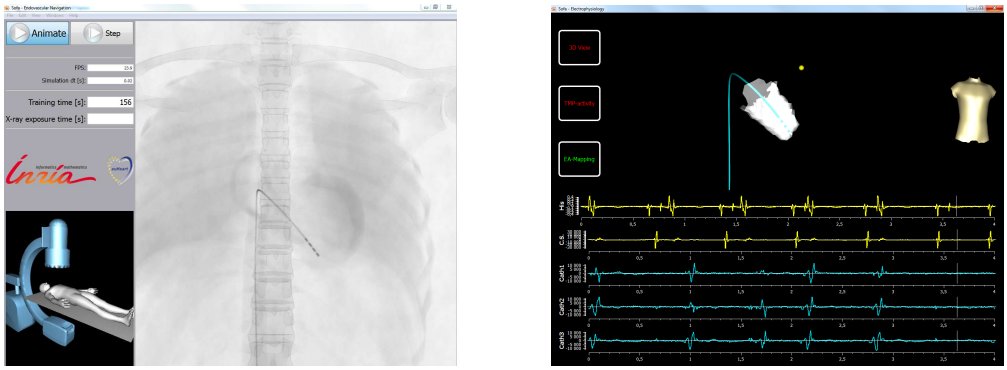

(a) Viewport n°1: fluoroscopic imaging

(b) Viewport n°2: electro-anatomical mapping and signals

Figure 5.14: View of the two screens used in our training simulator

- **Viewport n°1**: includes all the buttons controlling the simulation. This screen is also used to display the fluoroscopic images. The image orientation can be changed by moving the C-Arm, controlled by the tracking device. As shown in Fig. 5.16, joysticks can be used to move the C-Arm and translate the operation table. Additional information regarding the training is displayed, such as the total duration of the training session or the ablation duration.

- **Viewport n°2**: provides a 3D view for the electro-anatomic mapping and a set of intra-operative measurements. The 3D view includes the catheter moving inside the cardiovascular system. The reconstruction of the static endocardium and the mapping of activation times are displayed in this second viewport. Another visualization mode including the 3D dynamic cardiac electrophysiology is available, thus helping cardiology trainees to better understand the pathology at the organ scale.

With this mode, the GPU computation of the transmembrane potential (see subsection 5.2.1) that runs permanently becomes visible. This viewport also shows all the different recorded signals: signals at specific anatomical points (His bundle, coronary sinus) or the signals measured by the catheter.

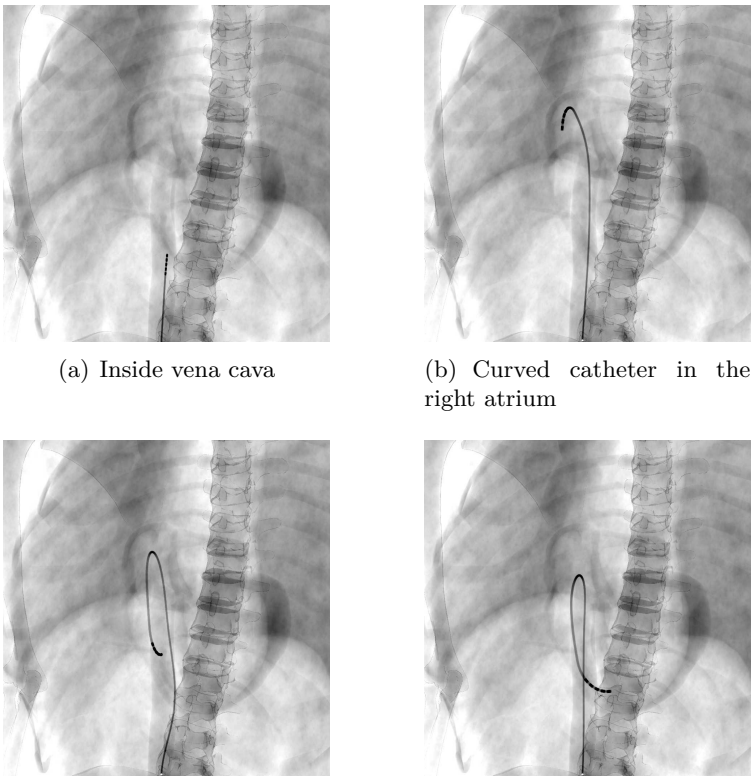

(a) Inside vena cava

(b) Curved catheter in the right atrium

(c) Inside the right ventricle

(d) Final position

Figure 5.15: Intra-cardiac catheterization

5.4 Results

5.4.1 Simulation Scenario

The designed training involves a virtual patient suffering from a cardiac arrhythmia caused by ectopic focus. This scenario assesses the ability of our simulator to reproduce a complete ablation procedure and to account for user interactions. As detailed previously, the ablation procedure for ectopic focus can be divided into three parts: catheter navigation, localization of the diseased region and ablation. Each step will now be presented and illustrated.

Navigation First, the user has to navigate using the catheter from femoral vein to the RV where the ectopic focus is located. After pushing up the catheter along the vena cava (see Fig. 5.15(a)), the catheter enters the heart. However, the RV is not straightforward to reach from the vena cava. To manage this, cardiologists usually use a bending catheter in order to orientate its tip towards the tricuspid valve and thus enter the RV easily. During the virtual procedure, the user faces the same issue and needs to bend the catheter to face the RV (see Fig. 5.15(b)). As in operation, it can be experimentally noticed that bending the catheter makes the RA-to-RV navigation easier in the simulation. Finally, the RV can be accessed by further inserting the catheter, as described in Fig. 5.15(c) and Fig. 5.15(d). This framework therefore includes a faithful catheter navigation step that strongly matches the ablation procedure.

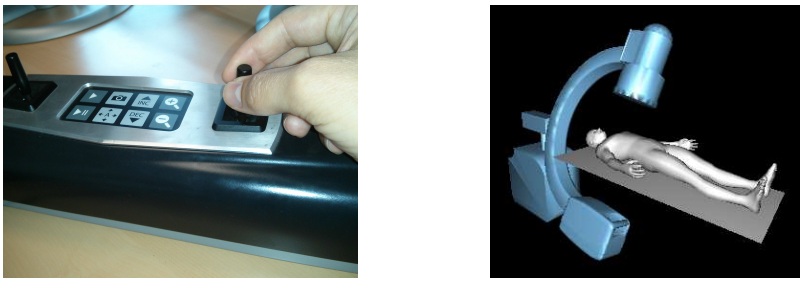

(a) Joystick controlling the C-Arm

(b) C-Arm visualization

Figure 5.16: C-Arm controlled using the hardware device

Localization Once inside the RV, the ectopic focus needs to be localized. This diseased area generates irregular extrasystolic stimuli. A capture of ectopic beats occurring during the simulation is shown in Fig. 5.17. In case of a ventricular extrasystole, the ectopic pattern is characterized by an early depolarization of the ventricle (visible on the catheter bipolar measurements). To start the localization, the endocardium must first be reconstructed. The user must slide the catheter against the heart wall to reconstruct a 3D surface (see Fig. 5.11(a)). Using an electrophysiology mapping, it is possible to locate the ectopic focus by studying the activation pattern produced by an extrasystolic beat. The pathological area can be found by iteratively measuring activation times on the endocardial surface. The ectopic focus should be the region with the shortest activation time. After acquisition of extrasystolic activation times on the endocardium, the Fig. 5.11(b) reveals the ectopic focus in the red area.

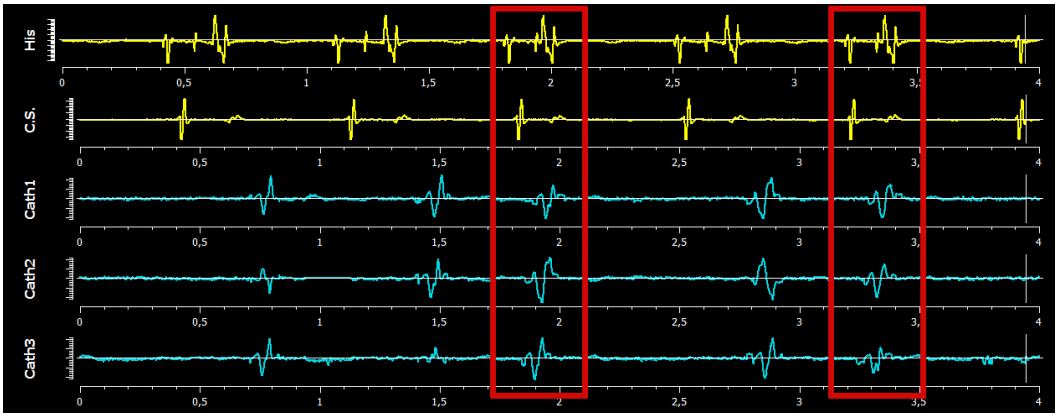

(a) Ectopic beats (red rectangles)

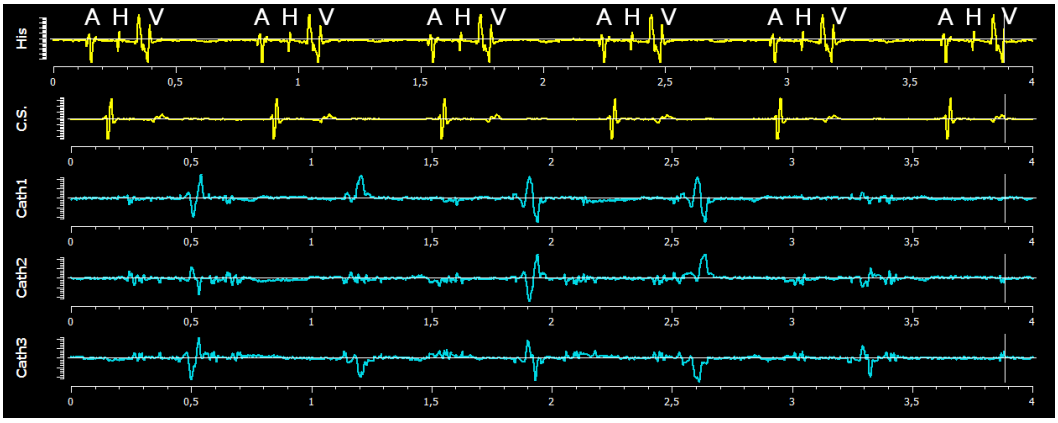

(b) Sinus rhythm after ablation of the ectopic focus: with regular atrial (A), His bundle (H) and ventricular (V) activations

Figure 5.17: Signals available in the simulation: with His bundle and coronary sinus measurements in yellow; and the three bipolar signals from the catheter

Ablation As soon as the ectopic region is localized, the user can proceed to its RF ablation. While ensuring contact between the catheter and the endocardium, the user can deliver the alternating current by pressing the left pedal. The scar resulting from the ablation is shown in Fig. 5.18.

The success of the ablation resides in isolating the complete region responsible for the ectopic beats. Therefore, abnormality in the cardiac rhythm should not be observed anymore and a regular sinus rhythm should remain, as it appears in Fig. 5.17(b). To assess the ablation, the user can finally deliver electrical impulses at different frequencies using the catheter. If no ischemic activity is detected, the entire region responsible for the ectopic beats is ablated and the operation is a success. However, if abnormal beats appear again, the ectopic focus is only partially ablated and the procedure has to be completed.

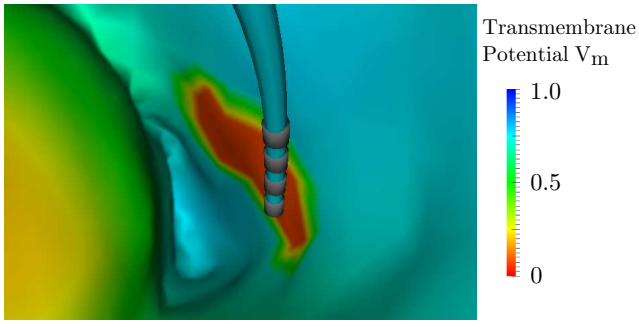

Figure 5.18: Internal view of the RV: colors correspond to the transmembrane potential; the red area underwent ablation

5.4.2 Performances

Exploiting the power of both multithreading and GPU computing, we achieve a fully interactive simulation. Our simulation runs on a computer including an Intel Core i7 CPU and an NVidia GTX 580 GPU. The performance results are given in Table 5.1 regarding the different steps during the procedure. In this table, real-time ratio stands for the ratio of elapsed time over computation time. When the simulation is faster than real-time (ratio $>$ 1), the computation can be slowed down to retain real-time. From Table 5.1, we first realize that the computational efficiency is strongly related to the number of contacts, i.e. to the navigation part. At the beginning of the procedure, only few contacts are detected whereas, once inside the heart, the catheter leans against the endocardium, thus decreasing the performance. This reveals that the navigation part tends to limit the overall performance when many contacts (over 50) are detected. 50 contacts implies 150 constraints which is substantial regarding the number of beams in our model (40 beams).

Table 5.1 also shows that our training system runs between 1.1 and 2.3 times slower than real-time. Our hybrid architecture proves to be efficient enough so that the entire simulation remains interactive. All possible interactions were introduced in Section 5.2.2 and illustrated in Section 5.4.1. Another crucial feature regarding our scope is that these interactions do not affect the performances. As a consequence, this training simulator for cardiac RF ablation procedure already offers close to real-time performances and a high level of interactivity.

5.4.3 Clinical Evaluation

An evaluation of our training simulation has been conducted in the cardiology department led by Dr. M. O'Neill belonging to the Guy's and St Thomas' National Health Service. At this occasion, seven electrophysiologists with

			Navigation only		Training Simulator	
Position	**Number of contacts**		**FPS**	**Real-time ratio**	**FPS**	**Real-time ratio**
	Mean	**[min-max]**				
Start	0	[0 - 0]	70.3	1.41	44.0	0.88
Vena cava (see Fig. 5.15(a))	2	[2 - 2]	67.3	1.35	43.8	0.87
Entrance of atrium	5	[2 - 14]	62.3	1.25	31.6	0.63
Loop (see Fig. 5.15(b))	110	[98 - 125]	26.4	0.53	21.5	0.43
Final (see Fig. 5.15(d))	50	[41 - 65]	45.9	0.92	23.6	0.47

Table 5.1: Performance results of the navigation simulation separately, and for our whole training framework (using for both a time step $dt = 0.02$ ms)

different level of experience practiced our virtual scenario of RF ablation in case of an ectopic focus. In the group, 4 participants were novice (less than three years of learning with almost no clinical practice) and 3 were experts (more than 10 years of clinical experience). After performing this virtual surgery, cardiologists filled a form in which each feature of the simulator has been evaluated using grades (see Table 5.2).

Grades		
Fail	=	0.0
Not satisfactory, to improve	=	1.0
Good	=	2.0
Very Good	=	3.0

Table 5.2: Possible grades to assess a given feature

This clinical evaluation provides a quantitative assessment of our framework. The different feedbacks are gathered in Table 5.3.

	Mean Grade
Procedure Evaluation	
Able to navigate through the venous system with the catheter	2.25
Able to bend the catheter and reach the RV	1.75
Able to reconstruct the RV endocardial surface	2.67
Able to map the activation times on the surface	2.30
Pathology can be characterized based on electrical measurements	2.30
Able to locate the ectopic focus using the intra-operative electrical measurements	2.10
Ablation can be performed	2.10
Able to ablate the ectopic focus	2.10
Realism of the Simulation	
Heart Motion	2.33
Fluoroscopic imaging	2.50
Catheter navigation	2.00
Electrophysiological signals	2.25
3D Mapping Simulation	2.50
Ablation procedure	2.33
Sensitive feedback	1.75
Global Experience	2.50
Interactivity of the Simulation	2.67
Immersive Experience	2.50

Table 5.3: Results of the clinical survey assessing our simulator

From this survey, it appears that the worst features of the simulation are: (i) reaching the RV from the RA by bending the catheter and (ii) the sensitive feedback. Some clinicians faced an issue while looping in the RA due to the length of our bending extremity. The shape of the steerable catheter has been subsequently fixed. Second, electrophysiologists pointed out a lack of force feedback using the catheter, especially when the catheter hits the heart walls. Till now, no force feedback has been implemented in our simulation and this remains a future work. Clinicians also pointed out that a surface ECG is usually used as reference in such operations. All improvements requested by the electrophysiologists are further discussed in the future work of this thesis.

Features obtaining the best grade are the 3D reconstruction of the endocardium and the global level of interactivity in the simulation. These positive appraisals attest to the good level of realism creating an immersive experience and to the global computational efficiency. Moreover, the overall grade given to this virtual experience amounts to 2.50, which is very encouraging. This clinical evaluation presents our framework as a promising tool for virtual training in cardiology.

5.5 Conclusion

In this last chapter, we present the first training system coupling a realistic catheter navigation with a fast cardiac electrophysiology model. We believe that this fully interactive framework is an important contribution towards training in cardiology based on medical simulators. The first main contribution of this work is to propose an interactive catheter navigation inside a moving venous system and a beating heart. The virtual catheterization reproduces navigation issues that can be solved using a bending catheter. Second, we present a real-time GPU electrophysiology model allowing interactions during the simulation such as extra-cellular potential measurement, endocardial surface reconstruction, electrophysiology mapping, RF ablation, and electrical stimulation. Finally, both navigation and electrophysiology simulations are integrated within a flexible framework. An innovative management of the computational units based on multithreading offers performances close to real-time. Even inside the contracting RV, the simulation remains only twice slower than real-time. Using a GUI that mimics the interventional environment, cardiologists could therefore train and gain experience on virtual ablation scenario close to their future operating room.

The clinical study conducted at the St Thomas Hospital highlights the satisfactory aspects and the weaknesses of our simulation. This framework is a first step towards realistic and efficient virtual training systems in cardiology.

CHAPTER 6

Conclusion and Perspectives

Contents

In this thesis, we presented an efficient cardiac electrophysiology simulation and we built a personalization framework based on the proposed electrophysiology model. We then constructed a training framework dedicated to junior electrophysiologists for cardiac arrhythmia ablation. An evaluation conducted by clinicians demonstrated the performances and the realism of this scenario. In this chapter, we summarise the contributions of each chapter and discuss the perspectives of the work presented in this thesis.

6.1 Conclusion

Real-Time Cardiac Electrophysiology Computation

Aiming at developing a training framework, this work first focused on a real-time electrophysiology simulation. After selecting an appropriate phenomenological model, a GPU implementation of the FEM model was proposed including 65,500 tetrahedra. The resulting computation reached good performances close to real-time, thus offering many possible applications. This GPU implementation was then coupled with a mechanical model of the heart. We demonstrated that the simulation reproduced the characteristic electrophysiology and mechanical contraction of a LBBB patient. This work was published in Talbot et al. (2013a).

Personalization of Electrophysiology Model

This work extended the efficient model of electrophysiology to a personalization tool. First, an exhaustive state of the art on optimization methods was provided to guide our choice. The data acquisition was presented and our personalization based on data assimilation was studied. We demonstrated the efficiency and the accuracy of our method using three patients suffering from VT. Personalised MS model was sufficient to generate re-entrant VT, based on the observed spatial heterogeneities. Running in about 20 minutes, this promising personalization process proved to be compatible with clinical constraints. We also observed a high sensitivity to the assimilation parameters. This work will be submitted as Talbot et al. (2014a).

Interactive Training System for Interventional Electrocardiology Procedure

We proposed a training scenario simulating an ablation procedure in the context of a RV ectopic focus. Combining an endovascular navigation and an interactive cardiac electrophysiology using a multithreaded architecture, we obtained performances close to real-time. The high level of interactivity also allowed to virtually reproduce all possible clinical gestures, namely electrical catheter measurements, electro-anatomical mapping, electrical stimulation and RF ablation. The development of an interface based on catheterization laboratory increased the realism of the training prototype. The quantitative assessment by cardiologists showed the ability of the framework to allow interactive gestures and to faithfully model the electrophysiology of arrhythmic patients. This interactive training system was a first contribution towards virtual curriculum in electrophysiology. This work was reported in euHeart project deliverable Talbot et al. (2011, 2013b) and will be submitted as Talbot et al. (2014c).

6.2 Perspectives

6.2.1 Training System for cardiac RF Ablation

The training system constructed in this thesis reached satisfactory performances and clinicians provided encouraging feedbacks. Further to the evaluation process, electrophysiologists made two main remarks to improve the simulation. First, the absence of force feedback was pointed out. Using our navigation model, a collision response could be implemented to reproduce the effect of friction and collisions against the endocardium. As presented in Chapter 5, the catheter navigation relies on the Signorini's law combined with the Coulomb's law and results in a non-linear complementary problem. The

solution of the system gives us the corrective motion of the catheter which is directly related to force applied on the catheter. A realistic force feedback can thus be defined.

Second, most of the clinicians asked for a surface ECG, which could help the understanding of the arrhythmia. To complete our training prototype, further research must therefore be conducted to extract the ECG information from our electrophysiology model. Both aspects (force feedback and ECG simulation) will be addressed in near future.

Another perspective regarding this training system consists in transferring this technology to a company. This project will require to meet different cardiologists to discuss and clearly establish how could this framework be concretely used. Moreover, a transfer of technology would be a great satisfaction after years of research.

6.2.2 Planification Tool for Ablation Procedures

The work presented in Chapter 4 gave promising results in terms of efficiency. However, further developments in the algorithm can be investigated. To start with, regions can be updated during the simulation. Regional conductivities can also be smoothed from a zone to another in order to avoid parameter discontinuities. Moreover, two specific regions for the personalization of both His bundle and epicardium can be studied. Finally, the personalization framework can be applied on new patient cases with various type of arrhythmia to assess its robustness.

In the long-term, the personalized framework can be coupled with our training framework. A virtual experience on different arrhythmic patients can significantly enlarge the application of our training system. Not only could cardiology interns better understand the mechanism of arrhythmias, but senior cardiologists could use this framework to plan a future ablation procedure. In case of complex arrhythmia, electrophysiology experts would be able to test different ablation strategies *in silico* before entering in the operation room.

6.2.3 Cryoablation in Cardiology

We saw that cryoablation is a technique for tumor ablation of which the field of application is expanding. First used in urology and dermatology, the ablation method expanded and progressed thereafter. Cryotherapy is now an ubiquitous practice for cancer ablation: liver and pancreas tumor, breast cancer, or lymph node metastases among others can be treated using this technique. Recently, cryotherapy was applied to cardiology for arrhythmia treatments (see Dubuc et al. (2001)). Our work on electrophysiology and cryoablation can therefore be of interest. In the coming years, simulation of

cryoablation procedure can bring new tools especially for surgical planning and guidance purposes.

Appendix A

This work around the cryoablation was a project between the IHU Strasbourg and NHC Strasbourg. It has been carried out on the fringe of our research around cardiac electrophysiology. Nowadays, cryoablation is a widely used technology for tumor treatments. After discussion with experts in interventional radiology, it appeared that clinicians lack efficient and accurate guiding tools for the needle insertion. In this work, we propose a proof of concept regarding the simulation of cryoablation. This appendix is based on:

Talbot et al. (2014b): H. Talbot, M. Lekkal, R. Béssard-Duparc et S. Cotin. Interactive Planning of Cryotherapy Using Physically-Based Simulation. In MMVR 21 - Medicine Meets Virtual Reality - 2014, Manhattan Beach, California, États-Unis, 2014b

Cryosurgery (also called cryoablation or cryotherapy) is a clinical technique that has been introduced to treat prostate cancers early in the 1960s. It is based on the Thompson-Joule phenomenon, and works by decompressing very rapidly a gas (generally argon) through a needle-like probe. The cryoprobes are small, hollow, cylindrical devices of about 1.5 mm in diameter, and may be put into the tumor during laparoscopic surgery or percutaneously under image guidance as shown in Fig. A.1(a). A ball of ice crystals forms around the probe, thus immediately leading to cellular death of the surrounding tissues. Cryosurgery often involves a cycle of treatments in which the tumor is frozen, allowed to thaw, and then refrozen. The procedure will continue until all tumor tissue is frozen to a temperature of approximately 233K to 248K. This technique has been applied to treat many kinds of tumors, such as breast cancer, primary or metastatic liver neoplasms, renal, lung, pancreas, and prostate cancer. As mentioned in Chapter 4, cryoablation was recently introduced in the field of cardiology. For now, this technique is no substitute for RF ablation but it reveals a high potential for some arrhythmic substrates located in the perinodal area, Koch's triangle, pulmonary veins, or coronary sinus. This practice of catheter cryoablation for cardiac arrhythmias is discussed in Chan (2013).

In tumor ablation, the volume of the ice ball must be slightly larger than the volume of tumor to ensure the effectiveness of cryosurgery but minimize freezing damage to nearby healthy tissue. Knowing that there are about 6 different types of cryoprobes each producing a different ice ball size and shape, the size and shape of the ice ball produced by a single probe can vary significantly.

To guaranty an optimal tumor ablation, it is quite obvious that a very careful planning must be performed to define the best position for each probe as well as the type of probe. This planning is currently done qualitatively, based on experience, and can take several hours, with a result that is often different from the expected one. To solve this important limitation of cryotherapy, a few planning systems have been proposed in the literature. Currently, commercial systems are nearly non existent, and emerging tools are limited to a visualization of the isotherms obtained for each probe in ideal conditions (usually in a gel). They do not account for any influence of the soft tissue properties, the presence of blood vessels, or the combined effect of multiple probes. As a consequence, large safety margins over 5 mm need to be planned, as detailed in Georgiades et al. (2012); Young et al. (2010). More advanced approaches have been proposed recently in the literature. They essentially rely on the same equation describing the heat diffusion through soft tissues Blezek et al. (2010); Chen et al. (2009); Magalov et al. (2008); Zhang et al. (2005). These different works all focus on the computation of the cryoablation process

(not the planning itself), they propose some computation time optimizations, and offer limited validation. But the main criticism of all these different approaches is that they do not address some key requirements for being used in clinical routine. For instance, the computation times reported by Chen *et al.* Chen et al. (2009) is of about 2 days of computation for a freezing cycle of 10 minutes, and all of the proposed methods require a significant pre-processing of the medical images to segment, label and mesh the different tissue types.

In this appendix, we introduce three main contributions, all aimed at bringing cryotherapy simulation closer to requirements for clinical use. First, our framework (see Fig. A.1(b)) proposes an innovative simulation directly based on medical images, sparing any segmentation, reconstruction and meshing step. Second, our multi-resolution and GPU-based approach significantly reduces computation times compared to the state-of-the-art, making it compatible with a clinical use, which has never been done till now. Third, our physics-based simulation can predict the ice ball produced by multiple cryoprobes. Accounting for this synergistic effect is key for cryotherapy planning as detailed in Young (2011). An evaluation using clinical data finally supports our contribution as a significant step forward in the context of cryotherapy.

Methods

Bioheat Equation: the Pennes' Model

The two main models estimating the heat transfer in perfused tissue are the Pennes' model Pennes (1948) and the Wulff's model Wulff (1974), both based on the enthalpy method. Front tracking methods can also be used to model heat propagation. However, these tracking methods use non-physiological pa-

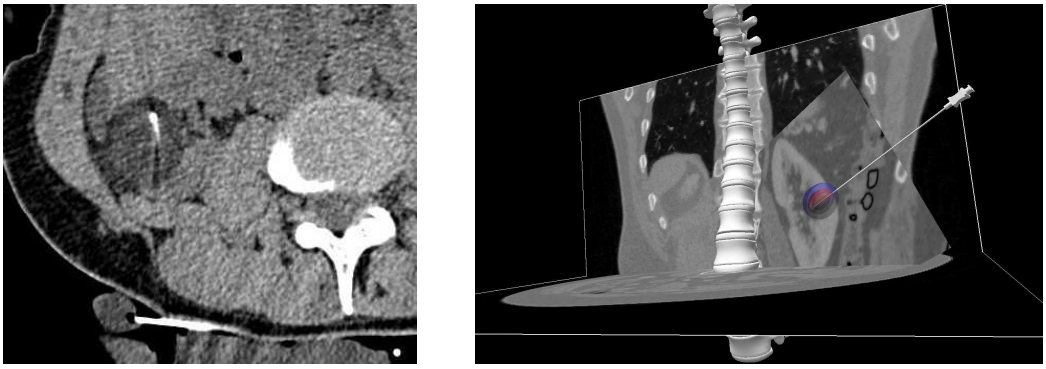

(a) CT image of a kidney treated with two Ice-Sphere cryoprobes

(b) Screenshot of our framework mixing patient data and cryosurgery simulation

Figure A.1: Context of our cryoablation framework

rameters. In this work, we rely on the Pennes' model that assumes a constant blood temperature. The heat transfer can then be described by the following equation:

$$\rho_t c_t \frac{\partial T}{\partial t} = div(k_t \nabla T) + W_b c_b \ (T_a - T) + Q_m \tag{A.1}$$

where T is the temperature of the living tissue, ρ_t, k_t and c_t and are, respectively, the density, the thermal conductivity and specific heat of the tissue. W_b is the perfusion rate, c_b the specific heat of the blood and T_a is the temperature of the arterial blood. Q_m is the metabolic heat generation.

In this work, our simulation of thermal diffusion is first evaluated with experimental tests in water and then using patient-specific data (see Fig. A.1(a)). In both cases, the parameters used in our simulation are the ones presented in Zhang et al. (2005). For the experimental tests in water, some parameters need however to be changed: the ambient temperature is set to 23°C and the metabolic heat, as well as the blood perfusion rate, are set to zero.

As presented in Young et al. (2011), usual procedures for cryosurgery consists of three steps: double ten-minute freeze cycles separated by a 5-minute thaw. However, the second freeze cycle only enables the clinicians to make sure that cells below −20°C die, and do not increase the ice ball dimension. Our simulation consequently focuses on the first freeze cycle and the 0°C isotherm will be compared with the segmented ice ball.

Numerical Approach

Spatial Discretization Our biophysical model is implemented using the FEM. From medical images, we define a regular grid of adjustable resolution surrounding the region of interest, namely the tumor. The computation grid is then decomposed into regular tetrahedra to reduce numerical errors.

Time Integration Regarding the time integration, a full explicit scheme with an explicit-BDF solver is chosen. Since it is an explicit formulation, we get a diagonal system to solve ($\mathbf{D}T = b$), that can be solved easily, without linear solver. Our integration scheme can be written as follows:

$$T_{t+\Delta t} = \frac{1}{3}\left(4 \cdot T_t - T_{t-\Delta t}\right) + \frac{2\ \Delta t}{3} \cdot (\mathbf{D}^{-1} b) \tag{A.2}$$

Tissue Domain Boundary Conditions Using a weak formulation for the integration of diffusion term, it can be shown that natural boundary conditions, described in Eq. A.3, appear on the surface (triangles are denoted t in the expression). It has been implemented so that our model verifies a zero Neumann boundary condition: $\nabla T = 0$.

$$\sum_t \frac{k_t A}{3} (\nabla T \cdot \mathbf{n}) \tag{A.3}$$

Cryoprobe Boundary Conditions Our simulation also needs to account for the freezing effect due to the cryoprobe. Needles used in cryotherapy have very thin diameter: usually 17 gauges, i.e. 1.47 mm. A second boundary condition has to be introduced to model this negative heat source, as detailed in Eq. A.4.

$$-k \frac{\partial T}{\partial n}\bigg|_{surf} = h_\infty \, (T_\infty - T) \tag{A.4}$$

where h_∞ is the needle convection coefficient, T_∞ is the free-stream temperature of the probe, and subscript *surf* denotes triangles circumscribing the needle surface.

GPU Optimization Thin dimensions of the cryoprobes implies strong limitations on the grid. To capture the effect of the cryoprobes, length of tetrahedra edges surrounding the needle must be smaller than $dx < 1.47\ mm$. Using larger elements would numerically increase the freezing effect and would distort the resulting ice ball, whereas using very fine elements implies huge computation costs. Both cases seem incompatible with accuracy and efficiency requirements for clinical use. We decide to use fine grids in order to preserve accuracy, but computational efficiency therefore becomes a major issue for our cryosurgery simulation.

GPU implementation is proposed as an appropriate solution to these computation cost problem. GPU computing consists in using all the multiprocessors of the graphics processing unit in order to carry out highly parallel tasks. Considering the grid size required for our simulation and the low complexity of the Pennes' equation, using this technique seems meaningful. The complexity of GPU computing results in optimally distributing these independent tasks (threads) and minimizing the memory access latency. In our work, the GPU version of our algorithm has been developed using CUDA toolkit dedicated to NVidia's GPUs. In the Pennes' equation, strong neighboring dependencies of the diffusion term $div(k_t \cdot \nabla T)$ make its implementation on GPU very challenging. In a parallel computation, this algorithm can lead to writing conflicts: two threads solving two adjacent edges could write on the

same point simultaneously. Using recent CUDA versions enables to overcome this issue. However, a more powerful implementation has been recently proposed in Allard et al. (2011). Originally designed for deformable finite element equations, we propose a new application of this algorithm for simulating the cryotherapy procedure. Moreover, the GPU implementation of the additional terms (metabolic and arterial heat) is more straightforward and do not require other advanced implementation technique. Finally, single float precision is preferred in order to save GPU memory.

Results

In this section, all simulations compute the result of a 10 minute freeze cycle. The volume of interest outlined by our grid remains constant $V = 10^{-3}\ m^3$. The error between the isosurface obtained using segmentation and simulation is quantified using a Hausdorff distance metric (noted d_H). This error has to be below the clinical requirements set at 2 mm. Finally, the following results have been computed using an Intel Xeon W3550 processor and a GeForce GTX580 GPU with 512 cores.

Numerical Study

A numerical study is performed to assess the choice of optimal parameters in our simulation. First, a sensitivity analysis on the time step is done. Regarding the literature values, the reference time step is set at $dt_{ref} = 0.01\ s$ and the reference edge length used is $dx_{ref} = 1\ mm$. A wide range of time steps is studied: from our reference $dt_{ref} = 0.01\ s$ to much larger time steps $dt = 0.5\ s$ always using dx_{ref} as element size. The maximum Hausdorff distance stays constant whatever the time step is: $max(d_H) = 0.27\ mm$. Concerning the mean Hausdorff distance, values vary very slightly: from 0.11 mm to 0.13 mm. Only a simulation using a time step $dt = 0.5\ s$ fails due to unstable behavior. From these results, it appears that the time step does not significantly alter

Edge Length (mm)	Number of tetrahedra	Computation Time (s)		Hausdorff distance (mm)	
		CPU	GPU	mean	max
6.67	20,250	24.85	1.29	1.00	3.16
3.33	162,000	134.2	5.73	0.96	1.83
2.0	750,000	671.1	25.36	0.26	0.54
1.25	3,072,000	3,623	97.37	0.11	0.37
1.0	6,000,000	8,682	N/A	REF	REF

Table A.1: Computation times and distance errors using different grid sizes.

accuracy, but it strongly impacts the stability. Using our Explicit-BDF solver, the time step cannot be larger than 0.2 s. Consequently, a $dt = 0.1$ s time step is now chosen.

Second, the error sensitivity related to the tetrahedral edge length has been characterized. Previous work reported that meshes with 1.0 mm edges can be chosen as reference. Table A.1 sums up both computation times and errors measured depending on the grid discretization. Using CPU computation, increasing the number of elements in the model dramatically increases the computation time, whereas GPU computing allows to keep reduced computation times. Focusing on the finer grid for GPU (1.25 mm edges), the GPU method offers a computation more than 37 times faster than the same grid on CPU. When taking into account our accuracy requirements, Table A.1 shows that grids with edges longer than 2 mm should not be considered. However, the last row shows that a computation involving 6 millions of tetrahedra exceeds the global memory available on our GPU (N/A).

Experimental Validation

To validate our simulation, we decided to perform our own experiments rather than relying on constructor reference iso-surfaces, as they have been obtained in experimental conditions we do not know precisely. We performed a series of experiments using Ice-Rod probes immersed in water. High resolution pictures of the ice ball (and a millimeter scale) were taken at different times of the freezing process (see Fig. A.2). CT scans of the same ice balls were also obtained at the end of the freezing cycle in order to have a three-dimensional model. The ice balls were then manually segmented.

After studying the freezing cycle of one cryoprobe to estimate the parameter of the needle, a high resolution X-ray of the needle was performed to precisely determine the dimensions of the cooling part, and set the correct boundary conditions for the model. Further to our simulation, the mean

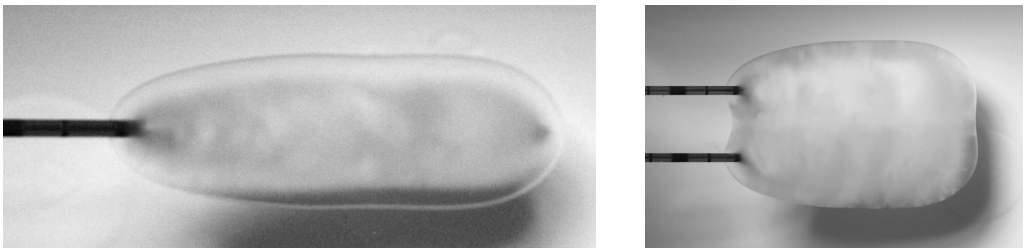

(a) Ice ball generated by one cryoprobe

(b) Synergistic effect of two cryoprobes

Figure A.2: Pictures of the ice ball using Ice-Rod needles

Hausdorff distance is 0.441 mm and its maximal value amounts to 1.108 mm. As detailed in Table A.1, this one needle simulation requires only 97.37 s which is less than 1 minute and 40 seconds. A simulation using two needles was then computed using the same parameters in order to evaluate the ability of our simulation to mimic the crucial synergistic effect presented in Buy et Gangi (2011). Computation time was 99.58 s, and the Hausdorff distance from the segmented ground-truth was computed. In this configuration, the mean Hausdorff distance was 0.271 mm, whereas the maximum value was 1.352 mm. The Hausdorff distances measured between the segmented and the simulated iso-surface (see distance maps in Fig. A.3(a) and A.3(b)) are very satisfactory since they remain below our 2 mm error requirement while requiring less than 2 minutes of computation.

These experimental measures allow us to validate our model as being able not only to simulate one single probe but also to faithfully reproduce the synergistic effect of multi-probes as described in Buy et Gangi (2011).

Clinical Application

After validating our model on *in vitro* data, we performed (retrospectively) a preliminary test on patient-data. Using our framework enables us to skip the segmentation, registration and even meshing steps that are time consuming, and potentially could all be source of error. Moreover, heterogeneity between healthy and tumor tissues is not distinctly noticeable from medical images. The simulation of cryotherapy from medical images is therefore straightforward. This patient has been treated using Ice-Sphere needles. After 97 seconds of computation, the resulting ice ball (see Fig. A.4(a)) was compared with the segmented post-operative iso-surface. The mean Hausdorff distance was computed at 0.655 mm with a maximum Hausdorff distance of 2.347 mm. The

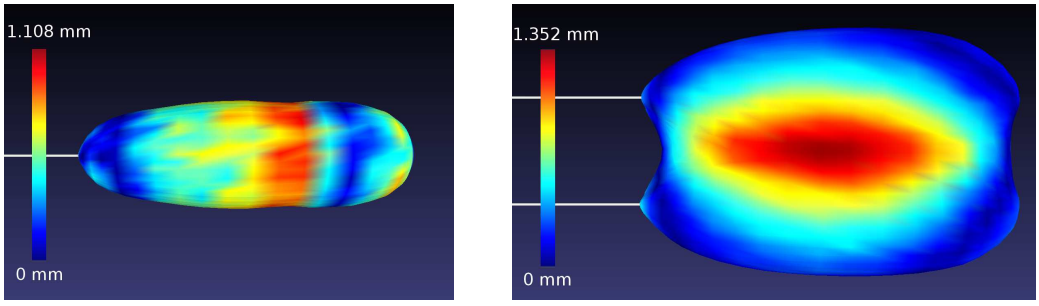

(a) Using one Ice-Rod cryoprobe (b) Using two Ice-Rod cryoprobes

Figure A.3: Hausdorff distance computed between the segmented and simulation based iso-surfaces

distance map is shown in Fig. A.4(b). This result is very encouraging, and certainly a lot more accurate than what could be obtained using the manufacturer iso-surfaces as an estimation of the resulting ice ball, as illustrated in Fig. A.4(c).

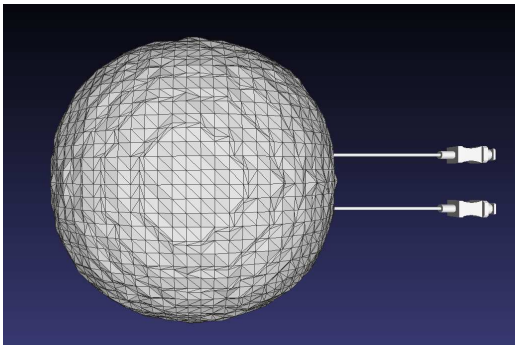

(a) Iso-surface from simulation

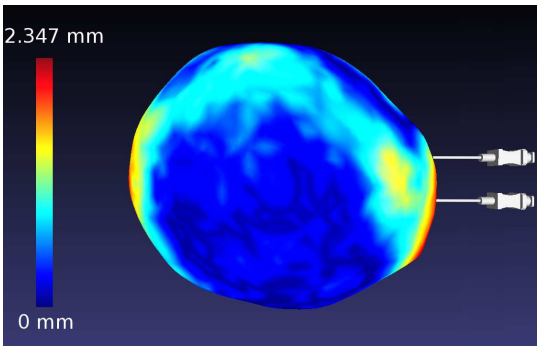

(b) Iso-surface from patient-specific data (with Hausdorff distance)

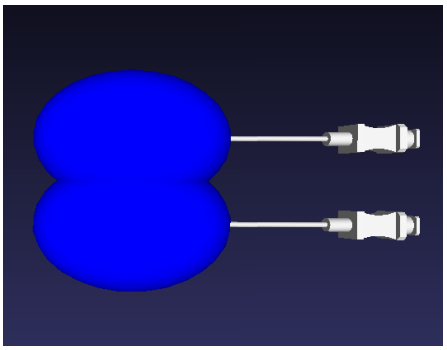

(c) Iso-surface from the constructor

Figure A.4: Comparison of the iso-surfaces resulting from a cryotherapy

Discussions and Conclusion

To conclude, we presented a very efficient simulation of cryotherapy, compatible with the requirements set by interventional radiologists : fast yet accurate, simple to use, and with limited processing of the pre-operative data. More validation on patient data is certainly needed, but more importantly, a better understanding of the tissue responses to the freezing process is needed. It is know for instance that fibrous tumors lead to small ice balls, or that blood vessels influence the shape of the ice ball. Yet, our current model allows to significantly decrease the safety margin by taking into account the synergistic effect of multi-cryoprobes with computation times consistent with clinical application, while preserving accuracy. In this context, our numerical strategies, such as the choice of GPU computing or grid-based finite element approach, prove to be relevant.

List of publications

Below is a partial list of my publications. Only the publications which were produced while I was working on my PhD between 2010 and 2014 are listed.

Book chapter

- [Faure et al. (2012)] F. Faure, C. Duriez, H. Delingette, J. Allard, B. Gilles, S. Marchesseau, H. Talbot, H. Courtecuisse, G. Bousquet, I. Peterlik et S. Cotin. SOFA: A Multi-Model Framework for Interactive Physical Simulation, vol. 11. Springer, 2012

Journal papers

- [Talbot et al. (2013a)] H. Talbot, S. Marchesseau, C. Duriez, M. Sermesant, S. Cotin et H. Delingette. Towards an Interactive Electromechanical Model of the Heart. Journal of the Royal Society Interface Focus, vol. 3, no. 2, 2013a

to be submitted:

- [Talbot et al. (2014c)] H. Talbot, F. Spadoni, C. Duriez, M. Sermesant, M. O'Neil, S. Cotin et H. Delingette. Interactive Training System for Interventional Electrocardiology Procedures. to be submitted, 2014c
- [Talbot et al. (2014a)] H. Talbot, C. Duriez, M. Sermesant, S. Cotin et H. Delingette. Personalization of Electrophysiology Model based on Data Assimilation. to be submitted, 2014a

Conference papers

- [Talbot et al. (2012a)] H. Talbot, S. Marchesseau, C. Duriez, H. Courtecuisse, J. Relan, M. Sermesant, S. Cotin et H. Delingette. Interactive Electromechanical Model of the Heart for Patient-Specific Therapy Planning and Training using SOFA. In VPH 2012, 2012a
- [Talbot et al. (2014b)] H. Talbot, M. Lekkal, R. Béssard-Duparc et S. Cotin. Interactive Planning of Cryotherapy Using Physically-Based Simulation.

In MMVR 21 - Medicine Meets Virtual Reality - 2014, Manhattan Beach, California, États-Unis, 2014b

European project deliverables

- [Talbot et al. (2011)] H. Talbot, F. Spadoni, M. Sermesant, N. Ayache et H. Delingette. Deliverable D10.4.1. Rapport de recherche, 2011
- [Talbot et al. (2013b)] H. Talbot, F. Spadoni, M. Sermesant, N. Ayache et H. Delingette. Deliverable D10.4.2. Rapport de recherche, 2013b

Workshop

- [Talbot et al. (2012b)] H. Talbot, S. Marchesseau, C. Duriez, H. Courtecuisse, J. Relan, M. Sermesant, S. Cotin et H. Delingette. Towards Real-Time Computation of Cardiac Electrophysiology for Training Simulator. In Statistical Atlases and Computational Models of the Heart - STACOM 2012 in the 15th International Conference on Medical Image Computing and Computer Assisted Intervention - MICCAI 2012, Lecture Notes in Computer Science, Springer, 2012b

Bibliography

[Aliev et Panfilov, 1996] R. Aliev et A. Panfilov. A Simple Two-Variable Model of Cardiac Excitation. Chaos, Solitons and Fractals, vol. 7, no. 3, pages 293–301, 1996.

[Aliot et al., 2009] E. M. Aliot, W. G. Stevenson, J. M. Almendral-Garrote, F. Bogun, C. H. Calkins, E. Delacretaz, P. Della Bella, G. Hindricks, P. Jaïs, M. E. Josephson et al.. Expert Consensus on Catheter Ablation of Ventricular Arrhythmias developed in a Partnership with the European Heart Rhythm Association (EHRA), a Registered Branch of the European Society of Cardiology (ESC), and the Heart Rhythm Society (HRS); in Collaboration with the American College of Cardiology (ACC) and the American Heart Association (AHA). Europace, vol. 11, no. 6, pages 771–817, 2009.

[Allard et al., 2011] J. Allard, H. Courtecuisse et F. Faure. Implicit FEM Solver on GPU for Interactive Deformation Simulation. In GPU Computing Gems Vol. 2, NVIDIA Elsevier, 2011.

[Bartocci et al., 2011] E. Bartocci, E. M. Cherry, J. Glimm, R. Grosu, S. A. Smolka et F. H. Fenton. Toward Real-Time Simulation of Cardiac Dynamics. In Proceedings of the 9th International Conference on CMSB, pages 103–112, ACM, 2011, ISBN 978-1-4503-0817-5.

[Bertails et al., 2006] F. Bertails, B. Audoly, M.-P. Cani, B. Querleux, F. Leroy et J.-L. Lévêque. Super-Helices for Predicting the Dynamics of Natural Hair. In ACM Transactions on Graphics, vol. 25, pages 1180–1187, 2006.

[Bestel et al., 2001] J. Bestel, F. Clément et M. Sorine. A Biomechanical Model of Muscle Contraction. In Medical Image Computing and Computer-Assisted Intervention - MICCAI 2001, vol. 2208 of Lecture Notes in Computer Science, edited by W. Niessen et M. Viergever, pages 1159–1161, Springer Berlin Heidelberg, 2001.

[Billet, 2010] F. Billet. Assimilation de Données Images pour la Personnalisation d'un Modèle Électromécanique du Coeur. Thèse de sciences (phd thesis), Université Nice Sophia-Antipolis, 2010.

[Bischof et al., 2002] C. H. Bischof, P. D. Hovland et B. Norris. Implementation of Automatic Differentiation Tools. In ACM SIGPLAN Notices, vol. 37, pages 98–107, ACM, 2002.

[Blezek et al., 2010] D. Blezek, D. Carlson, L. Cheng, J. Christensen, M. Callstrom et B. Erickson. Cell Accelerated Cryoablation Simulation. Computer Methods and Programs in Biomedicine, vol. 98, no. 3, pages 241–252, 2010.

[Brent, 2013] R. P. Brent. Algorithms for Minimization without Derivatives. Courier Dover Publications, 2013.

[Bueno-Orovio et al., 2008] A. Bueno-Orovio, E. M. Cherry et F. H. Fenton. Minimal Model for Human Ventricular Action Potentials in Tissue. Journal of Theoretical Biology, vol. 253, no. 3, pages 544–560, 2008.

[Buy et Gangi, 2011] X. Buy et A. Gangi. Thermoablation percutanée des cancers rénaux: radiofréquence ou cryoablation? Journal de Radiologie, vol. 92, no. 9, pages 774–788, 2011.

[Camara et al., 2010] O. Camara, A. Pashaei, R. Sebastian et A. Frangi. Personalization of Fast Conduction Purkinje System in Eikonal-Based Electrophysiological Models with Optical Mapping Data. In Statistical Atlases and Computational Models of the Heart, vol. 6364 of Lecture Notes in Computer Science, edited by O. Camara, M. Pop, K. Rhode, M. Sermesant, N. Smith et A. Young, pages 281–290, Springer Berlin Heidelberg, 2010, ISBN 978-3-642-15834-6.

[Chan, 2013] N.-Y. Chan. The Practice of Catheter Cryoablation for Cardiac Arrhythmias. John Wiley & Sons, 2013.

[Chapelle et al., 2012] D. Chapelle, P. Le Tallec, P. Moireau et M. Sorine. An Energy-Preserving Muscle Tissue model: Formulation and Compatible Discretizations. International Journal for Multiscale Computational Engineering, vol. 10, no. 2, pages 189–211, 2012.

[Chen et al., 2009] C. Chen, H. Kou, H. Liu, C. Chuang et L. Wang. Computer Assisted Simulation Model of Renal Tumor Cryosurgery. Heat Transfer 2009, vol. 3, pages 741–748, 2009.

[Cherry et al., 2003] E. M. Cherry, H. S. Greenside et C. S. Henriquez. Efficient Simulation of Three-Dimensional Anisotropic Cardiac Tissue using an Adaptive Mesh Refinement Method. Chaos: An Interdisciplinary Journal of Nonlinear Science, vol. 13, no. 3, pages 853–865, 2003.

[Chhay et al., 2012] M. Chhay, Y. Coudière et R. Turpault. How to Compute the Extracellular Potential in Electrocardiology from an Extended Monodomain Model. Research Report RR-7916, INRIA, 2012.

[Chiang et al., 2013] P. Chiang, J. Zheng, Y. Yu, K. Mak, C. Chui et Y. Cai. A VR Simulator for Intracardiac Intervention. Computer Graphics and Applications, IEEE, vol. 33, no. 1, pages 44–57, 2013, ISSN 0272-1716.

[Chinchapatnam et al., 2008] P. Chinchapatnam, K. S. Rhode, M. Ginks, C. A. Rinaldi, P. Lambiase, R. Razavi, S. Arridge et M. Sermesant. Model-Based Imaging of Cardiac Apparent Conductivity and Local Conduction Velocity for Diagnosis and Planning of Therapy. Medical Imaging, IEEE Transactions on, vol. 27, no. 11, pages 1631–1642, 2008.

[Clayton et Holden, 2004] R. H. Clayton et A. V. Holden. Propagation of Normal Beats and Re-entry in a Computational Model of Ventricular Cardiac Tissue with Regional Differences in Action Potential Shape and Duration. Progress in biophysics and molecular biology, vol. 85, no. 2, pages 473–499, 2004.

[Clements et al., 2004] J. C. Clements, J. Nenonen, P. Li et B. M. Horáček. Activation Dynamics in Anisotropic Cardiac Tissue via Decoupling. Annals of biomedical engineering, vol. 32, no. 7, pages 984–990, 2004.

[Corporation, 2013] S. M. S. Corporation. Simantha. 2013.

[Cosserat et al., 1909] E. Cosserat, F. Cosserat, M. Brocato et K. Chatzis. Théorie des Corps Déformables. A. Hermann Paris, 1909.

[Coudière et P., 2006] Y. Coudière et C. P.. Stability and Convergence of a Finite Volume Method for Two Systems of Reaction-Diffusion Equations in Electro-Cardiology. Nonlinear Analysis: Real World Applications, vol. 7, no. 4, pages 916–935, 2006.

[Dawson et al., 2000] S. Dawson, S. Cotin, D. Meglan, D. Shaffer et M. Ferrell. Designing a Computer-Based Simulator for Interventional Cardiology Training. Catheterization and Cardiovascular Interventions, vol. 51, no. 4, pages 522–527, 2000.

[Delingette et al., 2012] H. Delingette, F. Billet, K. C. Wong, M. Sermesant, S. Rhode, Kawal, M. Ginks, C. A. Rinaldi, R. Razavi et N. Ayache. Personalization of Cardiac Motion and Contractility from Images using Variational Data Assimilation. IEEE Transactions on Biomedical Engineering, vol. 59, no. 1, pages 20–24, 2012.

[Dequidt et al., 2008] J. Dequidt, M. Marchal, C. Duriez, E. Kerien et S. Cotin. Interactive Simulation of Embolization Coils: Modeling and Experimental Validation. In MICCAI 2008, vol. 5241, pages 695–702, Springer, 2008.

[Dössel et al., 2012] O. Dössel, M. W. Krueger, F. M. Weber, M. Wilhelms et G. Seemann. Computational Modeling of the Human Atrial Anatomy and Electrophysiology. Medical & biological engineering & computing, vol. 50, no. 8, pages 773–799, 2012.

[Dubuc et al., 2001] M. Dubuc, P. Khairy, A. RODRIGUEZ-SANTIAGO, M. Talajic, J.-C. TARDIF, B. Thibault et D. Roy. Catheter Cryoablation of the Atrioventricular Node in Patients with Atrial Fibrillation: a Novel Technology for Ablation of Cardiac Arrhythmias. Journal of cardiovascular electrophysiology, vol. 12, no. 4, pages 439–444, 2001.

[Duriez et al., 2005] C. Duriez, F. Dubois, A. Kheddar et C. Andriot. Realistic Haptic Rendering of Interactive Deformable Objects in Virtual Environments. IEEE Transactions on Visualization and Computer Graphics, vol. 12, pages 36–47, 2005.

[Duriez et al., 2006] C. Duriez, S. Cotin, J. Lenoir et P. Neumann. New Approaches to Catheter Navigation for Interventional Radiology Simulation 1. Computer Aided Surgery, vol. 11, no. 6, pages 300–308, 2006.

[Ethier et Bourgault, 2008] M. Ethier et Y. Bourgault. Semi-Implicit Time-Discretization Schemes for the Bidomain Model. SIAM J. Numerical Analysis, vol. 46, pages 2443–2468, 2008.

[Farina et Dössel, 2009] D. Farina et O. Dössel. Non-Invasive Model-Based Localization of Ventricular Ectopic Centers from Multichannel ECG. International Journal of Applied Electromagnetics and Mechanics, vol. 30, no. 3, pages 289–297, 2009.

[Faure et al., 2012] F. Faure, C. Duriez, H. Delingette, J. Allard, B. Gilles, S. Marchesseau, H. Talbot, H. Courtecuisse, G. Bousquet, I. Peterlik et S. Cotin. SOFA: A Multi-Model Framework for Interactive Physical Simulation, vol. 11. Springer, 2012.

[Fenton et Karma, 1998] F. Fenton et A. Karma. Vortex Dynamics in Three-Dimensional Continuous Myocardium with Fiber Rotation. Chaos, vol. 8, no. 1, pages 20–47, 1998.

[Fenton et Cherry, 2008] F. H. Fenton et E. M. Cherry. Models of cardiac cell. Scholarpedia, vol. 3, no. 8, page 1868, 2008.

[FitzHugh, 1961] R. FitzHugh. Impulses and Physiological States in Theoretical Models of Nerve Membrane. Biophysical Journal, vol. 1, no. 6, pages 445–466, 1961.

[Fletcher et Reeves, 1964] R. Fletcher et C. M. Reeves. Function Minimization by Conjugate Gradients. The computer journal, vol. 7, no. 2, pages 149–154, 1964.

[Fraser, 1957] A. S. Fraser. Simulation of Genetic Systems by Automatic Digital Computers I. Australian Journal of Biological Sciences, vol. 10, pages 484–491, 1957.

[Garny et al., 2008] A. Garny, D. P. Nickerson, J. Cooper, R. W. d. Santos, A. K. Miller, S. McKeever, P. M. F. Nielsen et P. J. Hunter. CellML and Associated Tools and Techniques. Philosophical Transactions: Mathematical, Physical and Engineering Sciences, vol. 366, no. 1878, pages pp. 3017–3043, 2008.

[Geman et Geman, 1984] S. Geman et D. Geman. Stochastic Rrelaxation, Gibbs Distributions, and the Bayesian Restoration of Images. Pattern Analysis and Machine Intelligence, IEEE Transactions on, , no. 6, pages 721–741, 1984.

[Georgiades et al., 2012] C. Georgiades, R. Rodriguez, E. Azene, C. Weiss, A. Chaux et *et al.*. Determination of the Nonlethal Margin Inside the Visible Ice-Ball During Percutaneous Cryoablation of Renal Tissue. Cardiovasc Intervent Radio, pages 1–8, 2012.

[Griewank et Walther, 2008] A. Griewank et A. Walther. Evaluating Derivatives: Principles and Techniques of Algorithmic Differentiation. Siam, 2008.

[Guillem et al., 2013] M. S. Guillem, A. M. Climent, J. Millet, Á. Arenal, F. Fernández-Avilés, J. Jalife, F. Atienza et O. Berenfeld. Non-Invasive Localization of Maximal Frequency Sites of Atrial Fibrillation by Body Surface Potential Mapping. Circulation: Arrhythmia and Electrophysiology, vol. 6, no. 2, pages 294–301, 2013.

[Handschin et Mayne, 1969] J. Handschin et D. Q. Mayne. Monte Carlo Techniques to Estimate the Conditional Expectation in Multi-Stage Non-Linear Filtering. International journal of control, vol. 9, no. 5, pages 547–559, 1969.

[Hastings, 1970] W. K. Hastings. Monte Carlo Sampling Methods using Markov Chains and their Applications. Biometrika, vol. 57, no. 1, pages 97–109, 1970.

[HealthCare, 2013] C. HealthCare. CathLabVR. 2013.

[Heidenreich et al., 2010] E. A. Heidenreich, J. M. Ferrero, M. Doblaré et J. F. Rodríguez. Adaptive Macro Finite Elements for the Numerical Solution of

Monodomain Equations in Cardiac Electrophysiology. Annals of biomedical engineering, vol. 38, no. 7, pages 2331–2345, 2010.

[Henriquez, 1992] C. Henriquez. Simulating the Electrical Behavior of Cardiac Tissue using the Bidomain Model. Critical reviews in biomedical engineering, vol. 21, no. 1, pages 1–77, 1992.

[Hestenes et Stiefel, 1952] M. R. Hestenes et E. Stiefel. Methods of Conjugate Gradients for Solving Linear Systems, vol. 49. NBS, 1952.

[Huxley, 1957] A. Huxley. Muscle Structure and Theories of Contraction. Prog Biophys Biophys Chem, vol. 7, pages 255–318, 1957.

[Johnson et Willemsen, 2004] D. Johnson et P. Willemsen. Accelerated Haptic Rendering of Polygonal Models through Local Descent. In Haptic Interfaces for Virtual Environment and Teleoperator Systems, 2004. HAPTICS '04. Proceedings. 12th International Symposium on, pages 18–23, 2004.

[Julier et al., 1995] S. J. Julier, J. K. Uhlmann et H. F. Durrant-Whyte. A New Approach for Filtering Nonlinear Systems. In American Control Conference, Proceedings of the 1995, vol. 3, pages 1628–1632, IEEE, 1995.

[Kalman, 1960] R. E. Kalman. A New Approach to Linear Filtering and Prediction Problems. Journal of Basic Engineering, vol. 82, no. 1, pages 35–45, 1960.

[Keener, 1991] J. Keener. An Eikonal-Curvature Equation for Action Potential Propagation in Myocardium. Journal of Mathematical Biology, vol. 29, pages 629–651, 1991.

[Konukoglu et al., 2011] E. Konukoglu, J. Relan, U. Cilingir, B. H. Menze, P. Chinchapatnam, A. Jadidi, H. Cochet, M. Hocini, H. Delingette, P. Jaïs et al.. Efficient Probabilistic Model Personalization Integrating Uncertainty on Data and Parameters: Application to Eikonal-Diffusion Models in Cardiac Electrophysiology. Progress in Biophysics and Molecular Biology, vol. 107, no. 1, pages 134–146, 2011.

[Lamecker et al., 2009] H. Lamecker, T. Mansi, J. Relan, F. Billet, M. Sermesant, N. Ayache et H. Delingette. Adaptive Tetrahedral Meshing for Personalized Cardiac Simulations. In CI2BM09 - MICCAI Workshop on Cardiovascular Interventional Imaging and Biophysical Mod pages 149–158, 2009.

[Lee et al., 2003] D. S. Lee, L. D. Green, P. P. Liu, P. Dorian, D. M. Newman, F. C. Grant, J. V. Tu et D. A. Alter. Effectiveness of Implantable Defibrillators for Preventing Arrhythmic Events and Death: a Meta-Analysis. Journal of the American College of Cardiology, vol. 41, no. 9, pages 1573–1582, 2003.

[Lines et al., 2003] G. T. Lines, P. Grottum et A. Tveito. Modeling the Electrical Activity of the Heart: a Bidomain Model of the Ventricles Embedded in a Torso. Computing and Visualization in Science, vol. 5, no. 4, pages 195–213, 2003.

[Liu et al., 2011] F. Liu, J. Walmsley et K. Burrage. Parameter Estimation for a Phenomenological Model of the Cardiac Action Potential. ANZIAM Journal, vol. 52, pages C482–C499, 2011.

[Luo et Rudy, 1991] C.-h. Luo et Y. Rudy. A Model of the Ventricular Cardiac Action Potential. Depolarization, Repolarization, and their Interaction. Circulation research, vol. 68, no. 6, pages 1501–1526, 1991.

[Magalov et al., 2008] Z. Magalov, A. Shitzer et D. Degani. Experimental and Numerical Study of One, Two, and Three Embedded Needle Cryoprobes Simultaneously Operated by High Pressure Argon Gas. Journal of heat transfer, vol. 130, no. 3, 2008.

[Mansi et al., 2011a] T. Mansi, X. Pennec, M. Sermesant, H. Delingette et N. Ayache. iLogDemons: A Demons-Based Registration Algorithm for Tracking Incompressible Elastic Biological Tissues. International Journal of Computer Vision, vol. 92, pages 92–111, 2011a.

[Mansi et al., 2011b] T. Mansi, X. Pennec, M. Sermesant, H. Delingette et N. Ayache. iLogDemons: A Demons-Based Registration Algorithm for Tracking Incompressible Elastic Biological Tissues. International Journal of Computer Vision, vol. 92, no. 1, pages 92–111, 2011b.

[Marchesseau et al., 2010] S. Marchesseau, T. Heimann, S. Chatelin, R. Willinger et H. Delingette. Multiplicative Jacobian Energy Decomposition Method for Fast Porous Visco-Hyperelastic Soft Tissue Model. Lecture Notes in Computer Science, vol. 6361, no. 1, pages 235–242, 2010.

[Marchesseau et al., 2012a] S. Marchesseau, H. Delingette, M. Sermesant et N. Ayache. Fast Parameter Calibration of a Cardiac Electromechanical Model from Medical Images Based on the Unscented Transform. Biomechanics and Modeling in Mechanobiology, pages 1–17, 2012a.

[Marchesseau et al., 2012b] S. Marchesseau, H. Delingette, M. Sermesant, M. Sorine, K. Rhode, S. Duckett, C. Rinaldi, R. Razavi et N. Ayache. Preliminary Specificity Study of the Bestel-Clément-Sorine electromechanical Model of the Heart using Parameter Calibration from Medical Images. Journal of the Mechanical Behavior of Biomedical Materials, 2012b.

[Maron et al., 2006] B. J. Maron, J. A. Towbin, G. Thiene, C. Antzelevitch, D. Corrado, D. Arnett, A. J. Moss, C. E. Seidman et J. B. Young. Contemporary Definitions and Classification of the Cardiomyopathies. Circulation, vol. 113, no. 14, pages 1807–1816, 2006.

[Mentice, 2012] Mentice. VIST. 2012.

[Metropolis et Ulam, 1949] N. Metropolis et S. Ulam. The Monte Carlo Method. Journal of the American statistical association, vol. 44, no. 247, pages 335–341, 1949.

[Mitchell et Schaeffer, 2003] C. Mitchell et D. Schaeffer. A Two-Current Model for the Dynamics of Cardiac Membrane. Bulletin of Mathematical Biology, vol. 65, pages 767–793, 2003.

[Moireau et Chapelle, 2011] P. Moireau et D. Chapelle. Reduced-order Unscented Kalman Filtering with Application to Parameter Identification in Large-Dimensional Systems. ESAIM: Control, Optimisation and Calculus of Variations, vol. 17, no. 02, pages 380–405, 2011.

[Nelder et Mead, 1965] J. A. Nelder et R. Mead. The Downhill Simplex Method. Computer Journal, vol. 7, no. 308-310, page 5, 1965.

[NICE, 2007] NICE. Arrhythmia - Implantable Cardioverter Defibrillators (ICDs) (review) (TA95). Clinical report, National Institute for Health and Care Excellence, 2007.

[Nichols et al., 2012] M. Nichols, N. Townsend, P. Scarborough, R. Luengo-Fernandez, J. Leal, A. Gray et M. Rayner. European Cardiovascular Disease Statistics 2012. European Heart Network, Brussels, European Society of Cardiology, Sophia Antipolis, page 104, 2012.

[Nichols et al., 2013] M. Nichols, N. Townsend, P. Scarborough et M. Rayner. Cardiovascular Disease in Europe: Epidemiological Update. European heart journal, vol. 34, no. 39, pages 3028–3034, 2013.

[Niederer et al., 2011] S. Niederer, L. Mitchell, N. Smith et G. Plank. Simulating Human Cardiac Electrophysiology on Clinical Time-Scales. Frontiers in Physiology, vol. 2, no. 14, 2011.

[Oliveira et al., 2012] R. S. Oliveira, B. M. Rocha, D. Burgarelli, W. Meira Jr et R. W. dos Santos. An adaptive Mesh Algorithm for the Numerical Solution of Electrical Models of the Heart. In Computational Science and Its Applications–ICCSA 2012, pages 649–664, Springer, 2012.

[Pathmanathan et al., 2010] P. Pathmanathan, M. O. Bernabeu, R. Bordas, J. Cooper, A. Garny, J. M. Pitt-Francis, J. P. Whiteley et D. J. Gavaghan. A Numerical Guide to the Solution of the Bidomain Equations of Cardiac Electrophysiology. Progress in Biophysics and Molecular Biology, vol. 102, no. 2, pages 136–155, 2010.

[Pathmanathan et al., 2011] P. Pathmanathan, G. Mirams, J. Southern et J. Whiteley. The Significant Effect of the Choice of Ionic Current Integration method in Cardiac Electro-Physiological Simulations. International Journal for Numerical Methods in Biomedical Engineering, 2011.

[Pennes, 1948] H. Pennes. Analysis of Tissue and Arterial Blood Temperatures in the Resting Human Forearm. Journal of applied physiology, vol. 1, no. 2, pages 93–122, 1948.

[Pierre, 2012] C. Pierre. Preconditioning the Bidomain Model with Almost Linear Complexity. Journal of Computational Physics, vol. 231, no. 1, pages 82–97, 2012.

[Polak et Ribiere, 1969] E. Polak et G. Ribiere. Note sur la Convergence de Méthodes de Directions Conjuguées. ESAIM: Mathematical Modelling and Numerical Analysis-Modélisation Mathématique et Analyse Numérique, vol. 3, no. R1, pages 35–43, 1969.

[Pop et al., 2009] M. Pop, M. Sermesant, D. Lepiller, M. Truong, E. McVeigh, E. Crystal, A. Dick, H. Delingette, N. Ayache et G. Wright. Fusion of Optical Imaging and MRI for the Evaluation and Adjustment of Macroscopic Models of Cardiac Electrophysiology: a Feasibility Study. Medical image analysis, vol. 13, no. 2, pages 370–380, 2009.

[Pop et al., 2012] M. Pop, M. Sermesant, G. Liu, J. Relan, T. Mansi, A. Soong, J.-M. Peyrat, M. Truong, P. Fefer, E. McVeigh et al.. Construction of 3D MR Image-Based Computer Models of Pathologic Hearts, Augmented with Histology and Optical Fluorescence Imaging to Characterize Action Potential Propagation. Medical Image Analysis, vol. 16, no. 2, pages 505–523, 2012.

[Potse et al., 2006] M. Potse, B. Dubé, J. Richer, A. Vinet et R. M. Gulrajani. A Comparison of Monodomain and Bidomain Reaction-Diffusion Models for Action Potential Propagation in the Human Heart. Biomedical Engineering, IEEE Transactions on, vol. 53, no. 12, pages 2425–2435, 2006.

[Powell, 1964] M. J. Powell. An Efficient Method for Finding the Minimum of a Function of Several Variables without Calculating Derivatives. The computer journal, vol. 7, no. 2, pages 155–162, 1964.

[Przemieniecki, 1985] J. S. Przemieniecki. Theory of Matrix Structural Analysis. Courier Dover Publications, 1985.

[Rapaka et al., 2012] S. Rapaka, T. Mansi, B. Georgescu, M. Pop, G. Wright, A. Kamen et D. Comaniciu. LBM-EP: Lattice-Boltzmann Method for Fast Cardiac Electrophysiology Simulation from 3D Images. In MICCAI 2012, vol. 7511, pages 33–40, Springer Berlin Heidelberg, 2012.

[Rawlings et Bakshi, 2006] J. B. Rawlings et B. R. Bakshi. Particle Filtering and Moving Horizon Estimation. Computers & chemical engineering, vol. 30, no. 10, pages 1529–1541, 2006.

[Relan et al., 2009a] J. Relan, M. Sermesant, H. Delingette, M. Pop, G. Wright et N. Ayache. Quantitative Comparison of Two Cardiac Electrophysiology Models using Personalisation to Optical and MR Data. In IEEE International Symposium on Biomedical Imaging: From Nano to Macro (ISBI'09), pages 1027–1030, Boston, MA, 2009a.

[Relan et al., 2009b] J. Relan, M. Sermesant, M. Pop, H. Delingette, M. Sorine, G. Wright et N. Ayache. Parameter Estimation of a 3D Cardiac Electrophysiology Model Including the Restitution Curve using Optical and MR Data. In World Congress on Medical Physics and Biomedical Engineering, vol. 25/IV of IFMBE Proceedings, edited by O. Dössel et W. C. Schlegel, pages 1716–1719, Springer, Munich, Germany, 2009b.

[Relan et al., 2009c] J. Relan, M. Sermesant, M. Pop, H. Delingette, M. Sorine, G. Wright, N. Ayache et al.. Volumetric prediction of cardiac electrophysiology using a heart model personalised to surface data. In CI2BM09-MICCAI Workshop on Cardiovascular Interventional Imaging and Biophysical Modelling, 2009c.

[Relan et al., 2010] J. Relan, P. Chinchapatnam, M. Sermesant, K. Rhode, H. Delingette, R. Razavi et N. Ayache. Coupled Personalisation of Electrophysiology Models for Ssimulation of Induced Ischemic Ventricular Tachycardia. In Medical Image Computing and Computer-Assisted Intervention-MICCAI 2010, pages 420–428, Springer, 2010.

[Relan et al., 2011a] J. Relan, P. Chinchapatnam, M. Sermesant, K. Rhode, M. Ginks, H. Delingette, C. A. Rinaldi, R. Razavi et N. Ayache. Coupled Personalization of Cardiac Electrophysiology Models for Prediction of Ischaemic Ventricular Tachycardia. Interface Focus, vol. 1, no. 3, pages 396–407, 2011a.

[Relan et al., 2011b] J. Relan, M. Pop, H. Delingette, G. Wright, N. Ayache et M. Sermesant. Personalisation of a Cardiac Electrophysiology Model using

Optical Mapping and MRI for Prediction of Changes with Pacing. IEEE Transactions on Bio-Medical Engineering, vol. 58, no. 12, pages 3339–3349, 2011b.

[Rosenbaum et Jalife, 2001] D. Rosenbaum et J. Jalife. Optical mapping of cardiac excitation and arrhythmias. Futura Armonk, NY, 2001.

[Roth, 1992] B. Roth. How the Anisotropy of the Intracellular and Extracellular Conductivities Influences Stimulation of Cardiac Muscle. Journal of mathematical biology, vol. 30, no. 6, pages 633–646, 1992.

[Rudy, 2010] Y. Rudy. Noninvasive Imaging of Cardiac Electrophysiology and Arrhythmia. Annals of the New York Academy of Sciences, vol. 1188, no. 1, pages 214–221, 2010.

[Sainte-Marie et al., 2006] J. Sainte-Marie, D. Chapelle, R. Cimrman et M. Sorine. Modeling and Estimation of the Cardiac Electromechanical Activity. Computers & Structures, vol. 84, pages 1743–1759, 2006.

[Sermesant et al., 2009] M. Sermesant, F. Billet, R. Chabiniok, T. Mansi, P. Chinchapatnam, P. Moireau, J.-M. Peyrat, K. Rhode, M. Ginks, P. Lambiase et al.. Personalised Electromechanical Model of the Heart for the Prediction of the Acute Effects of Cardiac Resynchronisation Therapy. In Functional Imaging and Modeling of the Heart, pages 239–248, Springer, 2009.

[Sermesant et al., 2012] M. Sermesant, R. Chabiniok, P. Chinchapatnam, T. Mansi, F. Billet, P. Moireau, J.-M. Peyrat, K. Wong, J. Relan, K. Rhode, M. Ginks, P. Lambiase, H. Delingette, M. Sorine, C. Rinaldi, D. Chapelle, R. Razavi et N. Ayache. Patient-Specific Electromechanical Models of the Heart for the Prediction of Pacing Acute Effects in CRT: A Preliminary Clinical Validation. Medical Image Analysis, vol. 16, no. 1, pages 201–215, 2012.

[Shanno, 1970] D. F. Shanno. Conditioning of Quasi-Newton Methods for Function Minimization. Mathematics of computation, vol. 24, no. 111, pages 647–656, 1970.

[Siemens, 2006] Siemens. Cathi. 2006.

[Simbionix, 2012] Simbionix. AngioMentor. 2012.

[Smith et al., 1962] G. L. Smith, S. F. Schmidt et L. A. McGee. Application of Statistical Filter Theory to the Optimal Estimation of Position and Velocity on Board a Circumlunar Vehicle. National Aeronautics and Space Administration, 1962.

[Steinhaus, 1989] B. M. Steinhaus. Estimating Cardiac Transmembrane Activation and Recovery Times from Unipolar and Bipolar Extracellular Electrograms: a Simulation Study. Circulation research, vol. 64, no. 3, pages 449–462, 1989.

[Talbot et al., 2011] H. Talbot, F. Spadoni, M. Sermesant, N. Ayache et H. Delingette. Deliverable D10.4.1. Rapport de recherche, 2011.

[Talbot et al., 2012a] H. Talbot, S. Marchesseau, C. Duriez, H. Courtecuisse, J. Relan, M. Sermesant, S. Cotin et H. Delingette. Interactive Electromechanical Model of the Heart for Patient-Specific Therapy Planning and Training using SOFA. In VPH 2012, 2012a.

[Talbot et al., 2012b] H. Talbot, S. Marchesseau, C. Duriez, H. Courtecuisse, J. Relan, M. Sermesant, S. Cotin et H. Delingette. Towards Real-Time Computation of Cardiac Electrophysiology for Training Simulator. In Statistical Atlases and Computational Models of the Heart - STACOM 2012 in the 15th International Conference on Medical Image Computing and Computer Assisted Intervention - MICCAI 2012, Lecture Notes in Computer Science, Springer, 2012b.

[Talbot et al., 2013a] H. Talbot, S. Marchesseau, C. Duriez, M. Sermesant, S. Cotin et H. Delingette. Towards an Interactive Electromechanical Model of the Heart. Journal of the Royal Society Interface Focus, vol. 3, no. 2, 2013a.

[Talbot et al., 2013b] H. Talbot, F. Spadoni, M. Sermesant, N. Ayache et H. Delingette. Deliverable D10.4.2. Rapport de recherche, 2013b.

[Talbot et al., 2014a] H. Talbot, C. Duriez, M. Sermesant, S. Cotin et H. Delingette. Personalization of Electrophysiology Model based on Data Assimilation. to be submitted, 2014a.

[Talbot et al., 2014b] H. Talbot, M. Lekkal, R. Béssard-Duparc et S. Cotin. Interactive Planning of Cryotherapy Using Physically-Based Simulation. In MMVR 21 - Medicine Meets Virtual Reality - 2014, Manhattan Beach, California, États-Unis, 2014b.

[Talbot et al., 2014c] H. Talbot, F. Spadoni, C. Duriez, M. Sermesant, M. O'Neil, S. Cotin et H. Delingette. Interactive Training System for Interventional Electrocardiology Procedures. to be submitted, 2014c.

[ten Tusscher et al., 2004] K. ten Tusscher, D. Noble, P. Noble et A. Panfilov. A Model for Human ventricular Tissue. American Journal of Physiology - Heart and Circulatory Physiology, vol. 286, no. 4, pages 1573–1589, 2004.

[Theetten et al., 2008] A. Theetten, L. Grisoni, C. Andriot et B. Barsky. Geometrically Exact Dynamic Splines. Computer-Aided Design, vol. 40, no. 1, pages 35–48, 2008.

[Tobon-Gomez et al., 2013] C. Tobon-Gomez, N. Duchateau, R. Sebastian, S. Marchesseau, O. Camara, E. Donal, M. De Craene, A. Pashaei, J. Relan, M. Steghofer et al.. Understanding the Mechanisms Amenable to CRT Response: from Pre-Operative Multimodal Image Data to Patient-Specific Computational Models. Medical & biological engineering & computing, vol. 51, no. 11, pages 1235–1250, 2013.

[Uhlmann, 1995] J. K. Uhlmann. Dynamic Map Building and Localization: New Theoretical Foundations. Ph.D. thesis, University of Oxford, 1995.

[Veneziani et Vergara, 2013] A. Veneziani et C. Vergara. Inverse problems in Cardiovascular Mathematics: toward patient-specific data assimilation and optimization. International journal for numerical methods in biomedical engineering, vol. 29, no. 7, pages 723–725, 2013.

[Wang et al., 2007a] F. Wang, L. Duratti, E. Samur, U. Spaelter et H. Bleuler. A Computer-Based Real-time Simulation of Interventional Radiology. In Engineering in Medicine and Biology Society, 2007. EMBS 2007. 29th Annual International Conference of the IEEE, pages 1742–1745, IEEE, 2007a.

[Wang, 2009] L. Wang. Personalized Noninvasive Imaging of Volumetric Cardiac Electrophysiology. Rochester Institute of Technology, 2009.

[Wang et al., 2010] L. Wang, H. Zhang, K. C. Wong, H. Liu et P. Shi. Physiological-Model-Constrained Noninvasive Reconstruction of Volumetric Myocardial Transmembrane Potentials. Biomedical Engineering, IEEE Transactions on, vol. 57, no. 2, pages 296–315, 2010.

[Wang et al., 2007b] Y. Wang, R. B. Schuessler, R. J. Damiano, P. K. Woodard et Y. Rudy. Non-Invasive Electrocardiographic Imaging (ECGI) of Scar-Related Atypical Atrial Flutter. Heart rhythm: the official journal of the Heart Rhythm Society, vol. 4, no. 12, page 1565, 2007b.

[Weber et al., 2010] F. M. Weber, C. Schilling, G. Seemann, A. Luik, C. Schmitt, C. Lorenz et O. Dossel. Wave-Direction and Conduction-Velocity Analysis from Intracardiac Electrograms - A Single-Shot Technique. Biomedical Engineering, IEEE Transactions on, vol. 57, no. 10, pages 2394–2401, 2010.

[Wellens et al., 1985] H. J. Wellens, P. Brugada et W. G. Stevenson. Programmed Electrical Stimulation of the Heart in Patients with Life-Threatening

Ventricular Arrhythmias: What is the Significance of Induced Arrhythmias and What is the Correct Stimulaton Protocol? Circulation, vol. 72, no. 1, pages 1–7, 1985.

[Wulff, 1974] W. Wulff. The Energy Conservation Equation for Living Tissue. Biomedical Engineering, IEEE Transactions on, , no. 6, pages 494–495, 1974.

[Young et al., 2010] J. Young, S. Kolla, D. Pick, P. Sountoulides, O. Kaufmann, C. Ortiz-Vanderdys, V. Huynh, A. Kaplan, L. Andrade, K. Osann et al.. In Vitro, Ex Vivo and In Vivo Isotherms for Renal Cryotherapy. Journal of Urology, vol. 183, no. 2, pages 752–758, 2010.

[Young et al., 2011] J. Young, E. Khanifar, N. Narula, C. Ortiz-Vanderdys, S. Kolla, D. Pick, P. Sountoulides, O. Kaufmann, K. Osann, V. Huynh et al.. Optimal Freeze Cycle Length for Renal Cryotherapy. The Journal of Urology, vol. 186, no. 1, pages 283–288, 2011.

[Young, 2011] J. e. a. Young. Are multiple Cryoprobes Additive or Synergistic in Renal Cryotherapy? Urology, 2011.

[Zettinig et al., 2013] O. Zettinig, T. Mansi, B. Georgescu, E. Kayvanpour, F. Sedaghat-Hamedani, A. Amr, J. Haas, H. Steen, B. Meder, H. Katus et al.. Fast Data-Driven Calibration of a Cardiac Electrophysiology Model from Images and ECG. In Medical Image Computing and Computer-Assisted Intervention–MICCAI 2013, pages 1–8, Springer, 2013.

[Zhang et al., 2005] J. Zhang, G. Sandison, J. Murthy et L. Xu. Numerical Simulation for Heat Transfer in Prostate Cancer Cryosurgery. J Biomech Eng, vol. 127, no. 2, pages 279–294, 2005.